3-18-2014

SiC For Advanced Biological Applications

Joseph Register
University of South Florida, jjregist@gmail.com

SiC for Advanced Biological Applications

by

Joseph J. Register

A dissertation submitted in partial fulfillment
of the requirements for the degree of
Doctor of Philosophy
Department of Electrical Engineering
College of Engineering
University of South Florida

Major Professor: Stephen E Saddow, Ph.D.
Christopher Frewin, Ph.D.
Andreas Muller, Ph.D.
Andrew Raij, Ph.D.
Mark Jaroszeski, Ph.D.

Date of Approval:
March 18, 2014

Keywords: Silicon Carbide, Optrode, Photocapacitance, MEMS, Neural Probe

DEDICATION

I dedicate this dissertation to my family, especially to my parents Joe and Debra Register. Your selfless sacrifices for our family allowed me to pursue my dreams and become a scientist. Your love for life, art, and knowledge guides my steps. I also would like to dedicate this to my wife Alicia, for her encouragement and support while working towards my goal.

ACKNOWLEDGMENTS

I would like to thank my advisor Dr. Stephen Saddow for his guidance, patience, and advice while navigating the Ph.D. process. In addition, I would like to thank my fellow team members, specifically, Dr. Alexandra Oliveros, Dr. Christopher Locke, Maysam Nezafati, Dr. Chris Frewin, and Justin King for processing a processing and fabrication help. I would also like to thank the great people at the nanotechnology research and education center (NREC) on the USF campus, specifically, Richard Everly for helping with material characterization and processing and Rob Tufts for mask help. A deep thank you to Dr. Boulais and his team at the naval surface warfare center (NSWC) Dahlgren in VA for help with the SiC photocapactiance work.

TABLE OF CONTENTS

LIST OF TABLES

LIST OF FIGURES

ABSTRACT

Silicon carbide (SiC) has been used for centuries as an industrial abrasive and has been actively researched since the 1960's as a robust material for power electronic applications. Despite being the first semiconductor to emit blue light in 1907, it has only recently been discovered that the material has crucial properties ideal for long-term, implantable biomedical devices. This is due to the fact that the material offers superior biocompatibility and hemocompatibility while providing rigid mechanical and chemical stability. In addition, the material is a wide-bandgap semiconductor that can be used for optoelectronics, light delivery, and optical sensors, which is the focus of this dissertation research.

In this work, we build on past accomplishments of the USF-SiC Group to develop active SiC-based Brain Machine Interfaces (BMIs) and develop techniques for coating other biomaterials with amorphous SiC (*a*-SiC) to improve device longevity. The work is undertaken to move the state of the art in *in vivo* biomedical devices towards long term functionality. In this document we also explore the use of SiC in other bio photonics work, as demonstrated by the creation of the first reported photosensitive capacitor in semi-insulating 4H-SiC, thus providing the mechanism for a simple, biocompatible, UV sensor that may be used for biomedical applications.

Amorphous silicon carbide coatings are extremely useful in developing agile biomaterial strategies. We show that by improving current *a*-SiC technology we provide a way that SiC biomaterials can coexist with other materials as a biocompatible encapsulation strategy. We present the development of a plasma enhanced chemical vapor deposition (PECVD) *a*-SIC process and include material characterization analysis. The process has shown good adhesion to a wide variety of substrates and cell viability tests confirm that it is a highly biocompatible coating whereby it passed the strict ISO 10993 standard tests for biomaterials and biodevices.

In related work, we present a 64-channel microelectrode array (MEA) fabricated on a cubic 3C-SiC polytype substrate as a preliminary step in making more complex neurological devices. The electrode-electrolyte system electrical impedance is studied, and the device is tested against the model. The system is wire-bonded and packaged to provide a full neural test bed that will be used in future work to compare substrate materials during long-term testing.

Expanding on this new MEA technology, we then use 3C-SiC to develop an active, implantable, BMI interface. New processes were developed for the dry etching of SiC neural probes. The developed 7 mm long implantable devices were designed to offer four channels of single-unit electrical recording with concurrent optical stimulation, a combination of device properties that is indeed at the state-of-the-art in neural probes at this time.

Finally, work in SiC photocapacitance is presented as it relates to radio-frequency tuning circuits as well as bio photonics. A planar geometry UV tunable photocapacitor is fabricated to demonstrate the effect of below-bandgap optical tuning. The device can be used in a number of applications ranging from fluorescence sensing to the tuning of antennas for low-power communications.

While technology exists for a wide variety of *in vivo* interfaces and sensors, few active devices last in the implantable environment for more than a few months. If these devices are going to reach a long-term implant capability, use of better materials and processing strategies will need to be developed. Potential devices and strategies for harnessing the SiC materials family for this very important application are reviewed and presented in this dissertation to serve as a possible roadmap to the development of advanced SiC-based biomedical devices.

CHAPTER 1: INTRODUCTION TO SIC FOR ADVANCED BIOLOGICAL APPLICATIONS

1.1 Brain Machine Interface (BMI) Overview

The brain-machine-interface, or BMI, acts as a bi-directional manmade bridge from neural tissue to the outside world. This technology is based upon a neural interface that allows for a direct signal pathway to the neurological system, thus allowing for signals to be routed around damaged tissue in addition to intercepting signals for use outside of the body. One of the most important applications is in the area of robotic prosthetics, whereby functionality can be restored after the loss of a limb such as a hand, arm, foot, leg, etc. The BMI system also includes electronics, either on-board or outside of the body, and the associated software and algorithms to restore nervous system functionality. BMI devices range from simple skin-electrodes that pick up neural signals non-invasively, to those implanted directly into the brain or peripheral nervous system. The long term goal of these interfaces is to restore lost senses, motor control, and cognitive ability. Impressive BMI systems have been demonstrated for short periods of time, typically on the order of months. However, without new biomaterials, these interface systems will be frozen at their current state even as advances are made in BMI electronics and algorithms. Clearly, a breakthrough is needed if BMI is to become a mainstream clinical therapeutic option for patients suffering from neurological impairment/loss of limbs. This is the focus of our work in this dissertation. We focus on improvements in biomaterials that can push the technology into the next era of long-term implantable interface.

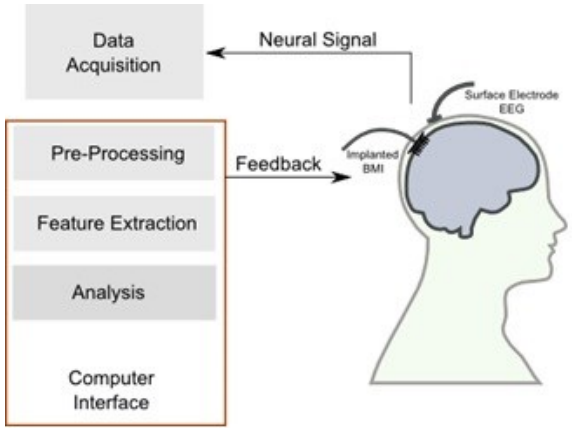

Figure 1: BMI overview demonstrating the components of a BMI system. Feedback may be required depending on the application thus motivating the need for a bi-directional BMI system.

In order to give a general overview of BMI systems one must first consider the fundamental biological basis for the signals that control the central nervous system (CNS) and peripheral nervous system (PNS), and how these signals can be analytically measured and modified though external stimuli. The brain consists of billions of specialized brain cells, called neurons, that contain voltage-gated ion channels within their membranes. These channels have a homeostatic state that results from a complex balance of various ions across the cell membrane. This semi-stable state is called a *resting potential* and is exhibited as a *membrane potential* of around -70mV in humans. The neuron will maintain this potential until it is perturbed by an adjacent neuron's depolarization or other outside force. Depolarization occurs when the membrane threshold value rises to approximately -55 mV in humans [1]. Within milliseconds a chain of events in the ion channels cause a sharp rise to a final value of +40 mV and then a slow reset over several milliseconds back into an attentive (resting) state. The frequency of the system can operate in a range of 1 Hz to over 5 KHz [2].

The small amplitude rise of a single neuron's action potential provides challenging recording conditions for BMI devices. At these small amplitudes the EM field radiated from the neuron is very weak and close to the electrical noise floor which is due to thermal oscillations and

external fields. To further complicate the problem the surrounding conductive fluid provides a current path further shunting the signal away from the recording electrode.

The Electroencephalography (EEG) system is the least invasive way of recording these signals. This is a transdermal system that takes advantage of the alignment of similar groups of spatially aligned neurons providing a collective action potential beat frequency that can be detected outside the body. Electrodes are placed on the subjects scalp for a high-impedance contact to the head. EEG is the oldest form of neural recording and is currently used clinically as a first line of defense for diagnosing stroke, brain tumors, and other serious neurological problems. The technique requires extensive processing and only provides very limited spatial resolution. Research in the area of digital processing for EEG derived signals has been an increasing field of research but ultimately the resolution of the technique is very limited and only allows for one-way signaling.

Taking EEG one step further, Electrocorticography (ECoG) places electrodes directly onto the exposed cortex during a surgical procedure (i.e., under the scalp). The technique provides a far superior spatial resolution to EEG as the signals are not dissipated across the skull thus allowing for a higher signal to noise ratio (SNR). ECoG is most commonly used as a surgical procedure for determining the epileptogenic zones that begin a seizure.

Table 1: Comparison of direct connection BMI techniques

	Pros	Cons	Reference
Electroencepha-lography (EEG)	• No trauma to the subject • Electrode systems are easy to fabricate due to large size • High Signal to noise ratio of collective action potentials • High channel counts are easily achievable	• Spatial accuracy is very poor • One-way communication	[3]
Electrocortico-graphy (ECoG)	• Good signal to noise ratio of collective action potentials • Spatial/temporal resolution better than EEG. • High channel counts are also easily achievable	• Implantation requires surgery • One-way communication	[3][4]
Single Unit Recording	• Extremely Spatially Accurate • Single neuron or groups of multiple neurons can be recorded. • Very high SNR	• Insertion Trauma damages neural tissue • Short Interface Duration • Recordings can't be used to extract any sensory information directly.	[3][4]

Recently, new advances in implantable microelectrodes have opened the door for the development of implantable interfaces. The interfaces allow the brain to link to an external system with high levels of temporal and spatial precision. Some experiments with BMI implants in monkeys have recently led to exciting new demonstrations. One experiment in particular by Nicolelis *et. al* demonstrated an implantable electrode system that facilitated a direct link between the motor cortex of a primate to a robotic arm [5]. The primate was taught to perform the certain task of stacking blocks using the arm and was given a juice reward in return.

These implantable devices, however, fall short in the area of useful device duration. Generally, any implant placed in the brain will fail after only a few short weeks or months due to gliosis and other immune system degradation [4]. Once the interface degrades the electrode is encapsulated and the electrical impedance of the system rises to a level unusable for recording. This would be unacceptable for human implantation due to the high risk of brain surgery procedures. Thus, new hardware is needed in this exciting field to bridge the gap to long-term solutions as current interface materials fall short of implantation goals.

1.2 Electrical Neural Interface

Although providing an exhaustive history of microelectrode arrays may be outside of the scope of this document, substantial progress has been made in the field. Many reviews have been published on the topic that include study of materials and methods on making microfabricated neural probes [6][7][8].

The first team to do work in the field was at Stanford in the mid-1960s. Kensall D. Wise and James B. Angell were some of the first to use microcircuit fabrication techniques to solve many of the problems that plagued traditional wire electrodes [9]. Shortly after this, in 1971, Wise and Angell reported to have created an onboard integrated circuit for the buffering of signals from one of their microelectrodes [10]. In 1984 the University of Japan created the first fully monolithic brain probe with amplifiers, multiplexing, and multiple recording sites along the probe's shank [11].

Much later, the University of Michigan became a forerunner in the field. It was here that the Center for Neural Communications Technology (CNCT) was founded in 1994 [12]. The center developed the first implantable boron-doped silicon probes for use in the brain. This was a large leap forward from the then currently used microwires and glass pipettes because it offered high channel density multichannel recording. By using implanted Boron as an etch stop nearly any 2D probe geometry could be made through chemical etching. The drawback was that the Boron-doped etch and release process developed was expensive and not ideal from a biocompatibility point of view [13].

Recently, the largest boon for the fabrication of implantable BMI devices has been the use of Reactive Ion Etching (RIE) and Dry Reactive Ion Etching (DRIE) techniques. By using various chemically reactive ion chemistries, such as Fluorine containing gasses, namely sulfur hexafluoride (SF_6), Silicon could be selectively etched at high aspect ratios with photopolymer masking. This new etching technique also allows our team to process SiC substrates for neural probes that cannot be wet chemically etched.

Today, microfabrication allows for a spatial resolution of 1 um or better and high channel densities. These new miniature electrodes make it possible to record the surrounding membrane potential and stimulate externally through either a voltage or current stimulus pulse on a neuron specific level addressable over large areas. Much of today's research is accomplished in-vitro through the use of planar microelectrode arrays (MEAs) as shown in Figure 2. In many applications these MEAs can replace the glass capillary electrodes that were once used in single cell recordings and provide the extra benefit of high channel densities. Through microfabrication, the 2-dimensional chips can easily have channel counts that allow for over a thousand recording sites. Generally, cells are cultured directly onto the devices and are recorded long-term for up to several weeks.

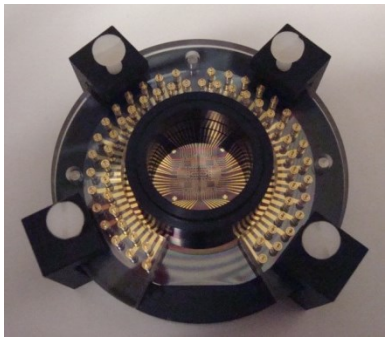

Figure 2: A photograph of a gold conductor on 3C-SiC MEA. Photo produced by Frewin *et. al* [14], [15]. The device was fabricated on a 2 inch diameter 3C-SiC on Si(100) epitaxial wafer grown at USF via hot-wall CVD.

For *in vivo,* studies electrodes are fabricated down a central mechanical support called a shank. The shank is use for targeted insertion of the electrodes into specific brain regions. These neural implants operate much like an MEA by sending and receiving signals to the onboard microelectrodes.

The devices are generally less than 1 mm thick and 300 um wide to reduce surgical insertion damage and contain several electrodes with metal traces that run down the length of the device. The main drawback of these implantable electrodes is that channel count is directly proportional to the size of the electrode. Larger, high channel-count devices inherently cause more damage during insertion. The devices are size limited and the conductor size can only be reduced to a point due to increasing electrical impedance. Some work has been done with 2D and 3D electrode arrays but generally at the cost of degraded recordings.

1.3 Optical Neural Interface

Before 2005, implantable brain interfaces only consisted of electrical interfaces. While this work continues, due to certain system advantages, optical stimulation systems have become commonplace with the advent of optogenetics techniques by Karl Deisseroth at Stanford University. This recent discovery allows us to change the way we think of BMI devices. With a subtle genetic manipulation, certain photo-sensitive ion channels can be added to a neuron's cell

membrane making it generate evoked action potentials (EAPs) or silencing its action based on light wavelength. That is to say we can turn the neuron into an optical switch.

The technology has already revolutionized how we model neurological disorders and will soon change how these diseases are treated [14][15][16]. Replacing metal electrodes in implantable BMI systems is also paramount to long-duration BMI performance, so the technique is a large step towards long-term chronically implanted systems.

Deisseroth and his team genetically isolated a photosensitive ion channel called Channelrhodopsin-2 (ChR2) that responds to blue light (centered at 473 nm in wavelength). Once illuminated, the ChR2 channel opens, allowing Na^+ cations to flow inward, increasing the depolarization of the membrane past threshold level, and instigating an action potential in the neuron (see Figure 3). Normally, the ChR2 opsin protein is found in a specific type of green algae; *Chlamydomonas reinhardtii*. Deisseroth's team gained international notoriety when they were able to recreate a ChR2 ion channel within a population of mammalian neurons by using a viral delivery vector [17]. ChR2 only requires one gene to be expressed in the host animal, works with visible light wavelengths, and provides precise millisecond temporal control of the neuron. In 2009 the technique gained even more momentum when ChR2 was used on living, non-human, primates to allow precise targeting and control of neurons (Xue Han *et al* 2009).

Just as blue light can activate ChR2, yellow light (centered at 580 nm in wavelength) can be used to activate another light driven Cl^- ion pump such as Halorhodopsin (NpHR). In contrast to ChR2, NpHR can effectively assist in repolarizing the neuronal membrane to essentially "turn off" the action potential. Total bipolar state control (i.e. on and off states) through neuronal action potentials can be realized using these two ion-channel structures in conjunction with blue and yellow light stimulation.

Cell-type-specific promoters for genetic modification can add ChR2 or NpHr ion channels

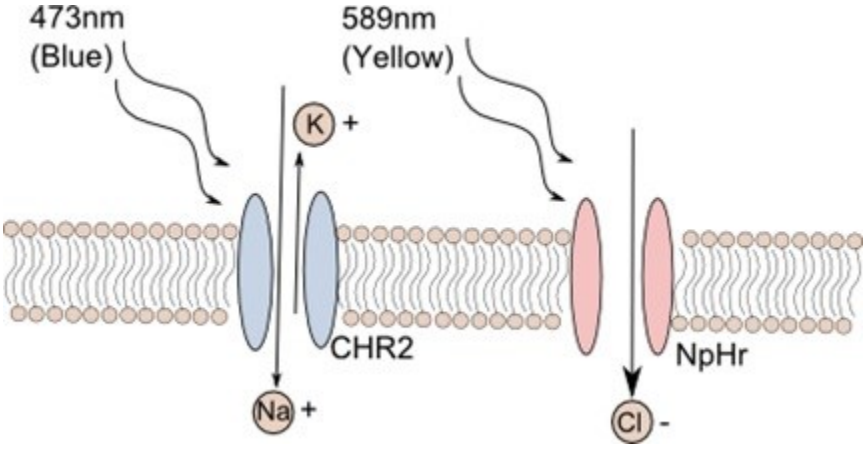

Figure 3: Ion channel overview for optogenetics. Blue light (473 nm) opens the ChR2 channel to allow membrane depolarization leading to AP stimulation. In contrast, yellow light (589 nm) can repolarize the membrane and thus 'turn off' the action potential. Thus full bi-state control can be realized. This field of research is known as Optogenetics.

to specific types of neurons. This differential targeting provides a great advantage over traditional electrical stimulation, which has very low levels of neuronal selectivity. Moreover, through this high level of selectivity, diseased brain circuitry can be traced allowing the development of new models for neuropsychiatric diseases. Other variants of these two ion pumps have been discovered with a wide range of sensitivity and selectivity options. These options can lead to the generation of complex techniques, which have been thus far unobtainable by any other methodology. Optogenetics may help unlock not only therapeutic relief of diseases like Parkinson's, but can help in the generation of cures for this and many other neurological disorders.

Optogenetics is now being used in laboratory animals to perform localized brain stimulation in mice with induced Parkinsonian tremor [18]. In these systems, glass-based optical fibers take the place of implanted electrodes for an entirely different mode of stimulation. Impulses of light travel down the optical fibers and then excite genetically modified neurons, which then respond to blue and yellow light. This important step has already changed the field of neuroscience by providing genetically targeted stimulation and control of neural tissue. If this treatment were tailored for Parkinson's patients, this would mean avoiding many of the common

side effects caused by stimulating the wrong brain region. It is not uncommon for deep brain stimulation (DBS) patents to have mood and sensory problems due to imprecise stimulation when their DBS pulse generator is active [19].

The current standard for localized optical stimulation in laboratory animals is a glass fiber implanted through the skull and held into place with cranial cement, see (Figure 4). The glass fiber protrudes out of the animal and is coupled into a high intensity light source. Light travels down the fiber and is delivered to a wide area inside the brain at the tip of the fiber.

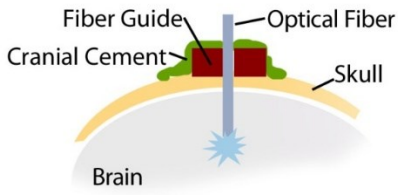

Figure 4: Standard glass fiber procedure for optogenetics in animals

This technique leaves much room for improvement. Glass fibers are not chemically bio stable and it has been shown that that the presence of glass can evoke an immune response in cortical tissue that can impede the light-to-neuron optical interface [20]. This glial scarring of brain tissue effectively lowers the spatial resolution and power output of the system. Second, the fragility of an implanted glass fiber is a problem that has yet to be fully addressed.

1.3.1 Clinical Uses for Optogenetics

The field of optogenetics BMI has some exciting years ahead. Never before have brain signals been explored with such granular detail and high temporal resolution. Already, research has shown that in animal models some visual sensory input can be restored, interconnections between brain regions that were lost due to a stroke can be improved, and motor function can be regained through the control of external prosthesis [21],[22],[5]. However, many hurdles still exist in long-term implantation of these strategies. Development of biomaterials that can survive the rigors of the *in-vivo* environment still provides one of the largest impediments to the technology.

Another short-term goal is the use of optogenetics to provide better deep brain stimulation protocols than those that already exist clinically. This has particular bearing on the research presented herein as current DBS technology is a rudimentary BMI interface that has vast room for improvement.

Parkinson's patents that do not respond to standard drug regimens have little choice for treatment. Often, these patents turn to direct neurostimulation wherein low-voltage electrical pulses are directly delivered to the subthalamic nucleus (STN) through metal electrodes implanted deep within the brain. This technique is approved by the FDA, but only as a humanitarian device exemption and is not approved for all cases [23]. The reason for this harsh control is the danger involved with DBS implantation and the long-term side effects of the prosthetic. Currently, the materials used in these implants give rise to the chronic immune system response from the body's own immune system. Eventually, this destructive cascade leads to neural degeneration around the implant (Figure 5)[24].

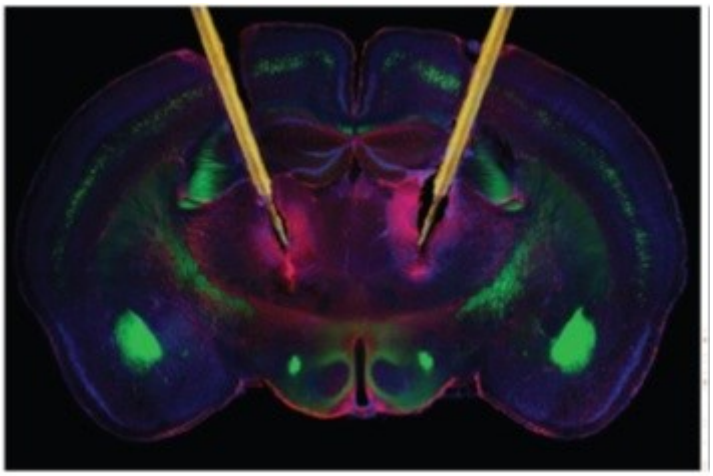

Figure 5: Deep brain stimulation electrodes implanted in the brain of a mouse. Implant shows extreme neural degeneration, marked by the presence of astrocytes stained against glial fibrillary acidic protein (GFAP) in red. Gliosis is especially noted around the active tips. Image from [25].

1.3.2 Optrodes for Optogenetics

An optrode is simply the combination of an optical fiber or monolithic waveguide combined with a conductive trace for closed-loop recording. Initially, optrodes for BMI were simple step index fibers implanted in mouse models. These devices worked well in short-term implantation, but were lacking multiple channels, spatially resolved emitters, and glass has been shown to be potentially toxic in chronic implantation [20]. Just as microfabricated electrodes revolutionized BMI, optogenetics technology could clearly benefit from microfabrication methods. Recent work has moved toward implantable microfabricated waveguides made from SU-8 and other biocompatible photo-patternable materials [26][27]. These are fabricated alongside metal electrodes for recording to create a bidirectional interface. Even with these designs, material challenges still exist but the great flexibility that microfabrication provides makes this technique superior in most respects.

1.3.3 Photocurrent Considerations

Whenever a metal electrode is illuminated with a high intensity light source a current is created. The so-called Becquerel effect generates a photocurrent that is amplified as if it were an evoked action potential (EAP). For devices with combined optical stimulation and electrical recording this can lead to recording artifacts [28]. The effect seems to be a larger problem with high powered lasers [29]. In the literature it has been found that driving longer 1 s low-power laser pulses in the range of 0.1 mW-3 mW minimizes this effect [28].

Generally, it is best to try and keep the electrodes out of the beam path of the optrode, this is a tradeoff however because the highest spike counts from ChR2 are recorded nearest the beam [29]. Another way to minimize the effect is through changing the material of the electrode altogether. Certain conductors such as Indium Tin Oxide (ITO) seem to completely eliminate the effect, but using ITO has drawbacks of protein absorption and a lack of longevity [30].

1.4 SiC for Biophotonics

Due to the wide bandgap property and mechanical resilience of SiC it lends itself well to biophotonic devices such as Optogenetic light delivery and other implantable *in vivo* sensors. The production of UV photodetectors in single crystal SiC is well documented in the literature [31]. In addition, it has been shown that visible high-index optical waveguides can be made from the material [32]. This makes the candidate a likely replacement for system components used in optogenetics and as a sensing element for in vivo florescence microscopy using system on a chip architecture. The literature shows promising data for SiC material as this material (in both amorphous and cubic forms) preventing bio-fouling that may obscure an optical sensor providing for un-needed insertion loss [33][34].

1.5 Materials Challenges

Any foreign object placed into the body will inevitably trigger an immune cascade that evokes an attack by the body's immune system. The brain in particular is a special case of this. The brain has specialty cells called astrocytes and glia that activate when an unwanted substance is detected.

Generally, this reaction is warranted when cancerous neurons go awry or toxic substances are introduced. These cells trigger a process that ends in macrophages enveloping the problem area and sealing it off from the rest of the brain. However, for a cortical implant, this cascade goes into overdrive thus damaging interconnects with the electrodes and optical emitters. Controlling this cascade is the primary factor when designing devices for the body (see Figure 6).

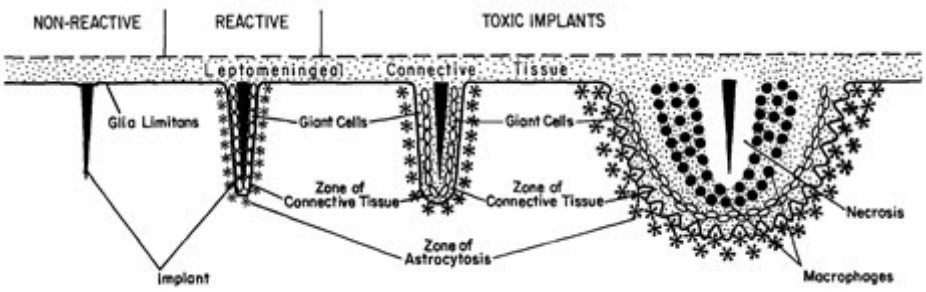

Figure 6: Various states of immune response for a cortical implant [35]. Some stages shown are the gradual activation of astrocytes, connective tissue, and giant cells formed by interconnected macrophages.

Materials for BMI have changed very little since their inception. The way these implants are created has rapidly become more complex but little ground has been gained in the area of long-term biocompatible materials for all the necessary components to the system. Although many of the currently used biomaterials have found some clinical success, these materials still fall far short of the requirements of long-term implantation goals. Commonly used insulators, such as polyimide, degrade and crack over time and metals leach ions into the body [8], [36].

In order for the immune response to begin, protein absorption must happen first so controlling this parameter is key to long-term performance [37]. Nearly all material surfaces, including metals, absorb proteins over time. While little is known about the mechanisms involved with protein absorption, a link has been made between the surface roughness, surface wettability, and surface charge and cell proliferation [38]. Also, many bio-active surface coatings have been developed to enhance a given material's biocompatibility through limiting surface absorption or improving cell attachment but the duration of the effect is limited [36]. A high variability exists in the biocompatibility data. This is not surprising considering the variability in biological testing. Even when concurrent tests are done with the same material on the same animal the data can differ [36]. Despite this, some things are well known about the material performance and we summarize herein some of the more important material players for BMI.

Generally, we are referring to materials used to manufacture passive implant devices, and we further separate the materials into categories as insulators and conductors. Waveguides will be discussed briefly as they relate to Optogenetics, but they are generally the same materials used for dielectric insulation.

It is important to note that significant evidence exists to support the belief that the fundamental driving factor behind the chronic inflammatory reaction is not simply the insertion trauma itself, but instead the chronic implantation and the materials within the implant. For example, a recent study performed by Ludwig K. *et al.* compared the glial response of mouse models that had nearly identical surgical procedures where Michigan style probes were inserted into the brains of adult male mice (species Fischer 344) [21] [39]. The control group had the probes immediately removed while other groups had the implants chronically inserted for 2 or 4 weeks before the animals were sacrificed for analysis. Using glial fibrillary acidic protein (GFAP) stain for astrocyte activity and ED1 analysis for the presence of macrophages, the brains of the mice were analyzed. Although both groups showed a response, the response from the control group was nearly non-existent indicating that the bulk of the immune response had occurred as a result of chronic implantation. This is strong evidence that the primary immune response comes from the chronic implantation and new materials must be developed to mitigate the local immune response.

1.5.1 Insulator Materials

Silica (SiO_2) was one of the first electrical insulators used for microfabricated implants and has been used even in recent work. It was a natural development as the first implantable probes were being made with pre-existing semiconductor tooling. The material is easily deposited by Plasma Enhanced Chemical Vapor Deposition (PECVD), created with thermal oxide growth, or even sputtering techniques. The material etches well with common Hydrofluoric Acid (HF) and can be patterned using standard lithography. Silicon Nitride (Si_3N_4), a similar coating, is deposited with the same techniques but is somewhat more difficult to pattern. While standardized

biocompatibility testing is not yet prevalent in the literature, material dissolution can give a picture of how much material is lost into the surrounding environment. Dissolution tests simply benchmark the loss of material over time using spectrophotometry, transmission electron microscopy, or liquid Fourier transform infrared spectroscopy (FTIR) measurements. A dissolution test performed by Maloney *et al.*, in 2005 showed that PECVD Si_3N_4 implanted in rats had a slightly slower dissolution rate of 2 nm/day as compared to that of 2.5 nm/day found in SiO_2 under the same conditions [40].

The amorphous form of Silicon Carbide (*a*-SiC), has recently been gaining notice among the electrophysiology community for its durability and chemical resistance. Deposited by PECVD, *a*-SiC has shown no detectable dissolution when held in a bath of phosphate-buffered saline (PBS) solution for 42 weeks at 37 °C [7]. The material's resistivity (9.0E15 Ω•cm) is slightly higher than that of SiO_2 (1.4E10 Ω•cm), providing better, more chemically resistant insulation when tested on SiO_2 coated Si wafers [7].

In addition to deposited rigid materials, polymers are often used for electrically insulating passivation layers as well as optical guides. Some common polymers used in cortical implants are polyimide, Teflon, or SU-8 photopolymer, with polyethylene and polypropylene used to a lesser degree. Most show good overall biocompatibility, but long term they tend to crack and fail negating their purpose as a long-term passivation layer.

1.5.2 Electrode Materials

A chronically implanted BMI electrode is susceptible to the same chronic inflammatory response as the rest of the implant. While stimulation mode systems such as deep brain stimulation (DBS) pulse generators overcome this by increasing signal amplitude this is not an option for recording. The EAP generated by the neuron will exist at fixed amplitude while the electrodes interface to the surrounding tissue continues to degrade. This is why electrode design for chronic implantation is so important. In order to improve the situation you must address both

the damage to the interface caused by the body's immune response, and by the faradic interactions at the interface.

To mitigate the immune response, metals with low protein absorption are used. Without absorbing the initial immunoglobulin G (igG) proteins the immune response would be greatly mitigated. This mitigation would not be complete, however, due to trauma caused to the insertion site. Metals such as gold (Au) and platinum (Pt) are particularly good at this and are heavily used in implantable devices as a consequence.

Faradic interactions are a consequence of ionic charge transfer between the metal and surrounding electrolyte. These reactions can be avoided altogether through eliminating charge-based stimulation and using optical techniques but this is a long way off from clinical implantation. These effects are reduced through using bi-phasic pulse stimulation waveforms so that no net charge remains after the stimulation cycle (one complete charge and discharge) is complete.

Metal ion dissolution is also of great importance in chronic electrode implantation. Toxic metals can leach into the surrounding tissue and cause cell death. Certain metals have less dissolution but all available metals dissolve eventually. Therefore new electrode materials are necessary.

1.5.3 SiC for BMI Devices

SiC can be formed in amorphous, crystalline and polycrystalline forms. The single crystal form has over 250 known polymorphs but the most commonly grown varieties are the cubic 3C- and hexagonal 4H- and 6H-SiC forms [13]. These forms are used by the semiconductor industry as a wide bandgap semiconductor. 6H-SiC is commonly used to make LED emitters and power electronic devices such as field-effect transistors [ref].

The mechanical properties of cubic SiC are particularly useful. For example, the Young's modulus of 3C-SiC is around 450 GPa, and a hardness of 2800 Kg/mm^2 give it very little deformation under mechanical load and durability in hostile environments [41]. This allows for thin devices that lower the risk of micro hemorrhage and damage to surrounding tissue.

Optically, SiC varies in bandgap from 2.36 eV (3C-SiC) to 3.05 eV (4H-SiC) and can be used as an optical waveguide for most of the visible spectra thus making the material a good candidate for optogenetics devices as well as fluorescence sensing [34].

Work performed by previous members of our group has suggested that cubic SiC shows good biocompatibility and hemocompatibility over and above other common substrate materials such as silicon [13]. The cubic form of the material possesses many physical properties that make it suitable for harsh chemical environments found in the body [34]. Work has been done by our group to determine even within these common SiC polymorphs which one provides the best biocompatibility or hemocompatibility and it was determined that this was somewhat application specific .

Unfortunately the mechanical resilience and chemical resistance of SiC come at a high cost. No effective wet-chemical etching exists for single crystal SiC and dry etching techniques are slow and expensive. This has been the primary reason for the biomaterial community not fully embracing single crystal SiC systems. As part of our work, we seek ways to make the process faster and more affordable thus paving the way for clinical use of this impressive material system.

1.6 Summary

The stimulation and recording of brain signals will provide a bright future for BMI in the medical field. As a highly robust, wide-bandgap semiconductor, SiC can be used as mechanical s, insulation, and active optical devices. The research suggests that SiC provides excellent biocompatibility and hemocompatibility and works well as an encapsulation strategy in fabricated devices. SiC may be an ideal candidate for many implanted, system-on-a-chip type devices, particularly those involving optics. While a steady stream of promising literature exists for the biocompatibility of SiC, little work has been done in the way of developing this material for use in biomedical devices. The fabrication processes are still extremely difficult and time consuming thus keeping the material from reaching commonplace use in the biomedical community. We therefore explore using this material for BMI and photocapacitance based sensors for the biomedical device

community. In this chapter we provided an overview of current implantable BMI strategies, materials, and techniques as well as proposing the use of SiC in biophotonics applications.

In Chapter 2 we investigate amorphous coatings for whole device encapsulation strategies. We develop a new PECVD process for the rapid deposition of *a*-SiC films over existing materials and then characterize the material for both its material properties and biocompatibility via in-vitro cell viability testing.

In Chapter 3 we lay the groundwork for electrical BMI interfaces through the development of a micro electrode array (MEA) device for stimulation and recording using 64 channels. A point-contact model was developed of the electrode-electrolyte interface and the fabricated device was then tested against the model. The lessons learned from this device were then carried through to the design of an implantable optogenetic stimulation device presented in Chapter 4.

In Chapter 4 we focus on implantable optrode development with the utilization of the *a*-SiC coatings and SiC substrates developed by our team. Building upon the passive implant work and MEA devices created by our team we develop new strategies for fabricating SiC based shank probes and ultimately integrate electrodes and waveguides onto one device. The processes developed allow for the biomedical device community to rapidly fabricate SiC based designs with active electrode arrays.

Chapter 5 introduces work done on the use of semi-insulating 4H-SiC for sensing visible UV light. In collaboration with The Naval Surface Warfare Center (NSWC), the sensor was fabricated at USF and characterized for its response to visible light at 473nm.

CHAPTER 2: AMORPHOUS SIC FOR BIODEVICES

2.1 Motivation for Amorphous Silicon Carbide (a-SiC) Films

Amorphous silicon carbide, denoted typically as *a*-SiC, has been proven to provide inert encapsulation for biodevices *in-vivo* and may prove to be pivotal in increasing the longevity of biodevice electronics. The material is inherently insulating, has high-K dielectric properties, high wear resistance, and works well as a durable coating. Unlike its single crystal cousin, the highly insulating property of *a*-SiC comes about from the amorphous microstructure and low deposition temperatures used. The lower deposition temperature prevents dopants present during the deposition from being electrically activated thereby providing an electrical insulator. The material can be used as an insulating outer encapsulation layer, thereby replacing or enhancing current polymer-based prosthetic coatings. The total encapsulation of electronic circuitry by *a*-SiC has been tested and has led to low water absorption and high wear resistance [7].

Amorphous SiC is a material that is now being used as an encapsulation strategy for *in-vivo* prosthetics. Most notably, the FDA has allowed *a*-SiC as a coating for commercially available cardiac stents. Heart stents, such as the one produced by the German firm Biotronik GmbH under the trade name Rithron-XR™, have ushered the coating into commercial clinical use. The material has been used as an optical coating in the past but we are reviving this use as a biocompatible coating that is easier to work with than single crystal variations of SiC.

2.2 Process Development

To develop this capability we began by benchmarking a PECVD *a*-SiC process that could be performed here at USF. The characterization runs were done at the Nanotechnology Research and Education Center (NREC) cleanroom on campus using a Plasmatherm 700 PECVD system. Two-inch (100) silicon wafer substrates were coated with films at 250 °C using methane (CH_4)

and silane (SiH_4) gas precursors with argon (Ar) as a bulk dilution gas. PECVD *a*-SiC film uniformity is particularly sensitive to the deposition pressure. The literature shows that a uniformity maximum exists near 900 mT [42]. Therefore, pressure was held constant at 900 mT for each run while the precursor gas ratio (CH_4/SiH_4) was varied from a ratio of 6.6 to 30. The films were then characterized for stress, chemical resistance, and optical index. In addition, transmission electron microscopy (TEM) (Figure 26) was performed to ensure the films were amorphous. Over twenty runs were performed with the goal of realizing an *a*-SiC film that would hold up to chemical resistance testing.

Early films exhibited large stress gradients causing telephone cord delamination showing the process was significantly detuned. Often, the films would appear sound and delaminate several days after the deposition. Profilometry based stress measurement was implemented as a method of benchmarking the stress imparted to the wafer due to the deposition.

2.2.1 Profilometry Stress Measurement

Using profilometry for stress measurement is a straightforward process wherein the wafer's curve is measured before and after the film deposition. Any change in the geometry of the surface is assumed to come from the film and the inherent stress of the film is then extrapolated from the new curvature value. The imposed stress can be calculated with Stony's formula (2.1) [43].

$$\sigma = \frac{1}{6}\left(\frac{1}{R_{post}} - \frac{1}{R_{pre}}\right)\frac{E}{(1-v)}\frac{{t_s}^2}{t_f} \tag{2.1}$$

where E is the Young's Modulus of the material, R_{post} is the radius of curvature post deposition, R_{pre} is the radius before the deposition of the film, t_s is the film thickness of the substrate, and t_f is the thickness of the film, and v is the Poisson's ratio of the substrate.

Using a Dektak 150 optical profilometer we performed curvature based stress optimization to the deposition process. The tool calculates stress using equation 2.1, pre scan curvature measured before the deposition, and post scan data measured along the same path. Standard 2"

(100) silicon wafers were RCA cleaned and marked with polyimide tape running across the length of the substrate. The polyimide tapeline was used for film thickness verification and as a geometric reference for the profilometer probe to measure in the same location each time. For the test, the silane (SiH_4) flow rate was held constant at 15 sccm while the methane concentration was increased on each run. The deposition temperature was held constant for all of the tests at 250 °C and the pressure at 900 mT during the deposition. Argon acted as the dilution gas and had a flow of 500 sscm. After each run, the stress was profiled and the results were compiled into Figure 7.

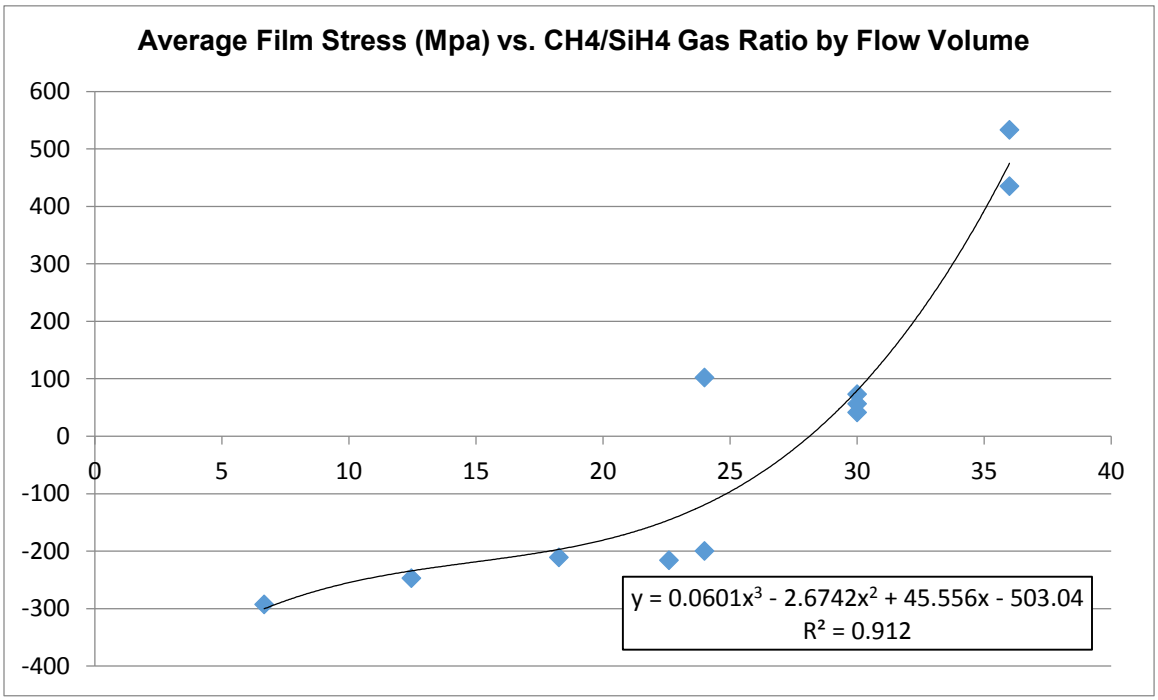

Figure 7: Average film stress (MPa) vs. CH_4/SiH_4 gas ratio. A polynomial fit was applied to the data as shown in the text box with an R^2 value of 0.9 indicating a strong fit.

The test resulted in very low stress for CH_4/SiH_4 ~ 30. Again, several PECVD runs were performed near this ratio while varying the SiH_4 flow to determine the lowest stress value. Eventually, we reached the accuracy of the tool for our measurement technique which is ≈10 MPa and settled on the process shown in Table 2. This ratio was then set for future films to be deposited at this null point used for further testing and characterization. It should be noted that although the

gas precursor ratio used varies somewhat from those values in the literature, the systems for PECVD vary greatly. Each process is thus unique due to the equipment constraints.

Table 2: Process conditions for low stress *a*-SiC films (PECVD).

Parameter	Value
Single RF Supply	13.57 MHz
Temperature	250 C
Pressure	900 mT
Silane (SiH_4) flow rate	12 sccm
Methane (CH_4) flow rate	360 sccm
Argon (Ar) flow rate	500 sccm

2.2.2 Atomic Force Microscopy (AFM)

Early *a*-SiC samples from selected for testing and imaged using atomic force microscopy (AFM) for surface analysis and pinhole testing. The surface was very smooth and indicative of *a*-SiC films found in the literature with a RMS roughness of 551.7 pm. However, pinhole defects were found in the initial films thus indicating process improvements were necessary.

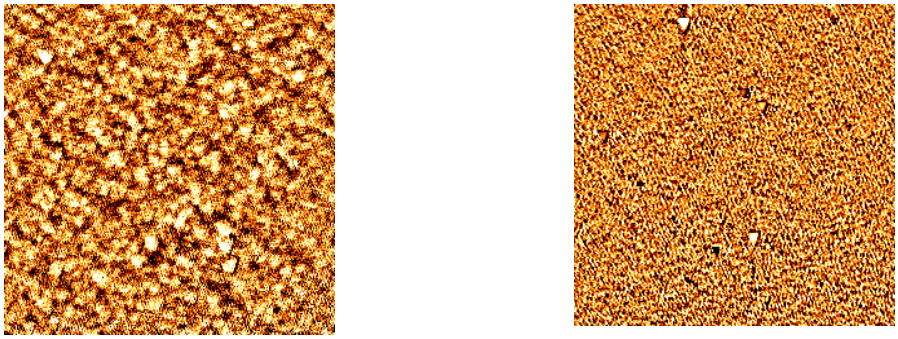

(A)
5x5 um

(B)
10x10 um

Figure 8: AFM image of sample ID PASIC052112 (a) a 5x5 um AFM scan of the surface RMS = 551.7 pm (b) 1 10x10 um scan of the same sample. Data taken in tapping mode using a Park XE-100 AFM by M. Nezafati, USF SiC Group.

To alleviate this effect it was found that by adding an Ar sputtering step before the PECVD deposition clean, pinhole free, thin films could be realized. The thickness of the film was maintained for both tests of 230 nm.

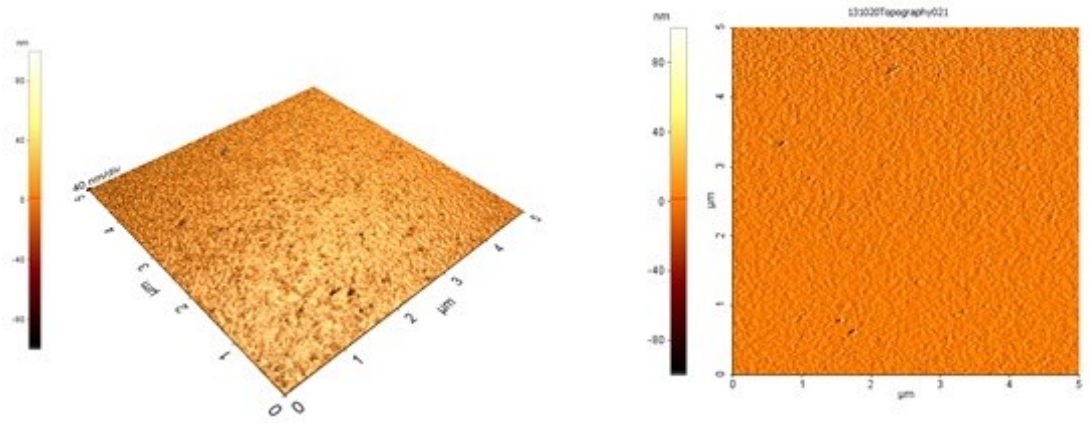

(A) (B)

Figure 9: AFM image of sample ID PASIC102013 (230 nm thick *a*-SiC). (A) a 5x5 um AFM scan of the surface showing 3D topology. (B) 5x5 um scan of the sample showing reduced roughness and a lack of pinhole defects. Sample RMS roughness of 1.2 nm. Data taken in tapping mode using a Park XE-100 AFM by M. Nezafati, USF SiC Group.

2.2.3 TEM/SAD/EDAX

Transmission electron microscopy analysis allows for cross sectional views of the sample on an atomic level. The measurements were taken on a Technai F20 TEM system. The system uses a Schottky Field emitter with an energy spread of 0.7 eV or less. In our test, the sample was thinned and fixed using a focused ion beam (FIB) at the USF NREC facility.

The TEM micrograph shows the expected amorphous structure of the PECVD deposited *a*-SiC film on top of the highly ordered Si substrate (Figure 10a). In addition, using selected area diffraction (SAD) within the TEM, it was shown that the film has very little short-range order (Figure 10b). This SAD pattern indicative of an amorphous film.

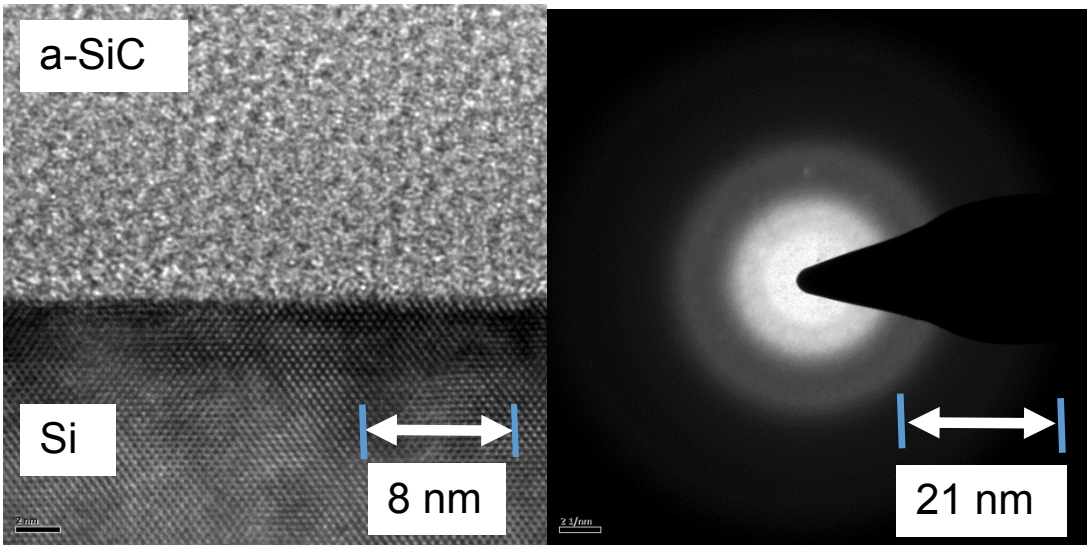

Figure 10: TEM micrograph and SAD data from sample PASIC052112. LEFT: Cross-section TEM micrograph of the PECVD deposited sample PASIC052112(A) appears to be a non-crystalline solid indicative of an amorphous SiC film. RIGHT: The SAD pattern showing an amorphous material. Data taken by Dr. Y. Emirof, USF NREC.

The Technai F20 is also capable of Energy-dispersive X-Ray Spectroscopy (EDAX) analysis. In this technique, the localized atomic composition is given based on the location of the electron beam. The atomic species in the localized area give off a characteristic x-ray emission.

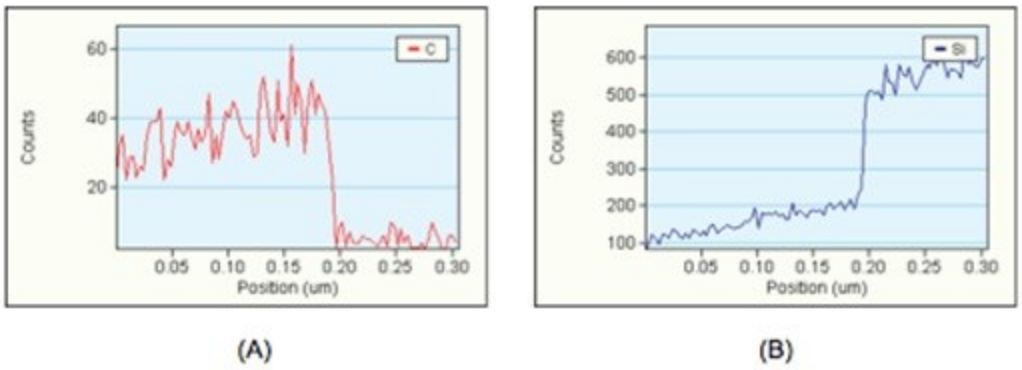

Figure 11: EDAX spectra taken of the *a*-SiC film. (A) Concentration profile of carbon as the electron beam is moved from the top of the *a*-SiC film to the substrate. The boundary between the *a*-SiC film and substrate is clearly visible. (B) Concentration profile of Si as the electron beam is moved from the top of the *a*-SiC film to the substrate. Data taken by Dr. Y. Emirof, USF NREC.

2.2.4 Optical Measurement

For device work that combines *a*-SiC coatings with waveguides and other optogenetics devices, the optical index was studied using a Filmetrix F20 optical profilometer. The technique measures the spectral reflectance of the light traveling back from the substrate to give both the thickness of the film and its optical index. The tool has a wavelength range of 380 nm to 1050 nm and the optical index measurements were all taken at 470 nm, a critical wavelength for optogenetics stimulation and fluorescence sensing.

It was shown that the optical index could be controlled slightly through the use of the precursor gas ratio during film growth. However, large swings in the index of refraction did not result (Table 3, Figure 12). The lack of change is consistent with the literature for precursor ratios in this range [42]. Future work may include alternating gas chemistries for successive layers to develop different effective optical indexes. Tuning of the optical index may allow for a much more versile process when coating waveguides and other optical system components.

Table 3: Precursor gas ratio vs. optical index

Run ID	CH4/SiH4 Gas Ratio	Index of Refraction
PASIC052112(A/B)	10.00	2.01
PASIC052112(C/D)	6.67	2.60
PASIC061412	6.67	2.40
PASIC080112A	12.46	2.30
PASIC081712A	24.00	2.28
PASIC081712C	36.00	2.28
PASIC090612A	22.60	2.28
PASIC090612B	35.00	2.28
PASIC092712A	30.00	2.28

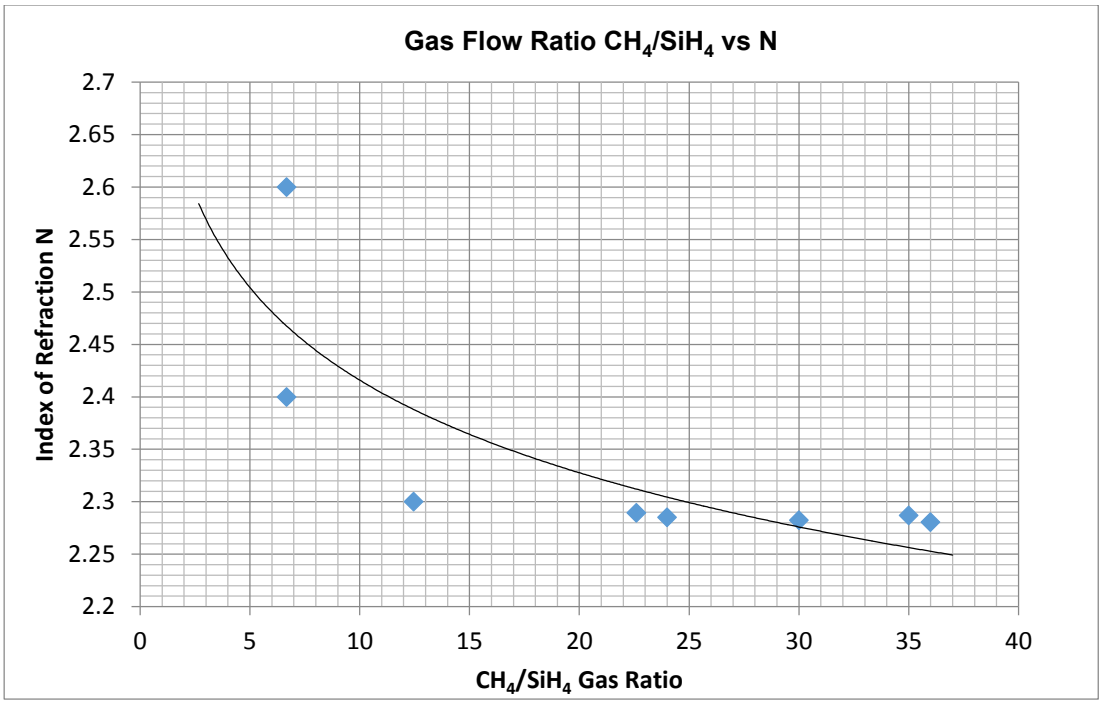

Figure 12: Influence of precursor gas ratio on index of refraction N. Data taken from PECVD-deposited *a*-SiC films in table 3.In the test CH_4/SiH_4 ratio is varied from 6.67 to 30.

2.2.5 Chemical Resistance

To perform chemical resistance testing of the *a*-SiC film, a solution of 40% hydrofluoric acid (HF) was used in an acid resistance test. Similar tests are conducted by others in the literature for SiC coatings [44]. The samples were submersed in the solution for 2 minutes at 25 °C to demonstrate acid resistance. After the test, the samples were imaged for subjective analysis and optically profiled to test for film etching. Early films with low CH_4/SiH_4 gas ratios ≤ 20 showed immediate delamination when subjected to the test and were not profiled due to the significant damage of the film (Figure 13). Later, the films showed no sign of delamination and also showed no appreciable etching after tested before and after for thickness using a Filmetrix F20 optical profilometer.

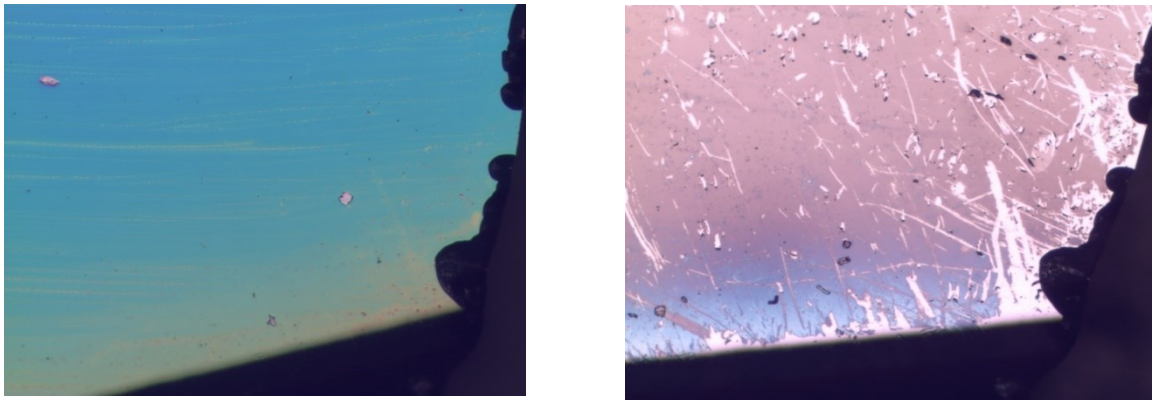

(A) (B)

Figure 13: Early acid challenge test for sample PASIC061412. Image (a) taken before 2 min 40% HF solution and (b) the resulting surface from the test. The film has clearly delaminated and etched away.

A clear trend between residual stress and chemical resistance was visible in the samples. As the stress was reduced the acid resistance increased significantly. When we had reached our lowest stress values (+/- 41 MPa), as seen in Figure 7, no appreciable etching was detected after the test. It is likely, however, that some chemical etching is still taking place. In the literature, standard *a*-SiC films etch rates for 40% HF are < 1 nm/hr so detection would take a much longer test [45].

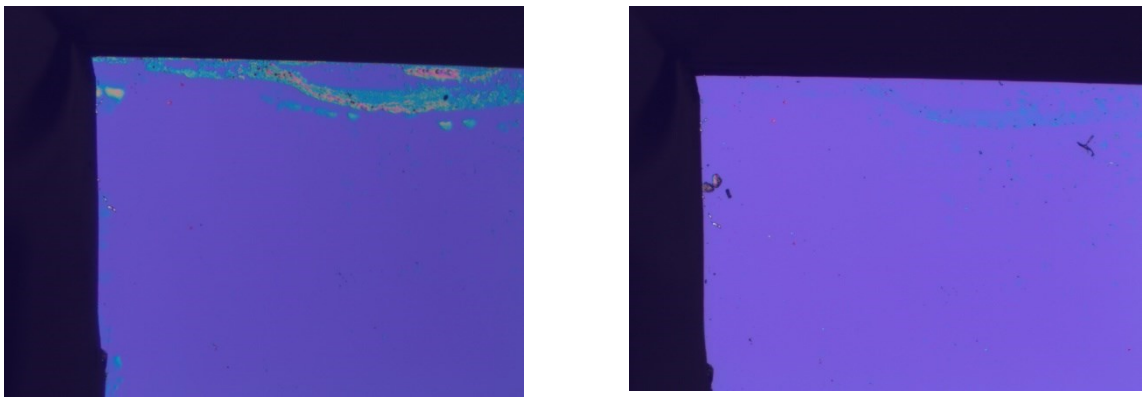

(A) (B)

Figure 14: Final acid chalenge test for sample PASIC061412. Later *a*-SiC films that showed lower residual stress had no appreciable etching or delamination when exposed to the HF acid challenge. (a) Image before the acid challenge of PASIC092712A and (b) After the test. The film shown here was optically profiled for thickness before and after by using a Filmetrics F20 profilometer which reported no detectable change in thickness.

2.2.6 XPS Data

XPS, or X-Ray Photoelectron spectroscopy, is a surface analysis technique where photoelectrons are ejected from the surface by means of a high energy X-Ray beam. The energies of the respective electrons are analyzed for their kinetic energy and plotted as a spectrum from high energy to low energy. Each measured binding energy provides a fingerprint that can be used to determine the presence and state of a particular atomic element or molecule. The number of electrons is counted for each species and this can be directly related to how much of that species is in the studied volume. With post processing, data peaks are fit to models which conclude on atomic species percentage per volume.

Film PASIC02212013 was grown using the process conditions shown in Table 2. The XPS survey from this film reveals a slightly carbon rich *a*-SiC material with ≈41.59% Carbon (1s peak), ≈34.47% Si (2p peak), and ≈23.9% O (O1s peak). It should be noted that these numbers are rough estimates given by the XPS software. The presence of oxygen in the data cannot be avoided in our current process due to chamber contamination. In the future work, it would be useful to work on creating a chamber used only for this purpose with a high vacuum system capable of thoroughly purging out oxygen. This may improve film density, and hardness.

The deconvoluted XPS data Si 2p flash shows characteristic peaks of Si-C bonding located at 102.4 eV alongside Si-0 bonding at 103.5 eV. Also, Oxygen is visibly present at 533 eV indicating oxidation of the sample. Although measures were taken to sputter clean the sample in Ar plasma before film deposition, this is to be expected due to the samples contact with atmosphere and residual oxygen in the chamber. The results have some ambiguity, as the O 1s and C 1s peaks seem to be present at 1 eV higher than those found in the literature [42]. This is likely, however, to be accounted for from surface charging due to the insulating nature of the *a*-SiC film.

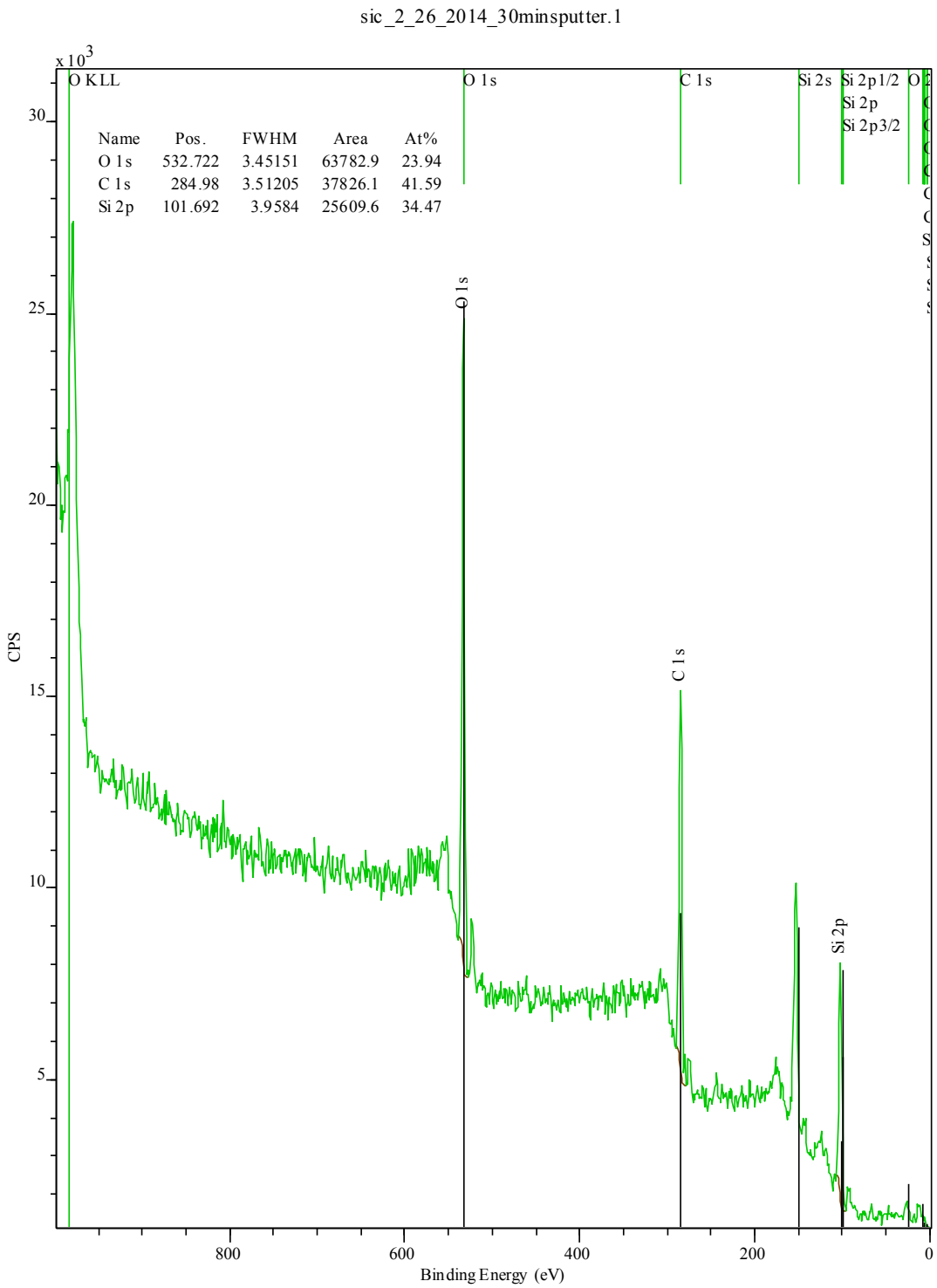

Figure 15: XPS survey of sample PASIC02212013. Sample grown with process conditions in Table 2. Data provided by Dr. James Lallo from Dr. Batzill's Interface and Surface Science Laboratory (ISSL).

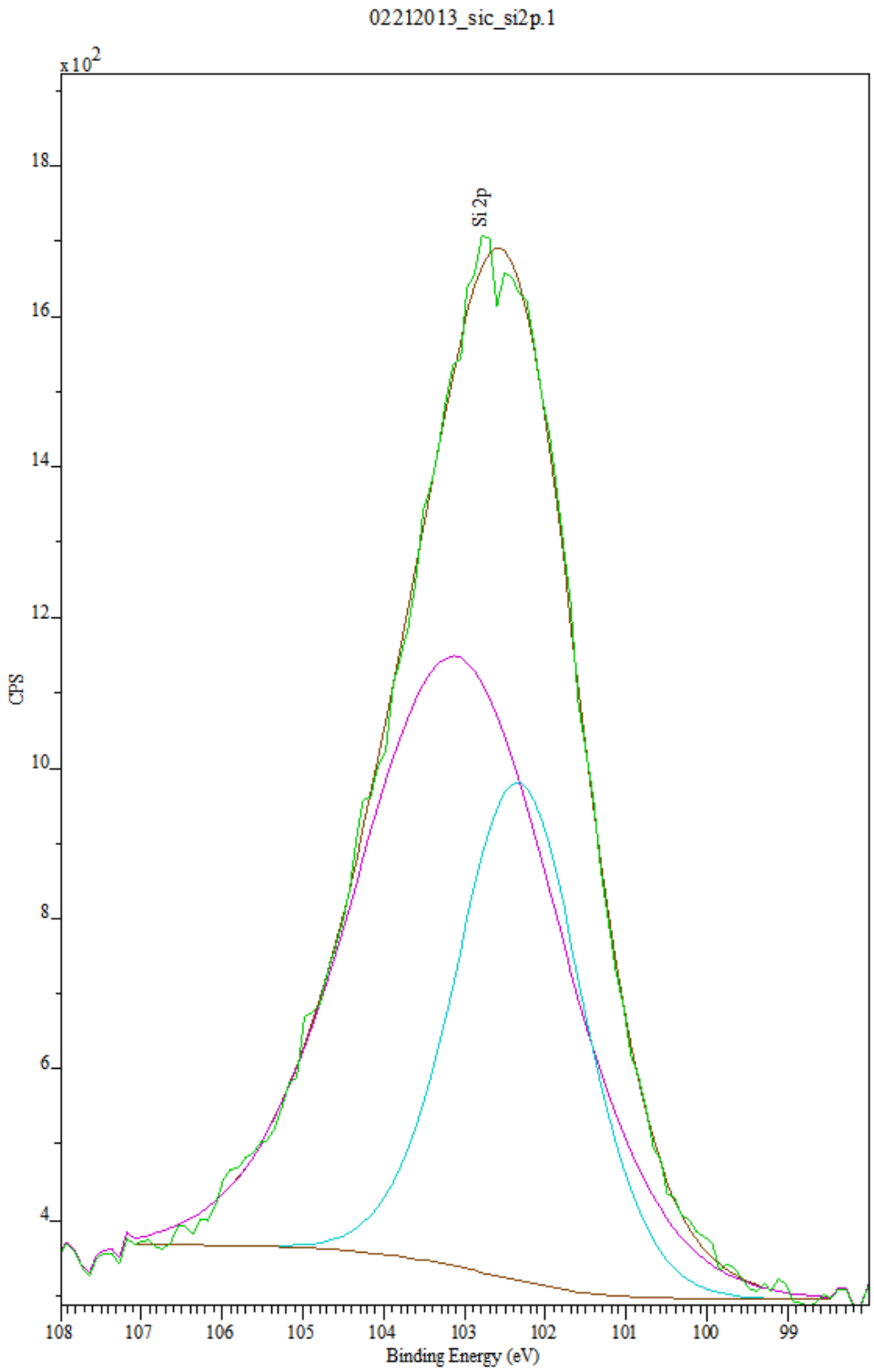

Figure 16: High-resolution XPS data from sample PASIC02212013. Sample grown with process conditions in Table 2. The Si 2p peak is evidence of Si-C bonding at 102.1eV. Data and analysis provided by Dr. James Lallo from Dr. Batzill's Interface and Surface Science Laboratory (ISSL).

2.2.7 Cytotoxicity Test

In work done by Maysam Nezafati of our group, cytotoxicity testing was performed on *a*-SiC samples produced with process conditions found in Table 2. Using immortalized NCTC clone 929 [L-929,derivative of Strain L] (ATCC® CCL-1™) mouse fibroblast cells, the material was studied for cell viability response. The test was performed via direct cell plating according to the guidelines generated by the International Organization for Standardization (ISO) in published standard ISO-10993-5. The *a*-SiC was deposited directly into silicon substrates and diced into 8 mm x 10 mm coupon samples. Calcein dye (1 mg/ml in anhydrous DMSO, life technologies) was used to detect live cells and ethidium homodimer-1 dye (EthD-1,2 mM solution in 1:4 DMSO/H2O, invitrogen) to detect dead cells. In the test 8 mm x 10 mm coupons of Cu and Polyvinyl chloride (PVC) were used as positive controls that show a reaction. Coupons of Au and polyethylene served as negative controls that show no reaction. In addition culture-treated polycarbonate coupons (CTPC) were used as a baseline material as per the ISO standard. To perform the analysis a Zeiss (Axio Image.M2m) florescence microscope was utilized for qualitative and quantitative evaluation of live/dead behavior of the cells. The *a*-SiC samples performed nearly as well as single crystal SiC and on par with Au coupons indicating that the material is biocompatible.

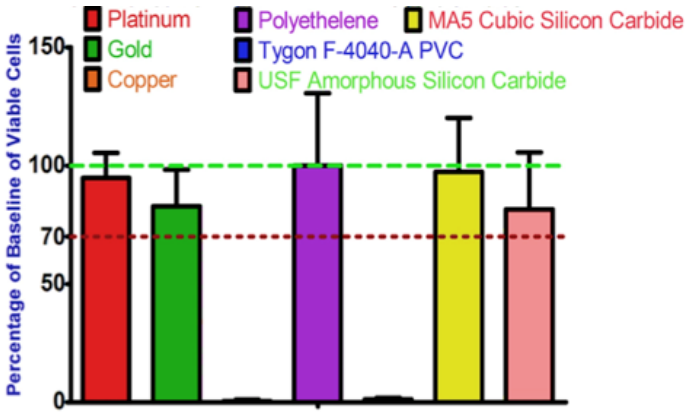

Figure 17: Comparison of viable cells on a-SiC as compared to baseline material. 0.8 cm^2 material tested in a 6 well plate. Data provided by Dr. C. Frewin, USF SiC Group.

2.3 Chapter Conclusion

The PECVD *a*-SiC process development was a success. A new low-temperature, low inherent stress process was developed for the coating and encapsulation of Biodevices. The process can be easily adapted to coat polymer substrates such as SU-8 and Polyimide.

For all processes, *a*-SiC was deposited using PECVD with a Plasmatherm 700. The system is retrofitted with a 13.56 MHz fixed-frequency source for plasma generation. It was found that adding an Argon plasma clean before the process enhanced adhesion to the substrate and reduced surface particles. The pre-clean is run at 50 W RF power and 12 sccm of Ar for 5 min. Many variations of the precursor gas ratios were attempted at 300 °C and 900 mT but through iterative testing, a gas ratio of 30 CH_4 to SiH_4 was found to reduce stress to a nominal amount and thereby increase adhesion and chemical resistance. At this precursor ratio the samples were tested for biocompatibility under the ISO-10993-5 standard and found to perform nearly as well as negative controls.

The final process is as follows: The process begins with initial pump down to 20 mT while heating of the sample holder to the nominal deposition temperature of 300 °C. To improve adhesion, an initial sputter-clean step is performed with a steady flow of 12 sccm Ar and a 50 W RF plasma. Next, the plasma is extinguished while precursor gas flows are established at a fixed ratio of 30 CH_4 to SiH_4 with Ar as the bulk dilution gas. Generally, the flows maintained are 360 sccm of CH_4, and 12 sccm of SiH_4, and 500 sccm of Ar. The chamber is maintained at a process pressure of 900 mT for the remainder of the deposition while maintaining the precursor ratio. Once gasses are stabilized, an RF plasma is struck and maintained with 50 W power for the entire duration of the deposition. The process deposits *a*-SiC at a rate of 4 nm/min. The process has been tested successfully down to 150 °C with some loss in adhesion and uniformity characteristics.

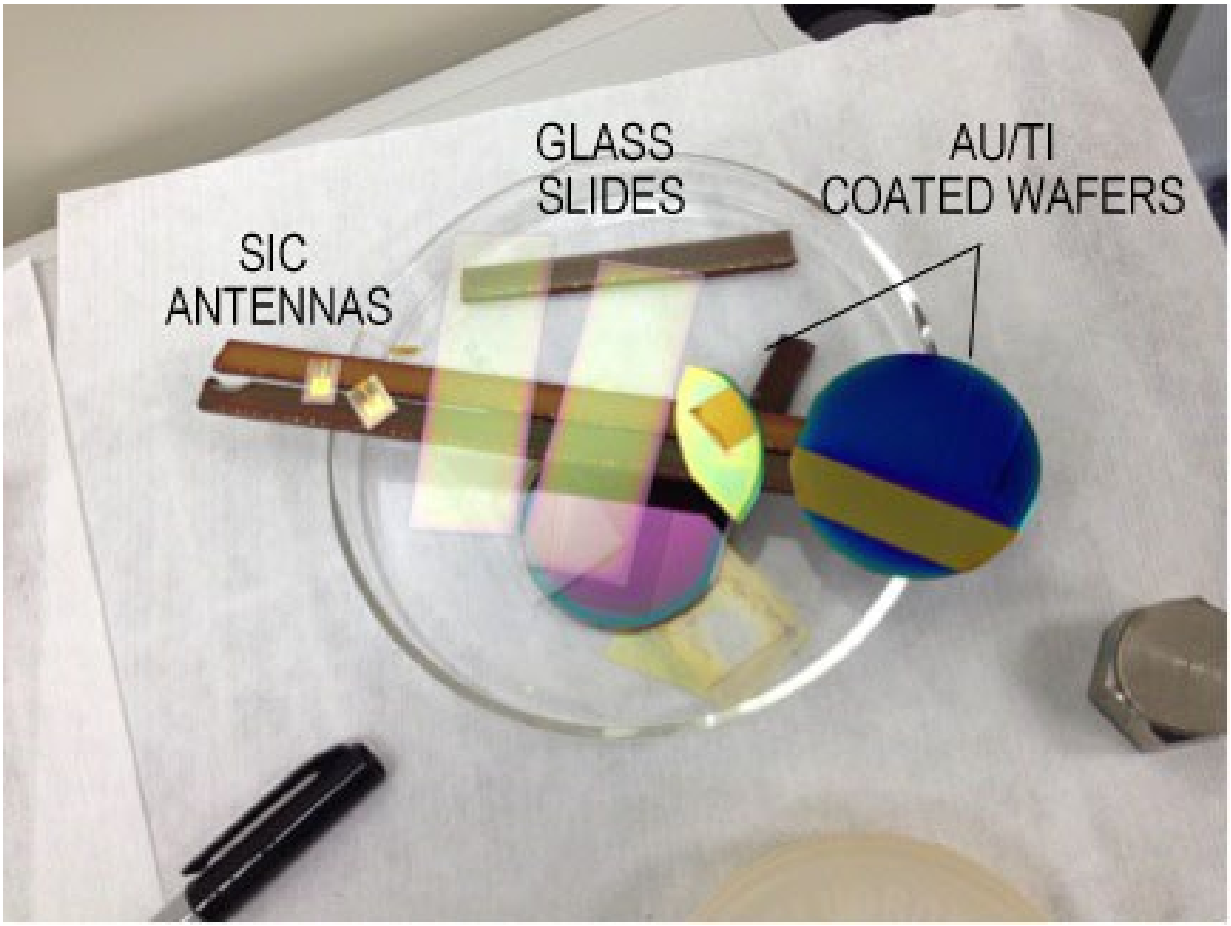

Figure 18: The *a*-SiC process can be adapted for a variety of substrates. Pictured here are several devices and substrates using the developed process.

CHAPTER 3: SIC FOR MICRO ELECTRODE ARRAY (MEA) DEVELOPMENT

3.1 Introduction

The neuroscience community benefits greatly by studying *in vitro* (cells) and *ex vivo* (brain tissue slice) neurodynamics and electrophysiology through long-term laboratory cultures. Typically these studies are performed using 2D microelectrode array (MEA) devices fabricated on silicon substrates using traditional microfabrication techniques. Silicon has been documented to cause glial scarring and has been shown to cause disruptions in neuronal cell cultures that may potentially skew the obtained data long-term [13], [46]. In our device, the silicon substrate is replaced with cubic silicon carbide (3C-SiC) providing an inert, biocompatible surface to allow for long-term neuroscience studies as well as a demonstration platform for long-term neural interfaces.

The presented microfabricated MEA consists of an array of 64 planar Ti/Au electrodes patterned directly onto a 3C-SiC substrate and on an oxide insulator for comparison. The small size of these electrodes (10 um in width) provides excellent spatial selectivity for neural recording and stimulation at the cellular level. The fabricated device was packaged in a 68-pin Pin Grid Array (PGA) style package and plugged into a custom interface board for signal processing and generation [ref Danilo book chapter]. The device and its associated support equipment are designed as a test bed for long-term neural recording and stimulation experiments *in vitro* and *ex vivo*. The device allows the testing of 3C-SiC substrates in active brain-like neuron environments as well as a test bed for brain-machine interface material studies.

The MEA device was primarily constructed as a proof of concept allowing for more sophisticated implants to be created in subsequent work. From the MEA device and its modeling we learned about electrode size, insulation materials, conductors, and worked out certain

fabrication steps that would have been more costly with implants due to the thicker 3C-SiC films required to realize free-standing probes (5-15 um typically). The MEA's require films of 3-5 um which are not only less expensive to manufacture but have less built-in stress and are of higher quality [47].

3.2 Electrode-electrolyte System

In this section, a simple point contact model of the electrode-neuron interface is developed to aid in component selection of the amplifier and design of the electrode system. The point contact model does not account for spatial distribution of charge and as such assumes that the potential outside the cell and in the solution are equal in all directions which generally holds true for simple planar microelectrodes.

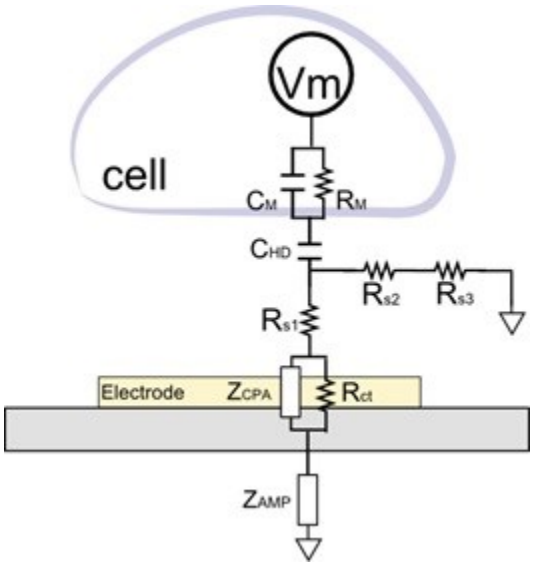

Figure 19: Overview of the point-contact model. Microelectrode impedance equivalent circuit where C_M and R_M are the membrane capacitance and resistance, respectively, C_{HD} is the double layer capacitance, and R_{S1}, R_{S2} and R_{S3} are to model the spread resistance Z_C.

To develop the model specific to our device, we first determine the impedance of the cell's outer membrane and develop a lumped element model. In this model, the cell membrane is modeled by a combination RC circuit of C_m and R_m in series with a capacitance for the electrolyte-cell membrane interface caused by the Hemholtz double-layer at the surface, which we call C_{HD}.

We first find R_m, or the purely resistive component of the cell membrane, using (3.1) where g_{mem} is the local membrane conductivity of 0.3 ms/cm^2 [48] and A_{ce} is the area of the electrode in cm^2:

$$R_m = \frac{1}{g_{mem} A_{ce}} \tag{3.1}$$

Next, we find the membrane capacitance in (3.2) using a value for capacitance per membrane area given in the literature as C_{mem}= 1 uF/cm^2 [48]. The membrane capacitance per area is then given by

$$C_m = C_{mem} A_{ce} \tag{3.2}$$

We then calculate the capacitance in the region where the cell membrane meets the surrounding electrolyte, or C_{HD}. This term represents the Hemholtz double layer and can be modeled using a three stage Gouy-Chapman sub-model [49].

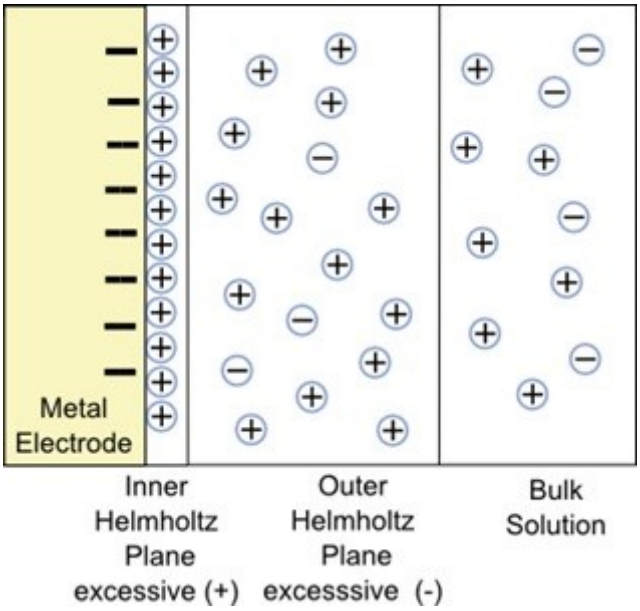

Figure 20: Regions of the Helmholtz double layer. Diagram details the three regions of the Helmholtz double layer showing the charge distribution for a standard metal electrode. The distribution forms a capacitance, C_{HD}, which is the Hemholtz capacitance

This model can be applied to low charge-injection conditions which is valid when the device is in recording mode. The sub-model breaks up the interfacial region into three separate

zones [50]. Each layer of the model will have its own capacitance and they are summed in standard reciprocal fashion to generate the value of C_{HD} (3.3).

$$\frac{1}{C_{HD}} = \frac{1}{C_{h1}} + \frac{1}{C_{h2}} + \frac{1}{C_d} \tag{3.3}$$

The first layer capacitance, C_{h1}, is the inner Helmholtz plane and is mostly made up of unhydrated ions. The next layer, C_{h2}, is composed of the interfacial region between the non-hydrated ions on the outside of the cell and the hydrated ions in the outer Helmholtz plane. While C_d is from the diffuse region where the electric potential decreases exponentially into the solution. The equations for each component are variations of a parallel plate capacitor and include terms to model the permittivity values in their respective regions [2].

$$C_{h1} = \frac{\varepsilon_0 \varepsilon_{lhp}}{d_{lhp}} * A_{ce} \tag{3.4}$$

$$C_{h2} = \frac{\varepsilon_0 \varepsilon_{OHP}}{d_{OHP} - d_{lHP}} \tag{3.5}$$

$$C_d = \frac{q\sqrt{2\varepsilon_0 \varepsilon_d kTz^2 n^0 N}}{kT} \tag{3.6}$$

where ε_0 is the permittivity of free space, and ε_{lhp}=6 and ε_{OHP}=32 are the permittivity of the inner plane and the outer plane, respectively. $d_{lhp=}0.3\ \mathrm{nm}$ and d_{OHP}=0.7 nm are the widths of the regions in the Gouy-Chapman model, K is Boltzman's constant, T is temperature in Kelvin, q is the charge on an electron, z is valence of the ionic species in the region, N is Avogadro's number, and n^0 is the bulk concentration of ions in the solution. The parameters used herein are material specific to a Au electrode but other metals will have a similar result.

Using equivalent circuit analysis, we combine the components discussed thus far into a complex equivalent membrane impedance given by

$$Z_m := \frac{1 + j\omega \cdot R_m \cdot (C_m + C_{hd})}{(1 + (j\omega \cdot R_m \cdot C_m)) \cdot (j\omega \cdot C_{hd})}; \tag{3.7}$$

Next, we want to establish the impedance for the spreading resistance denoted as $R_{s1\text{-}3}$ in Figure 19. These resistance values arise from the signal propagating outward through the

solution. The model in Figure 19 shows three separate resistances for the solution between the electrode and the cell's surface (R_{s1}) as well as a resistance to the surrounding solution (R_{s2}, R_{s3}). Our model assumes an equipotential in the solution, therefore R_{s1} and R_{s3} can be omitted. In the literature, it has been shown that if a cell covers the recording electrode R_{s2} can be approximated by (3.8) [51] as

$$R_{seal} = \frac{\rho_s}{\theta \pi d} \tag{3.8}$$

where $\rho_s \approx 1\ \Omega \bullet m$ is the typical resistivity of the electrolyte and Θ = 5.78 is a correction factor based on the geometry [2]. This simplified impedance now gives a single phase-independent parameter for the spreading resistance of the signal into the solution. In other words, for our model $Z_{seal}=R_{seal}$.

Finally, we develop a model of the impedance at the electrode interface with the solution. Z_{cpa} in Figure 19 can be found using the same Helmholtz capacitance parameters used in 3.4-3.6. The function for modeling this constant phase angle capacitance for the electrode is:

$$Z_{CPA} = \frac{1}{(j\omega C_{HD})^n} \tag{3.9}$$

where n is a parameter between 0-1 and represents surface irregularities. For our simulation we chose n = 0.9 based on the literature [2]. Also, an electrochemical resistance R_{ct} in the bottom of Figure 19 is the charge-transfer resistance to the electrolyte due to faradic interactions and is given as

$$R_{ct} = \frac{kT}{q}\frac{1}{zJ_0A_{el}} \tag{3.10}$$

where q is the charge of an electron and J_0 is the equilibrium exchange current density for the particular metal used. In the case of our model, Pt has a J_0 of 3.1 – log(A/cm^2). A_{el} is the area of the electrode and, for our model, we assume a cell completely covering the electrode such that $A_{el}=A_{ce}$.

Using simple circuit analysis the electrode impedance becomes

$$Z_{el} = \frac{R_{ct}}{1+R_{ct}(j\omega C_{hd})^n} \tag{3.11}$$

We now have the components required to create a more simplified diagram as shown in Figure 21 whereby we can replace each impedance component with a single complex impedance which is much more useful for modeling purposes and MEA design.

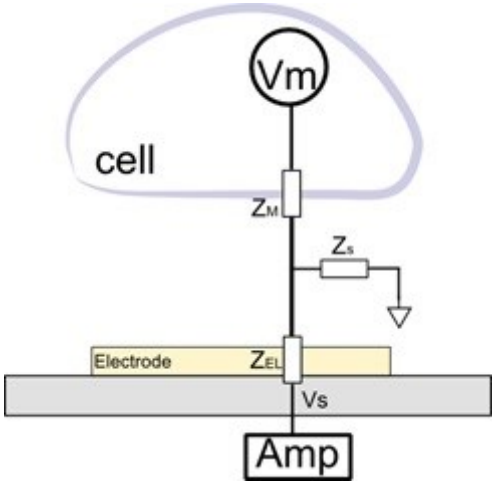

Figure 21: Neuron-electrode impedance model. Simplified Model of Neuron-Electrode Impedance where Z_M is the resulting membrane impedance, Z_S is the spreading resistance due to the solution, and Z_{EL} is the electrode impedance (typically on the order of 100 Ω for Au electrodes). Amp is the bioimpedance amplifier.

Further simplifying the model, we end up with a function for the complex input impedance as seen by the amplifier.

$$Z_{in} = Z_{el} + \left(\frac{1}{z_{seal}} + \frac{1}{Z_m}\right)^{-1} \tag{3.12}$$

This is to say that the impedance seen by the biopotential amplifier will be a parallel combination of the membrane resistance and the spreading resistance in series with the electrode's impedance, which is a result that we would have expected at the beginning based on standard circuit theory.

We use a computer math application (Maple 17) to plot the magnitude of Z_{in} over the potential range of neuron frequencies resulting in Figure 22. For our test case we assume a 10

um wide Au electrode and use the parameters from Appendix B. It is clear that the real impedance of the system drops as the frequency of the system is increased. This has been verified in the literature and is to be expected as the electrode system generally operates as a high-pass filter [52].

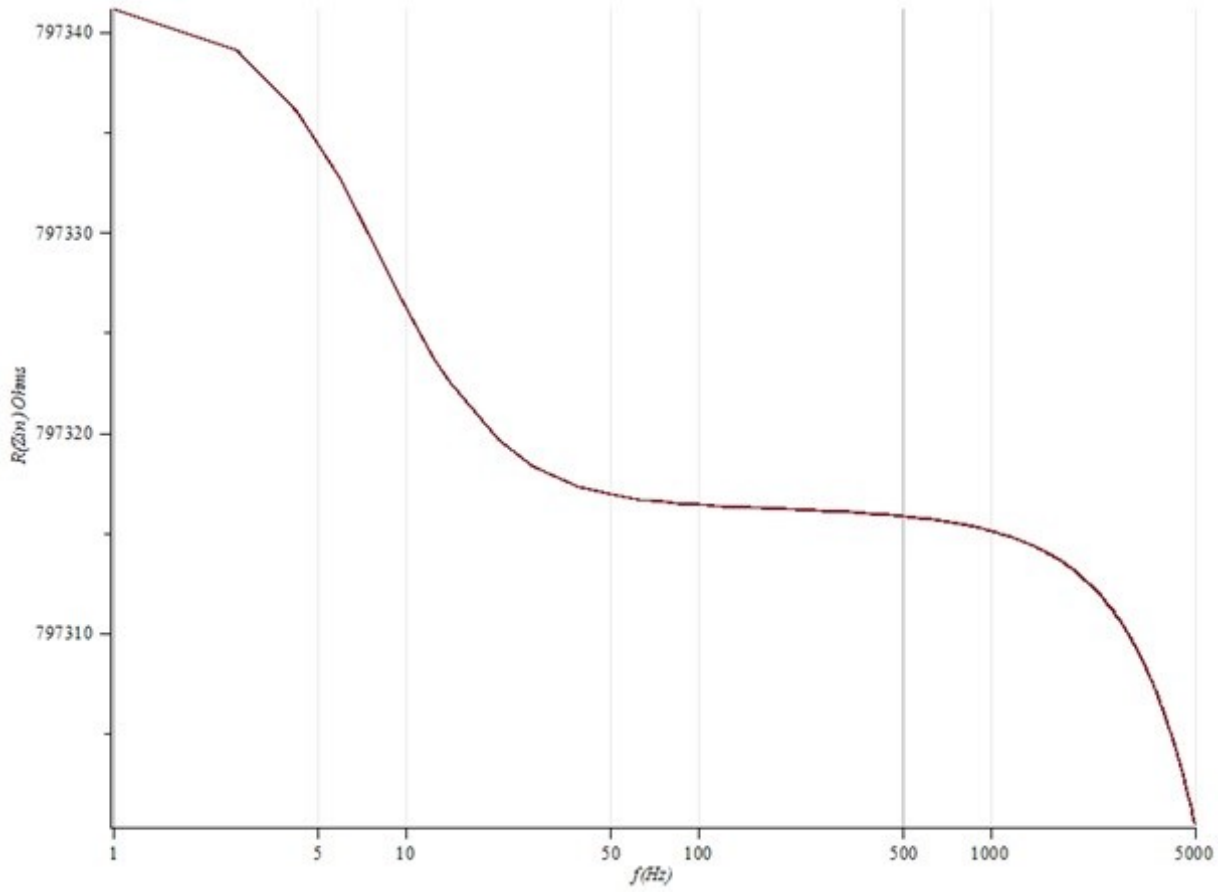

Figure 22: Impedance simulation based on the electrode-electrolyte model. Electrode impedance simulation based on the electrode-electrolyte model presented here. Shown is the Magnitude Plot of Re(Z_{in}) vs. Frequency from 1 Hz - 5 KHz. 1 KHz operating frequency gives a real load resistance of ~800 KΩ which is the approximate value used for MEA design purposes.

Plotting the capacitance using the imaginary part of the input impedance against frequency, you arrive at Figure 23. This allows a better understanding of what takes place as the system is driven with increasing frequency.

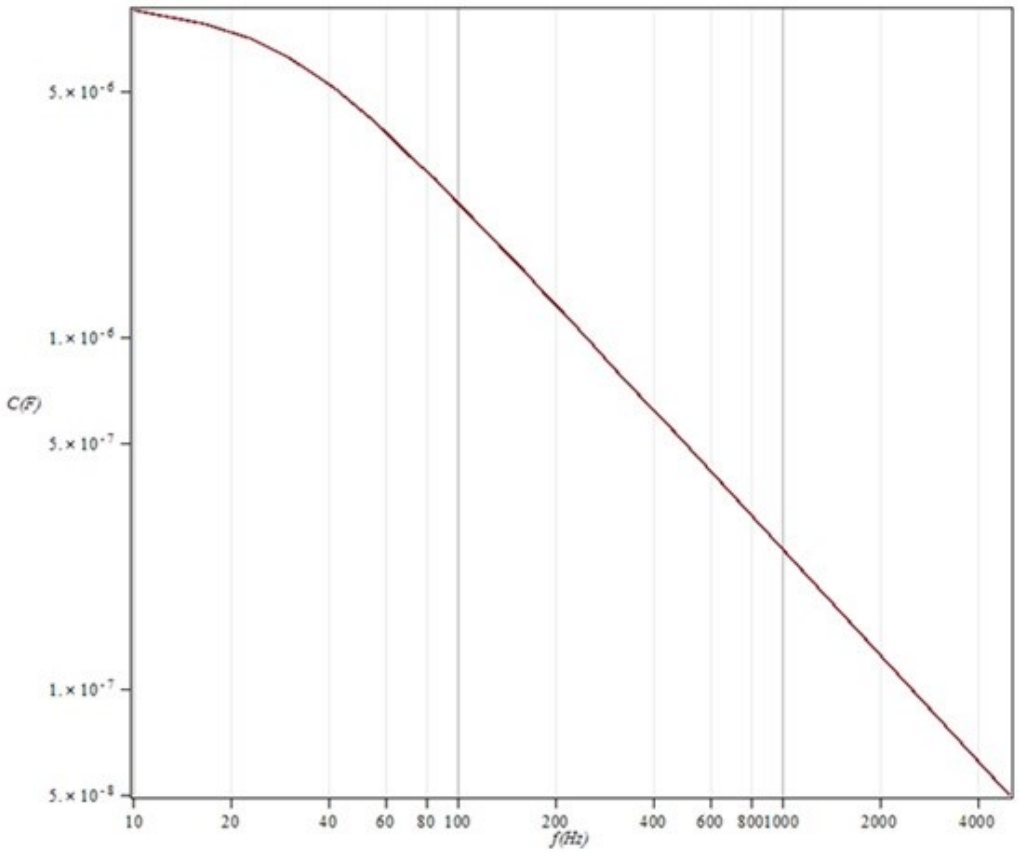

Figure 23: Simulated electrode capacitance (F) vs. frequency (Hz). At a 1 KHz design point the system has a predicted value of ~250 nF of capacitance.

In order to perform an analysis of the match of an amplifier to the impedance of the system we must define the input impedance of the amplifier. A 20 pF input capacitance was chosen and modelled as an imaginary reactive impedance Z_{load} (3.12). This impedance value is commonly used in such situations as many bioimpedance amplifiers exist near this range.

$$Z_{load} = \frac{1}{jwC} = \frac{1}{j2\pi f(20E-12)} \tag{3.13}$$

Next, a transfer function of the system was developed and the response of the system plotted in dB using (3.12). This helps us to better understand the factors in creating a quality interface to the neuron. As a design point we want to minimize the loss between the electrode and the amplifier in order to get the signal above the noise. The transfer function is shown in (3.14) and plotted in Figure 26 versus frequency:

$$H(s) = \frac{R_{seal}Z_{load}}{R_{seal}Z_{load}+(Z_m+R_{seal})(Z_{load}+Z_{el})} = \frac{Vs}{Vm} \quad (3.14)$$

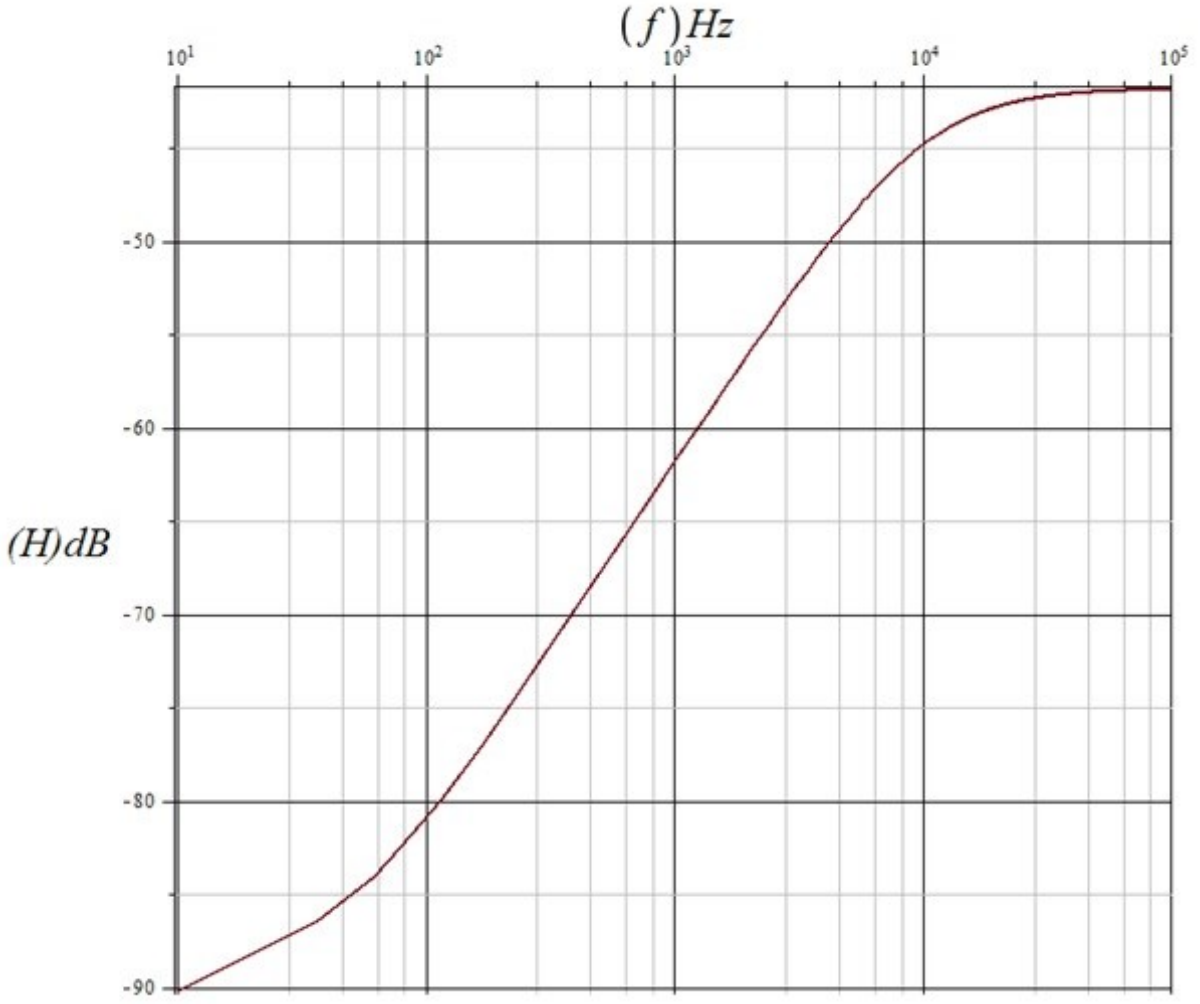

Figure 24: Transfer function of the electrode-electrolyte system. This simulation is for a 70 nm cell-electrode spacing and a circular Pt electrode of 10 um in diameter.

It is clear from Figure 24 that the overall system response is that of a high-pass filter. As the frequency increases the capacitive reactance lessens and begins to allow more signal amplitude. In addition the electrical phase of the system follows similar to what is expected in the literature for such a microelectrode system [2], [53].

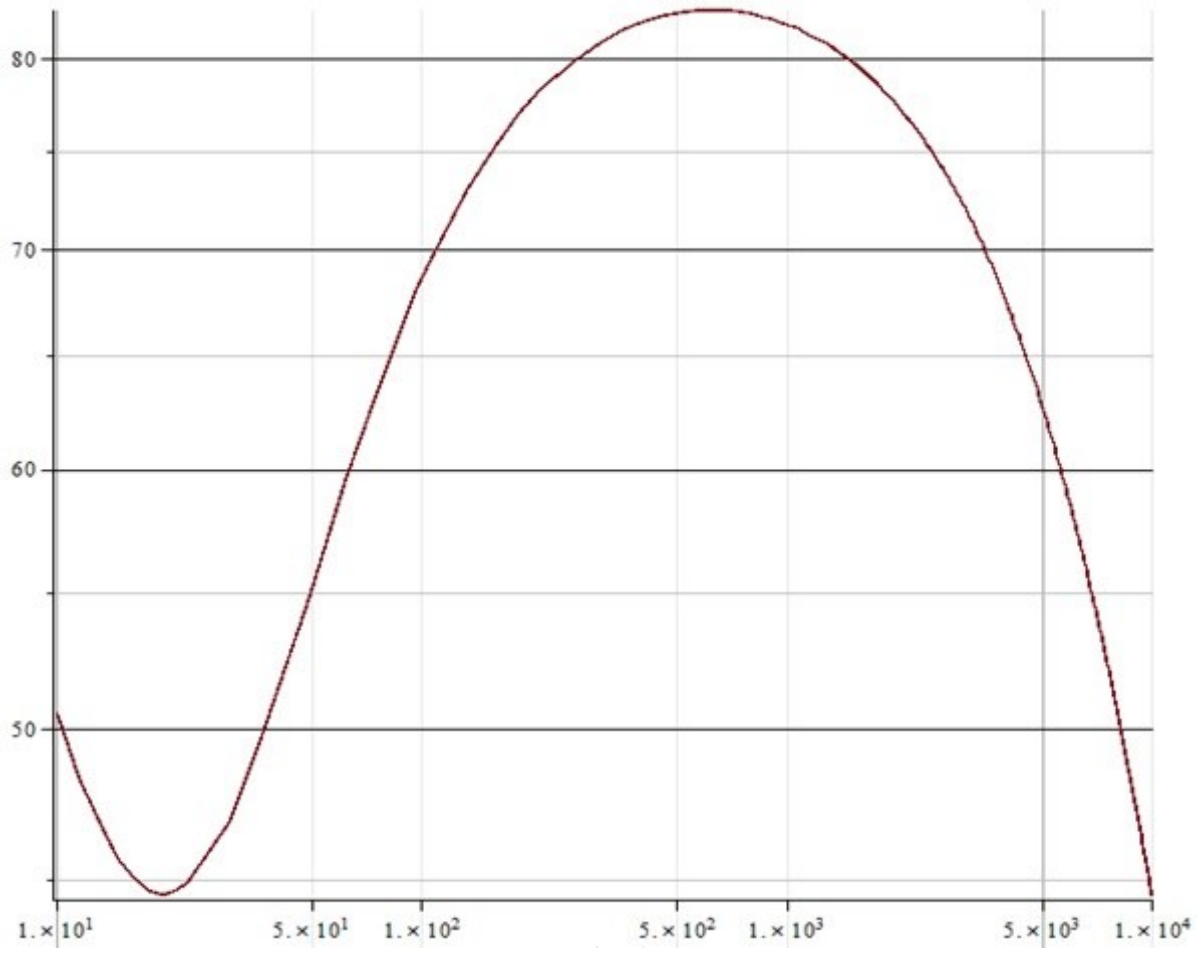

Figure 25: Simulated phase angle of the electrode-electrolyte system. Transfer function of Eq. (3.14). This simulation is for a 70 nm cell-electrode spacing and a 5 um wide Au electrode with a recording tip of 10 um in diameter.

In exploring the parameter space we would like to determine what the optimal size electrode would be using the model. To do this analysis we use (3.1-3.13), fix the cell diameter at a nominal value of 10 um, and increase the electrode diameter while plotting the frequency response of the system (see Figure 26 below). It is clear from the graph that as the electrode diameter increases the signal reaching the amplifier is less attenuated due to the influence of electrode area on R_{ct}. This trend continues until the electrode is roughly the size of the cell at which point the attenuation tapers off to an asymptotic value.

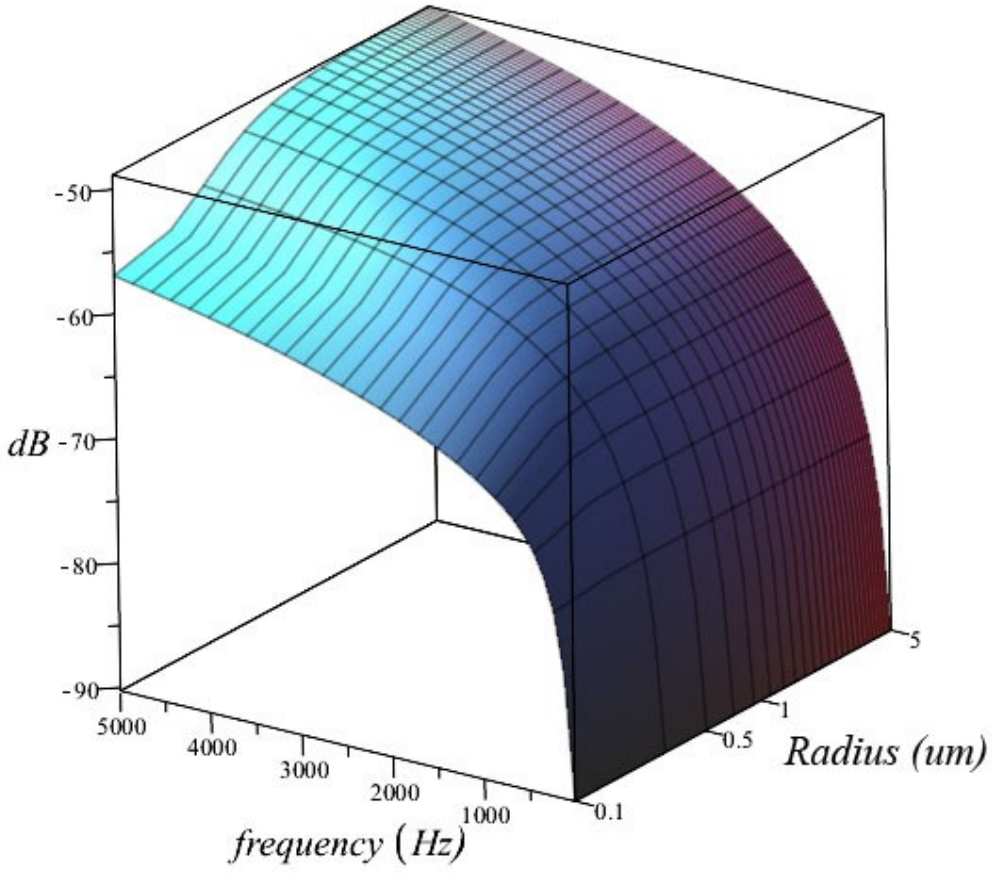

Figure 26: 3D plot of the diameter of a circular electrode (um) vs. frequency (Hz). Simulation of the electrode-electrolyte system showing a 3D plot of the diameter of a circular electrode (um) vs. Frequency (Hz) vs. Signal Amplitude reaching the amplifier (dB) for an Au electrode test case. Model used as presented here. Note the fairly flat response at 1 kHz for a circular electrode from 0.5 - -5 um in radius.

This dataset demonstrates that above a 5 um electrode radius there is no system benefit, with the caveat that this assumes a single neuron covering the electrode with the neuron diameter assumed to be 10 um. While creating electrode arrays, one must consider this as it seems that higher electrode densities and smaller electrode radii are best. However, due to assumptions and idealities of the model it may vary from the true system. One of the biggest factors affecting this outcome is that neurons are seldom perfectly aligned to the underlying electrodes and are of random size, albeit typically around 10 um. Therefore, by increasing the electrode area you

increase the probability of receiving the signal from a particular neuron. This probability could, however, be increased by reducing spacing and increasing the number of electrodes to get a more ideal case so there is clearly a trade-off between the probability of recording neural activity from a single electrode and recording the same activity from an ensemble of electrodes. A more sophisticated 'system level model (beyond the scope of this dissertation) is clearly needed to address this issue.

3.3 Micro Electrode Array (MEA) Fabrication

As a test bed for fabrication strategies of neural recording electrodes, a microelectrode array (MEA) system was realized. To accomplish this goal, we used conventional lithography and processing to create gold-electrode MEAs on both SiC and SiO_2 coated 3C-SiC substrates. The two substrates would allow for future testing of neuron cell proliferation on these surfaces. This work is a stepping-stone to a fully implantable recording SiC neural probe, but has independent merit as mentioned in the introduction to this chapter and so it is discussed here.

The neuroscience community has a need for studying neurons *in vitro* in long-term cell cultures. Typically, these studies are performed using 2D MEA devices fabricated on silicon or glass substrates using traditional microfabrication techniques. Silicon has been documented to cause glial scarring and disruptions in neuronal cell cultures that may potentially skew data from long-term neuron cultures so it is likely that SiC substrates would help the problem in the exposed substrate regions near the electrodes. Glass has similar, albeit reduced, effects and likewise SiC MEAs would provide benefits to long-term in-vitro studies.

The designed MEA consists of 64 planar Au electrodes patterned directly onto the substrate. Using the analysis from (2.2.4) a small electrode diameter of 10 um was chosen with a spacing of 150 um thus providing excellent spatial selectivity for neural recording of individual single units.

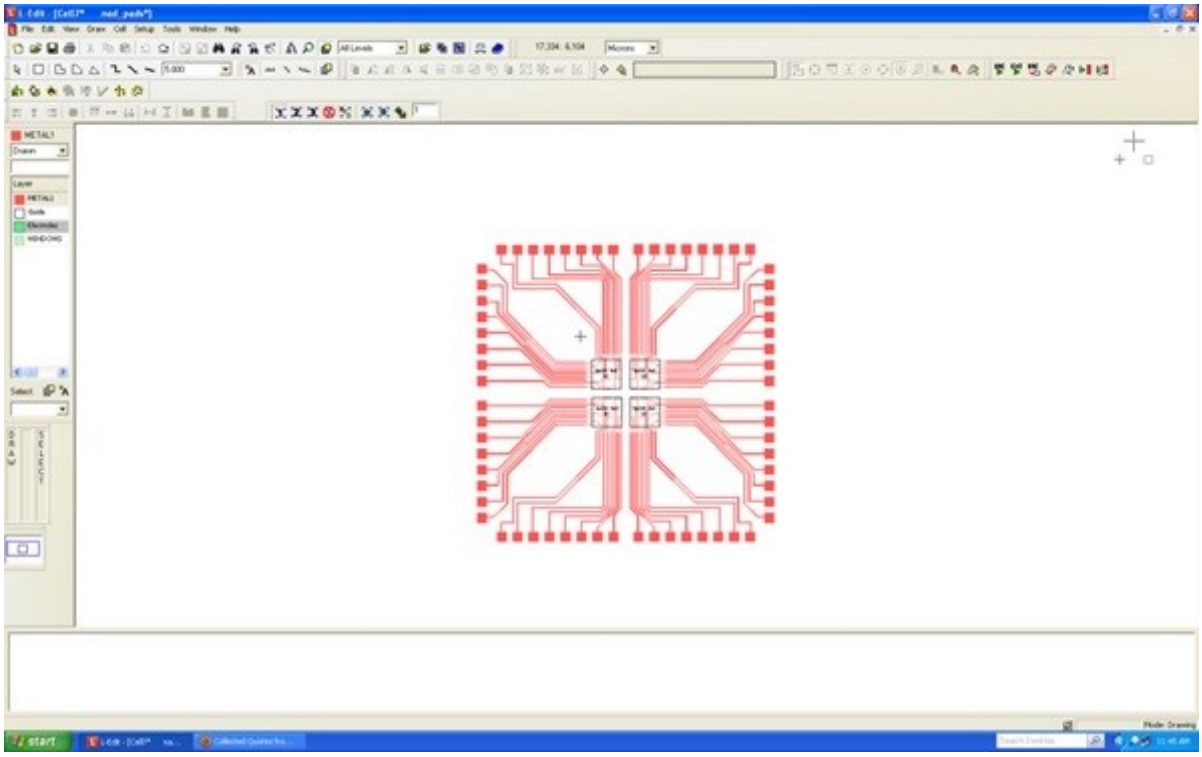

Figure 27: MEA device layout (64 electrodes). Layout was performed in Tanner Tools L-Edit software and exported for mask creation. Pictured here is a single die that was then repeated over an entire 4” wafer field. The die dimensions are 1.2 cm x 1.2 cm.

Gold metallization layers were chosen in these initial devices. This was primarily a fabrication-driven decision. Other metals, such as Pt, may make better electrode candidates. However, they require significantly more processing due to the difficultly in etching and plating the materials. Gold shows reasonable biocompatibility, low protein absorption, and high electrical conductivity. The metal layer can easily be substituted in future work. The MEAs were designed using 2000 Å gold layers. At this thickness, the layer provides a low resistance path through the trace. Trace resistance can be found using equation 3.15.

$$R = \rho * \frac{L}{T * W} \tag{3.15}$$

where the resistivity of gold is 2.44E-8 Ω•cm, L is length, T is thickness, and W is trace width. In the case of the designed device the 2000 Å trace metallization layer at 5 um in width resulting in

a resistance per length of 2.4 Ω/cm. This allows us to neglect this resistance as a design constraint as the solution resistance alone, R_s, will be in the range of several kΩ.

The devices were fabricated using standard lithography using the following process: First, CVD 3C-SiC substrates were epitaxially grown on (100) Si substrates which were cleaned using standard RCA cleaning procedures and then the surface was prepared using an O_2 plasma at 50 W for 5 min to remove any contaminants that may hinder metallization. For the oxide on 3C-SiC MEAs the samples were then coated with 3 um of PECVD SiO_2 for substrate isolation. For both the 3C-SiC and oxide coated 3C-SiC substrates 200 Å of Ti was deposited to serve as an adhesion layer followed by 2000 Å of Au for the metal interconnects and electrode conductors. Next, the samples were patterned with AZ4620 photoresist applied by spin coating at 2000 RPM for 30 seconds and immediately soft-baked at 90 °C for 5 min.

The wafers were then allowed time to rehydrate for a minimum of 2 hours before proceeding to the following lithographic steps. A small amount of water is needed in the following photoreaction. The humidity in the ambient environment is used to rehydrate the wafer. As a general guideline, 10 min of rehydration is used per micrometer of photoresist however in very thick films the water diffusion slows and this step can take several hours.

Next, they were aligned in a Quintel mask aligner and patterned using UV exposure. Once the samples were developed in 1:4 AZ400K solution, the gold was etched off in TFA Au etchant. This completed the metal trace structure fabrication process.

To insulate the traces from each other SU-8 2005 negative resist was spun onto the devices at 2000 RPM resulting in 5 um thickness. This layer is also patterned using the Quintel mask aligner under UV exposure to form the device insulation. This layer was then hard-baked at 100 °C for 20 min. In a final step, the individual die were cut from the wafer using a wafer dicing saw with a high-speed carbide blade. This resulted in loose MEA die ready for packaging.

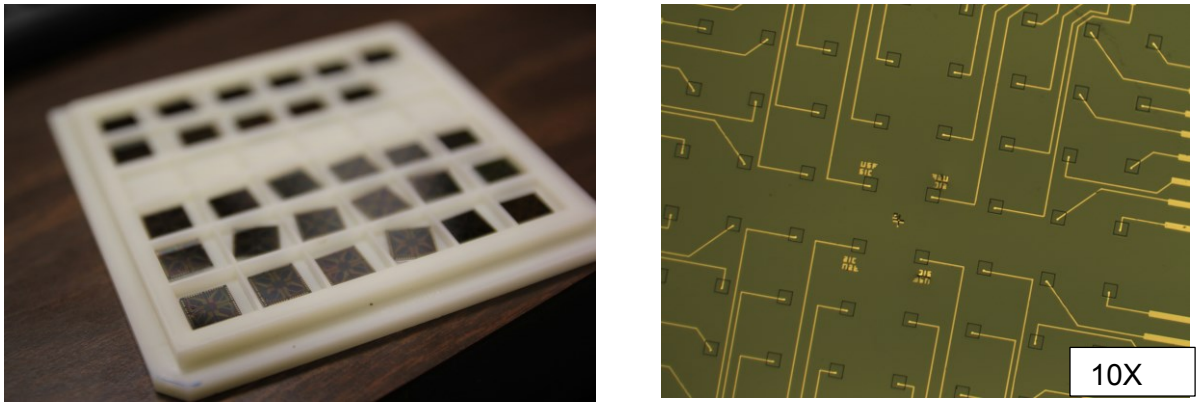

(A) (B)

Figure 28: Optical micrograph showing MEA die after processing. (A) Carrier tray used for sorting defective die and (B) 10x optical micrograph of the active area on the completed MEA at 10x magnification. Clearly visible are the 50 um square recording windows and the 10 um diameter Au electrodes.

3.4 Device Packaging

The finished MEA devices were bare die with small 300 um x 300 um bond pads for connecting wires to the package. In order to facilitate convenient supporting electronic connections, the bare die needed a chip packaging solution. The package chosen was a ceramic 68-pin Pin Grid Array (PGA) style package. The ceramic material would allow for inexpensive heat sterilization techniques to be used on the device and provides a rugged enclosure for repeated handling. Our MEA chip connects to 64 out of the 68 available package connections whereby the extra package leads were left floating. We then cleaned the samples again to avoid contamination caused by the dicing saw process. The MEA die were then sent off to a Quik Pak, Inc. in Saint Albans, VT for epoxy die attach mounting and automated wire bonding. The chip die were wire-bonded into ceramic PGA 64 Packages so that they could later be heat-sterilized before cell plating.

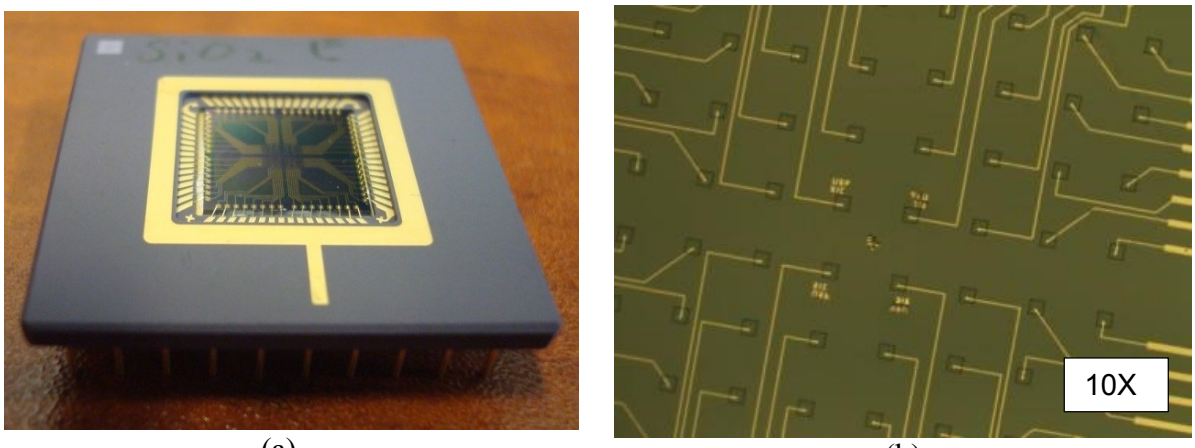

(a) (b)

Figure 29: Final packaged MEA devices. (a) MEA chip held in place with epoxy adhesive and wire bonded to a PGA 64 package. (b) Optical micrograph of the MEA center region viewed at 10 x magnification for reference.

Upon receiving the bonded devices, the wire bonds and ceramic package are exposed to the environment. If the devices were used in this state the PBS solution used to support the neurons would short out adjacent bond wires and the ceramic package may leach cytotoxic materials into the culture. To negate this, liquid containment wells were formed using Slyguard 184 Polydimethylsiloxane (PDMS). The active area of the MEAs were protected with a rubber block held in place with adhesive tape (see Figure 30(a)). The encapsulant was also applied to isolate and protect the gold wire bonds on the perimeter of the device. The well formed by the encapsulant also provided a cell culture area to hold PBS when performing cell experiments.

While PDMS encapsulate is generally considered biocompatible, In the future, MEA devices produced by our team will likely replace this step with a glass cylinder coated in *a*-SiC from the process outlined in Chapter 2. This would better isolate any cytotoxic response caused by the MEA well itself. By using the a-SiC coated glass material the data can be less confounded as materials are eliminated.

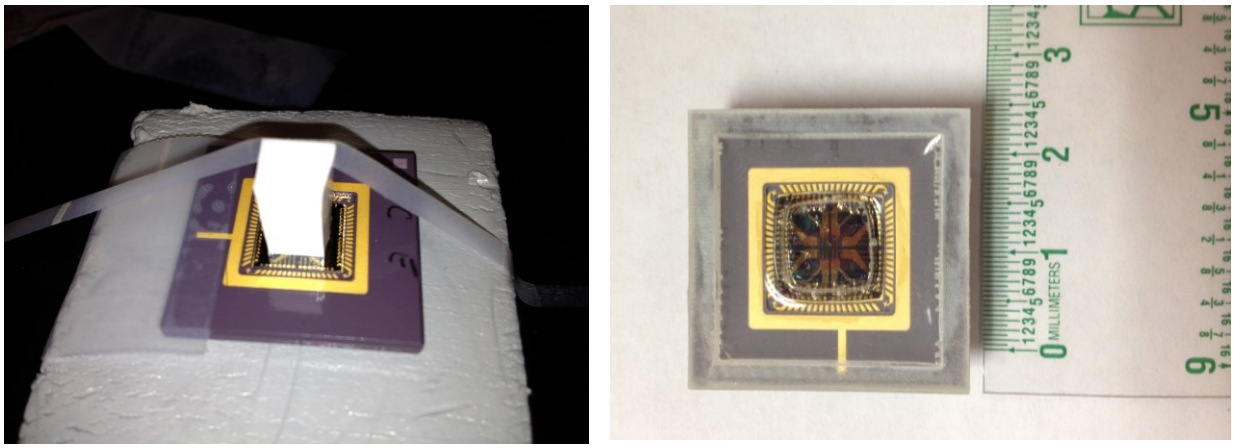

(A) (B)

Figure 30: MEA fluid well fabrication using PDMS. (A) a rubber block was used to protect the MEA active area during encapsulation and (B) A finished MEA device with the PDMS containment well and wire-bond encapsulant shown after curingd. Ruler shown for scale.

In addition, our team developed a PCB board for the MEA to connect to the auxiliary electronics using its 64 channel PGA footprint. The PCB board contained several 0.1mm spacing pin headers that could be used with standard shielded ribbon cables for signal stimulation and recording (Figure 31). The Cadence Eagle 3.6 design tool was used to layout the PCB and silkscreen artwork.

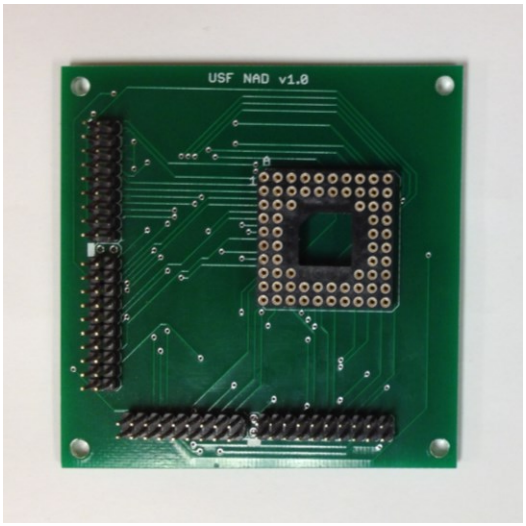

Figure 31: MEA carrier and breakout board. Board used for connecting stimulation and recording electronics. Board layout was performed by Justin King, USF, and the board produced by an off-site vendor.

3.5 MEA Validation

After fabrication, the devices were tested for impedance across a range of frequencies that covers the full frequency range of evoked action potentials EAPs. The measured data was then compared to the calculated data from the model presented in section 2.2.4. This allows us to simulate the 64 channel MEA system without using electrically excitable cells to verify functionality. The model is similar to the one presented in section 3.2. For simplification, the inner Helmholtz plane distance is neglected by setting d_{lp} to zero [2]. In addition, the frequency dependent Warburg impedance element was included to better model the low frequency response of the electrode [54].

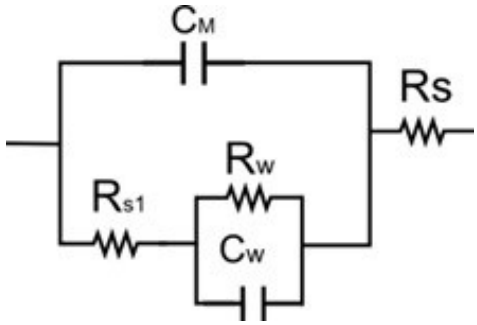

Figure 32: MEA electrode electrochemical equivalent circuit model.

The fabricated MEA devices were measured by introducing standard phosphate buffered saline (PBS) solution to the PDMS well above the device. PBS is a water-based salt solution that matches the pH and approximates the salt osmolarity seen within the body. The measurement was made though the custom PCB board interface using a silver wire counter electrode directly in contact with the solution. This allows us to test the response of a single electrode in the PBS solution. The wire is assumed to have an area large enough to negate interfacial effects and act as a direct connection to the surrounding solution. The device was then connected to a HP 4294A Impedance analyzer in two-point configuration for frequency response analysis. The HP 4294A is an auto-bridge impedance analyzer capable of measuring systems from 40 Hz up to 110 MHz.

For our tests, the analyzer was set for 100 mV stimulation potential and a maximum frequency of 5 kHz.

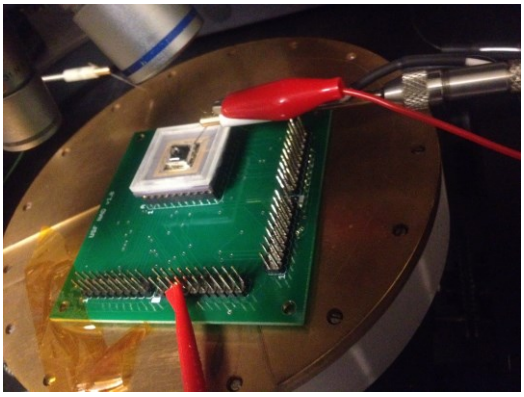

Figure 33: Oxide on 3C-SiC MEA under test. Measurement of electrical impedance of single electrodes performed using a silver reference electrode in PBS solution (wire visible at end of probe tip over MEA above). An HP 4294A impedance analyzer was used, settings of 100 mV signal amplitude swept from 40 Hz to 5 kHz.

Three electrodes were randomly selected on the MEA for measurement of |Z| and all three showed a good fit with the impedance model through using regression analysis as shown in Figure 32.

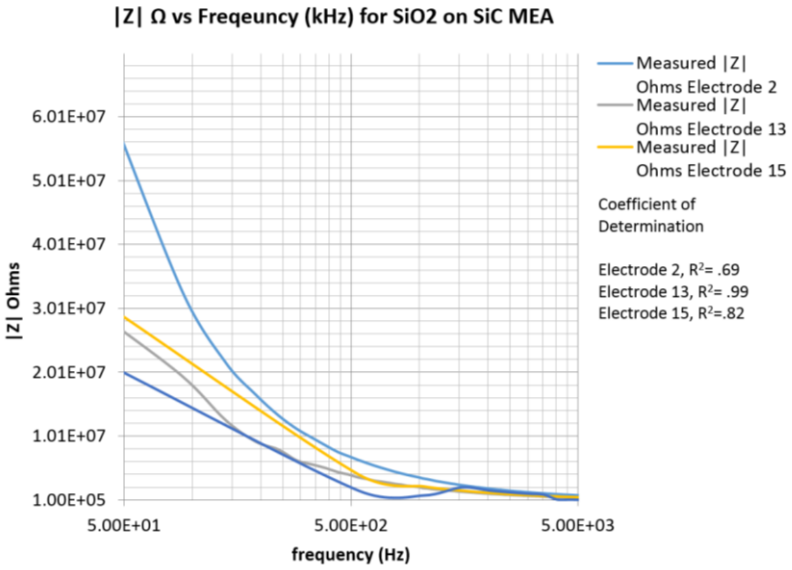

Figure 34: Impedance magnitude data |Z| vs frequency (Hz) of MEA electrodes. Data taken from three randomly chosen single electrodes on the oxide on 3C-SiC MEA and plotted against the circuit model shown in Figure 31.

The regression values are shown indicating, with the exception of one electrode, excellent fit with the model of section 3.2. In the figure, one electrode (electrode 2) seems to deviate causing a lower R2 value of 0.69. This outlier may be due to microfabrication or mask alignment errors or other yield-limiting issues.

Data was taken in the same setup for phase information and plotted with respect to frequency (Figure 53). Here, again, the data seems to work well with the model with the exception of a single electrode. Overall, the model fit is a success and thus validates the model so that it can be used as a basis for future designs. Phase information can be somewhat more difficult to accurately measure in the 2 point configuration used for the measurement. Further work will be performed with a 3 port electrochemical analyzer to avoid phase error. However, in spite of this, the measurement demonstrated R^2 coefficients of .95, .91, and ,.05 for electrodes 1, 7, and 10. The low coefficient of determination for 10 is likely due to device insulation failure.

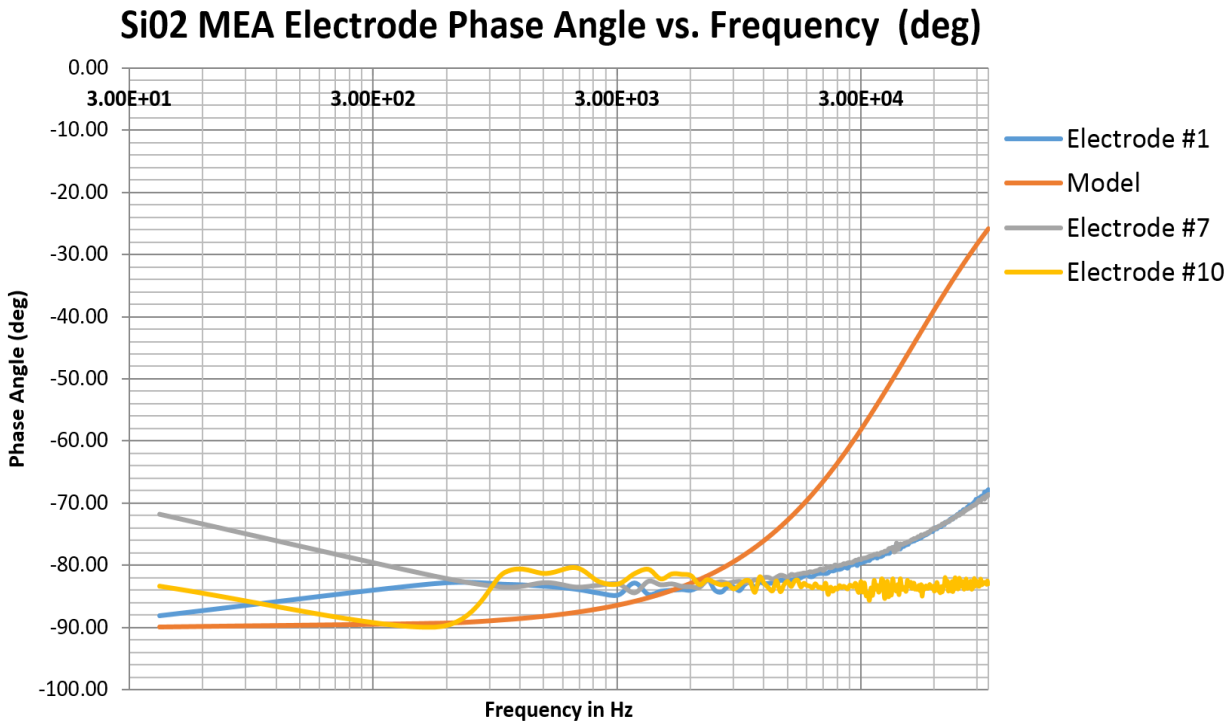

Figure 35: Impedance phase angle (degrees) vs frequency (Hz). Data taken of three randomly chosen single electrodes.

3.6 Conclusion

MEA devices were microfabricated from SiC substrates with gold electrodes as a platform for learning the tools and techniques required for more complex neural implant designs. The fabricated oxide on 3C-SiC MEA adequately follows the impedance model given. We therefore can draw conclusions from the circuit analysis of the electrode-electrolyte interface given in section 3.2. Extending this to the plot of gain of the transfer function in Figure 24 we get some basic requirements for the amplifier system as well so that a fully-functional 3C-SiC MEA system can be realized based on this work.

The system amplifier would need to have ≈ 60 dB of gain at 1 KHz to give a 1 V nominal signal amplitude to the analog to digital converter used in the system. Most biopotential amplifiers designed for microelectrode work provide well over 100 dB [55], thus this is not a difficult design specification to meet. The 3C-SiC MEA system and its associated fabricated support equipment will be used in future research by the group in advanced biomaterial research. In particular some novel materials concepts were developed to allow for an oxide-free 3C-SiC MEA and this will be discussed in further detail in Chapter 6 in the future work section.

CHAPTER 4: TOWARDS THE DEVELOPMENT OF SIC BASED OPTRODES

4.1 Introduction

Silicon carbide is a particularly good candidate biocompatible material for optrode development. The single-crystal form hVE been proven to work well in neuronal cell cultures and has optically transparent polytypes for the creation of waveguides. In amorphous form, the material can be used for highly insulating coatings to isolate conductors from each other and the surrounding bio-environment. These advanced devices would likely improve long-term cell recordings and lessen chronic implantation damage observed with currently used electrical stimulation techniques.

This chapter outlines our efforts to advance the state of the art of optrode development through using SiC-based biomaterials for functional or tissue-contact components. To achieve this goal, new processing techniques were developed and the project culminated in an implantable integrated device with optical waveguides, metallic electrodes, and *a*-SiC insulation.

4.1.1 SiC for Optogenetics

Data was collected on the optical transmission properties of several SiC polytypes for a head-to-head comparison near the critical wavelengths needed for optogenetics. The three polytypes tested (6H-SiC, 4H-SiC, 3C-SiC) were chosen because of preexisting biocompatibility work done by our team. Those studies showed the 3C-SiC polytype as the clear winner of the biocompatibility race followed by 4H-SiC and 6H-SiC [56]. In addition, 3C-SiC seems to be the most economical and readily available polytype since it can be grown epitaxially on Si substrates via chemical vapor deposition.

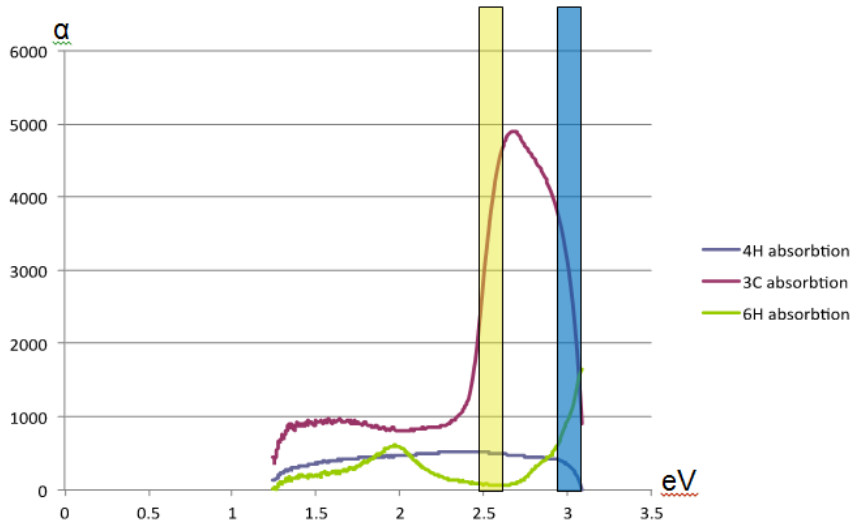

Figure 36: Absorption coefficient, α, vs. photon energy, eV. A graph of the measured Absorption Coefficient, α, vs. Photon Energy, eV. At T=296 K for various polytypes of SiC. Measurement taken with a Filmetrex F20 at NREC, USF. For reference the blue optogenetics activation and yellow quenching wavelengths are shown. Unfortunately, and as expected, 3C-SiC has too narrow of a bandgap to serve as a suitable optical waveguide.

To determine the feasibility of using SiC for light guiding components, the collected samples were then tested in a Filmetrix F20 retrofitted with a T-1 stage for measuring transmittance between 380 nm - 1050 nm. This allowed sufficient coverage of the visual spectrum covering all major optogenetics spectra. The experiments were performed in a lighted cleanroom environment with baseline calibration to remove ambient light effects. Absorption data was calculated from the raw transmission values. The transmission of the three polytypes is shown in Figure 39 as a function of photon energy (eV).

Optical propagation loss in these semiconducting materials is dominated by absorption of the material with a small amount of loss from crystal defect scattering. Generally, light energies that exist below the material's bandgap energy are transmitted while those that exist above are heavily absorbed. It was evident in our data that the most neurocompatible polytype, 3C-SiC, fails as a suitable waveguide core material for ChR2 due to its heavy absorption near 473 nm (2.62 eV). However, it is noted that NpHr light centered at 580 nm would pass nearly unhindered. The 4H-SiC and 6H-SiC have sufficiently high bandgap energies to avoid heavy absorption

characteristics. These materials make good waveguide core materials and leave the possibility for 3C-SiC overgrowth for enhancing biocompatibility.

Although our simple study was done with respect to the two most common opsin proteins, it should be noted that a wide variety of opsins for neuron activation and inhibition exist. Currently, the list of available opsin proteins expands every few months and provides an ever-growing menu of wavelengths, chemical kinetics, and temporal precision. For example, VChR1, which is another channelrhodopsin variant of ChR2, has a red-shifted activation wavelength. The center frequency for VChR1 is 590 nm, which corresponds to a photon energy of 2.1 eV (near yellow). At this wavelength, the attenuation of the 3C-SiC polytype is greatly reduced and would work as a possible waveguide material.

4.1.2 Modeling Light Delivery

In order to explore light delivery a simple model was developed for light propagation through brain matter. The model includes optical losses due to scattering, Fresnel loss, and geometrical loss. In actuality, some absorption may occur, but it is several orders of magnitude below that of scattering loss and is thus neglected.

Scattering light through brain matter can be modeled using a Kubelka-Munk model for diffuse scattering material. The Kubelka-Munk model describes light scattering in a uniform solid using monochromatic light with no outer reflection boundary [57]. Generally, at low optical power outputs this model will hold true deep within the brain thereby making it a useful approximation for optogenetic devices (4.1).

$$T = \frac{1}{Sz + 1} \tag{4.1}$$

where the parameter T is the transmission fraction of light reaching the region of tissue that is a distance z (mm) away from the optical source. The parameter S is a scattering coefficient per unit of thickness.

Geometric loss from the emitter can be modeled using Snell's law to calculate the half-angle of the divergence for the waveguide (4.2):

$$\theta_{div} = sin^{-1}\left(\frac{NA_{wg}}{N_{tissue}}\right) \tag{4.2}$$

where N_{tissue} is the index of refraction of the surrounding grey matter. To compute the numerical aperture we derive the following relationship from 4.3:

$$NA_{wg} = \sqrt{{N_{core}}^2 - {N_{clad}}^2} \tag{4.3}$$

We then calculate the illumination intensity emitted from the end of the waveguide by dividing the total optical power by the cross-sectional area of the waveguide emitter:

$$I(0) = \frac{P_{src}}{W * H} * A_f \tag{4.4}$$

where P_{src} is the source power of the system, H is the height of the rib waveguide and W is the width of the emitter end of the waveguide. A_f is a term to summarize the losses up into the end of the waveguide. This term is developed experimentally and contains both propagation loss and Fresnel loss.

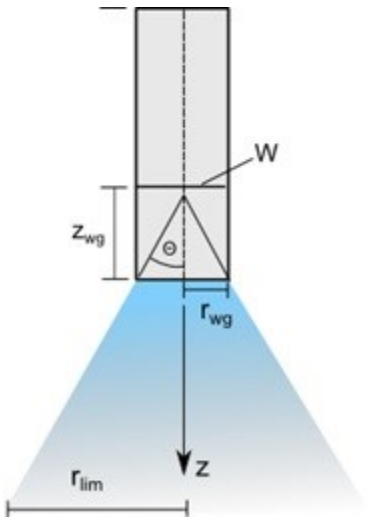

Figure 37: Diagram of optical emission from a multimode waveguide. r_{lim} is the radius of the emitted light at a distance of z from the end of the device, z_{wg} is a distance used for calculating beam geometry, Θ is the half-beam angle, and W is the width of the waveguide.

Combining the geometric decrease of light from the tip of the waveguide and adding the effects due to scattering, we arrive at a model for light intensity vs. distance. This equation was adapted from [58]:

$$\frac{I(z)}{I(z=0)} = \frac{\rho^2}{(Sz+1)(z+\rho)^2} \tag{4.5}$$

$$\rho = r_{wg} * \sqrt{\left(\frac{n}{NA_{wg}}\right)^2 - 1} \tag{4.6}$$

To calculate the volume of light emitted we use a cone approximation (Figure 37):.

$$\frac{1}{3}\pi z_{wg}({r_{ilm}}^2 + r_{ilm}r_{wg} + {r_{wg}}^2) \tag{4.7}$$

Using 4.1-4.7 we perform an analysis of the optical stimulation of tissue. We use a reported value of the index of refraction for grey matter, N_{tissue}, of 1.36 for mouse models [59]. Values for the scattering parameter S have been reported in the literature for mice as 11.2 mm^{-1} for a mouse cortical tissue and 10.3 mm^{-1} for a rat cortical slice at 473 nm [58] [59]. These values for the animal models follow closely to scattering values measured in humans [60]. We use a value of 57% that was determined experimentally by coupling a small 473 nm laser to a 100 um optical fiber and dividing the input power by the output power. This value is supported by similar results in the literature [61]. In addition, the test case uses a polymer waveguide made from photo curable SU-8 epoxy coated in SiO_2 for a cladding layer, a typical biocompatible material stack used in neural prosthetics. A value of N_{cor} ≈1.6 is used for SU-8 while the index of PECVD SiO_2 is derived from the literature [62][63]. To simplify the calculation, a square waveguide cross section is assumed.

The minimum activation light intensities that have been documented in the literature for ChR2 and NpHr opsins are ≈1 mW/mm^2 and ≈21.8 mW/mm^2, respectively [29][58]. These parameters provide a limiting condition for the analysis of activated tissue emitted from the waveguide.

If the input power level, P_{src}, is held at 20 mW and we plot the light intensity vs. distance from the light emitter, we observe ChR2 activation out to ≈ 1 mm within the brain tissue. The intensity of that light within the tissue is plotted in Figure 38.

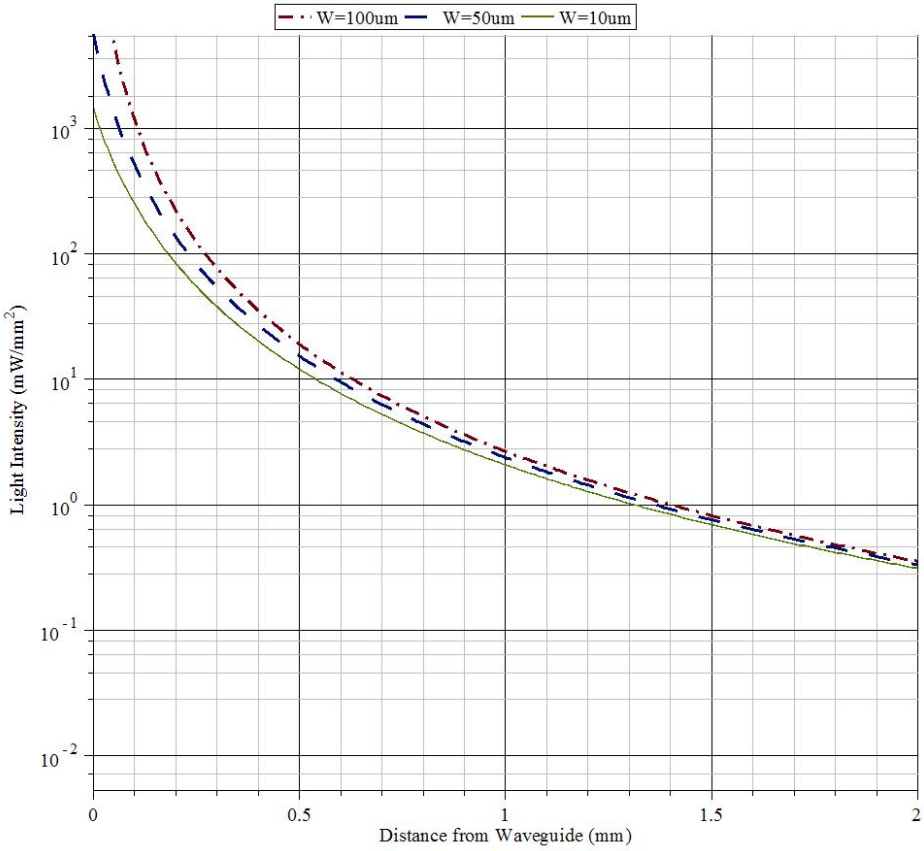

Figure 38: Light intensity vs. distance from the emitter tip in mm. Dataset uses 20 mW input source, 0.43 Numerical Aperture (NA), a coupling efficiency, A_f, of 57%, and assuming grey brain matter with an optical index of 1.36 with a scattering coefficient, S, of 10.

It is clear from the figure that the bulk of the power dissipates in the first 500 um of tissue. This result is verified by the literature in transmission experiments performed on mouse brain slices by work done by Aravanis *et. al* in 2007 that show 90% reduction of resulting intensity from the first 1 mm of grey matter [58].

Next, we continue our analysis by comparing how the volume of activated tissue relates to both the width of the rib waveguide and the initial input power P_{src}. The same assumptions as above apply and the equation set was solved for 1 mW, 10 mW, 15 mW, and 45 mW input power.

It is important to note that the coupling efficiency, A_f, was held constant for the simulation but due to real-world geometric constraints this parameter would likely modify the result somewhat.

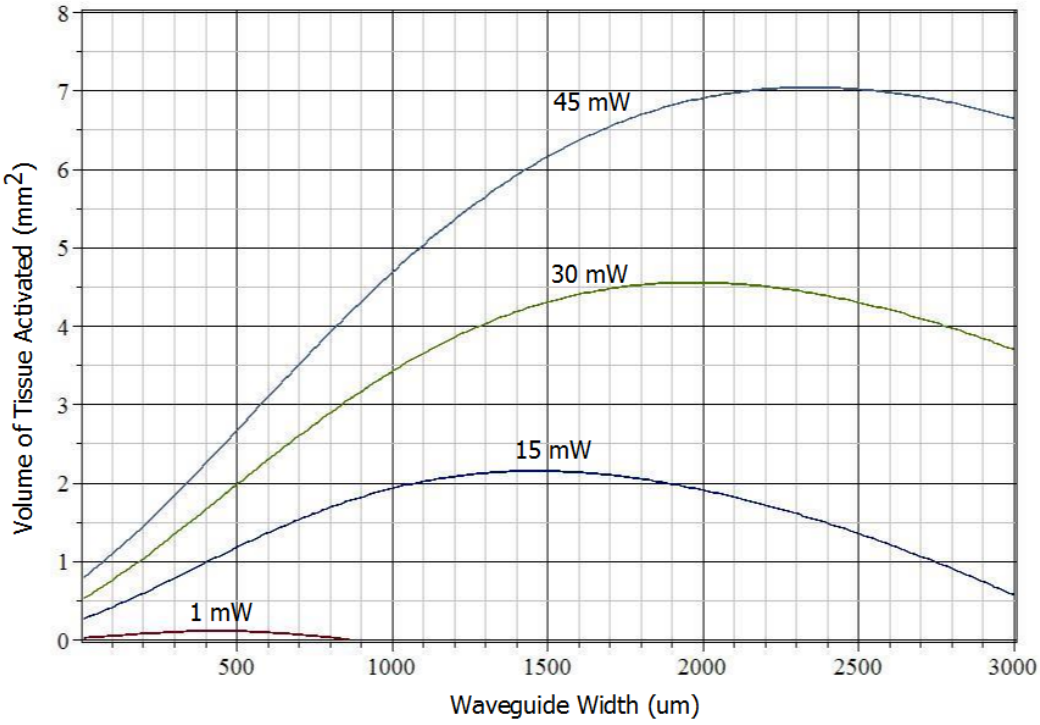

Figure 39: Power level vs. activated tissue volume. Calculation of power level impact on resulting activated tissue volume for various waveguide dimensions. Dataset uses a 0.43 Numerical Aperture (NA) calculated for a SU-8/SiO_2 waveguide, and assumes a constant coupling. Power levels as indicated.

The result is somewhat surprising, each power level input into the system results in an optimal waveguide area to get its respective maximum volume of activation. As the waveguide area increases, more light is coupled into the system due to the increasing area of the input end of the waveguide. However, as the output area increases so does the volume of the emission cone. This increasing volume becomes the dominant factor and the tissue activated begins to decrease again due to a lack of intensity on the emission surface. For the microfabricated waveguides investigated within this dissertation the waveguide diameters of 1-3 mm may be entirely too large for use in an animal research model. To minimize trauma and maximize overall

biocompatibility the overall device thickness is minimized, but the simulations act as a guide in which to compare optical source coupling techniques and analyze overall system efficiency. The numbers are simply given as an exploration of the parameter space and do provide a useful framework from which to conduct our optrode design.

4.2 SiC Fabrication Challenges

Epitaxial 3C-SiC wafers have very high intrinsic stress (tension) values that make them exceedingly difficult to process due to the 22% lattice mismatch between the SiC structure and the structure of the film [64]. This high stress makes the use of traditional micro electrical mechanical system (MEMS) techniques difficult. The inherent film stress causes wafer bow that prevents proper alignment in patterning, hinders wafer bonding by trapping air pockets, and often results in wafers fracturing when using vacuum chucks to hold the substrates during processing. To address these concerns, several measures were taken.

First, stress was minimized as much as possible in the initial substrate by using the (100) orientation of silicon as it results in slightly less stress than (111) Si substrates. In addition, the 3C-SiC growth process using an optimized carbonization step resulting in a very thin, but highly defective interface layer that can accommodate much of the strain [64].

Mechanically, it makes the most sense to use smaller substrates to minimize the effective curvature. By dicing the large 4” diameter substrates into 1” squares we reduced the height deviation from the horizontal plane as seen by the vacuum chuck surface. The smaller substrates allowed for the use of standard 2” vacuum chucks while minimizing the total height deviation over the width of the sample. This technique, however, comes at the cost of a more irregular edge bead from the spinning of photoresist and SU-8 layers, as well as greater difficulty in aligning subsequent layers.

In the final steps of fabricating SiC optrode devices the Si is removed through inductively coupled plasma (ICP) etching. As the substrate thins, the balancing compressive force it provides lessens and this causes the 3C-SiC on thin Si film to pull away from the handle wafer. This effect

can often be dramatic leading to delamination of the handle wafer from the substrate and subsequent severe buckling and cracking of the film. Proper bonding of the handle wafer to the film is necessary to prevent this from occurring during the back-side Si etch.

To further complicate device fabrication, 3C-SiC has no effective chemical etchants other than molten KOH salt. Therefore, inductively coupled plasma (ICP) is used. The use of ICP as a primary etch technique requires careful planning of the fabrication process to ensure the delicate microfabrication portions of the device are never exposed to the harsh high-energy plasma directly. Normal neural probe fabrication generally relies on chemical etching or oxide release layers which are not an option for single-crystal 3C-SiC based probes.

4.3 Waveguide Design

Ideally, the optical waveguide system of the optrode would be entirely made out of single-crystal SiC materials due to both its optical properties (section 3.1.2) and biocompatibility results seen with the material [56]. The processing requirements of fabricating these structures from this bulk material (4H- or 6H-SiC) are known to be extremely difficult and overly expensive for the purpose of the dissertation. Therefore, a viable alternative was found, and fabrication of these hexagonal-SiC waveguides will be left as future work. Instead, we will proceed with a polymer waveguide made from SU-8 with an *a*-SiC encapsulation layer in the hope to have both ease of fabrication and biocompatibly, thus leading us to a more realistic near-term SiC-based optrode.

SU-8 polymer also has evidence to support its biocompatibility in neural tissue, is optically transparent, photopatternable, and can be coated with PECVD *a*-SiC, through low temperature processes, to prevent its dissolution into the surrounding tissue [65]. Therefore, the material was chosen as a viable alternative and was used in conjunction with 3C-SiC substrates and *a*-SiC dielectric coatings. Hard-baked SU-8 has an inherently low optical index of 1.67 and, therefore, cannot be used directly in contact with *a*-SiC without significant optical loss. Therefore PECVD SiO_2 served as both an intermediate adhesion layer and optical cladding for the optical

waveguide. Figure 42 shows the realized SiC optrode with the various material layers and their corresponding indices of refraction.

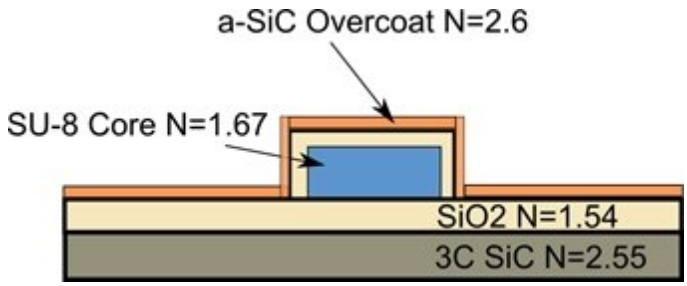

Figure 40: Developed biocompatible optical waveguide geometry. An a-SiC over layer was used to ensure material robustness and biocompatibility. The oxide layer serves as the required low-index cladding layer and the waveguide core is made from SU-8 photopatternable polymer.

4.4 Fabrication of Test Waveguide Structures

Multimode waveguides were fabricated from SU-8 polymer and clad with PECVD SiO_2 and *a*-SiC biocompatible encapsulation. Standard contact lithography was used to first create linear test structures of 50 um in width and 20 um in height.

The fabrication process begins with the growth of 3 um of PECVD SiO_2 at 250 °C on a substrate material. Next, the wafer is plasma cleaned in an O_2 Plasma for 30 min at 200 W to help with the removal of any organic material as well as to terminate the surface for better adhesion of subsequent layers. In addition, the surface is cleaned using a mixture of 3:1 concentrated sulfuric acid to 30% hydrogen peroxide solution (Piranha Etch). Once clean, the wafer is then dehydrated by placing it on a 200 °C hotplate for 30 min to remove any residual water or solvent on the surface. It is important to note that without this step adhesion to the underlying glass substrate is poor causing the structures to delaminate in subsequent processing. Next, MicroChem SU-8 2010 photopolymer is spin coated onto the substrate using 1000 RPM for 30 sec resulting in ≈20 um of material. The wafer is then soft baked at 90 °C for 5 min to remove solvent and reduce stress from the film. Masks were made from laser printed acetate and were acquired through Advanced Reproductions, Inc. The wafers were patterned using a Quintel Mask aligner. Exposure dose was found to be 201 mJ of broadband UV through experimentation. The resulting structures

were then hard-baked at 100 °C for 20 min. The process was repeated to create multiple samples. Control samples were kept with no cladding, while another group were deposited with 3 um PECVD SiO_2 cladding, and others the full material stack shown in (Figure 40).

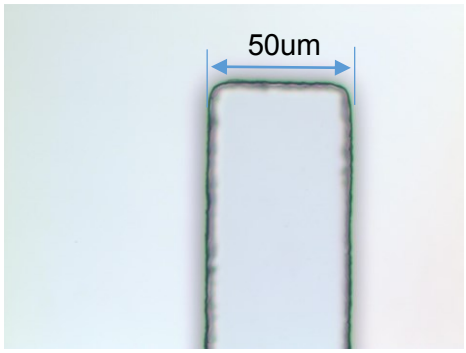

Figure 41: Optical micrograph of a fabricated SU8 waveguide device. Work based on the design of Fig. 40.

4.5 Waveguide Loss Testing

In order to characterize the fabricated optical waveguides a test setup was needed that would allow for launching light into the structure with minimal spill around the outside of the structure influencing the measured light output. To achieve this goal, a test-setup was built with the help of Dr. Muller and his students in the physics department at USF. Using an air-stabilized optics table as a platform a 10 um fiber was positioned directly in front of the 20 um x 50 um waveguide structure. The fiber was free-space coupled to a 450 nm laser on one end while the other end was affixed to a XYZ position stage for precise control of the into a single mode fiber. This allowed the fiber to be positioned directly in front of the waveguide structure to measure the output power avoiding light spillage for coupling into the underlying substrate. The setup is also capable of imaging the end of the waveguide using a camera for beam size and shape measurements, as shown in Figure 42.

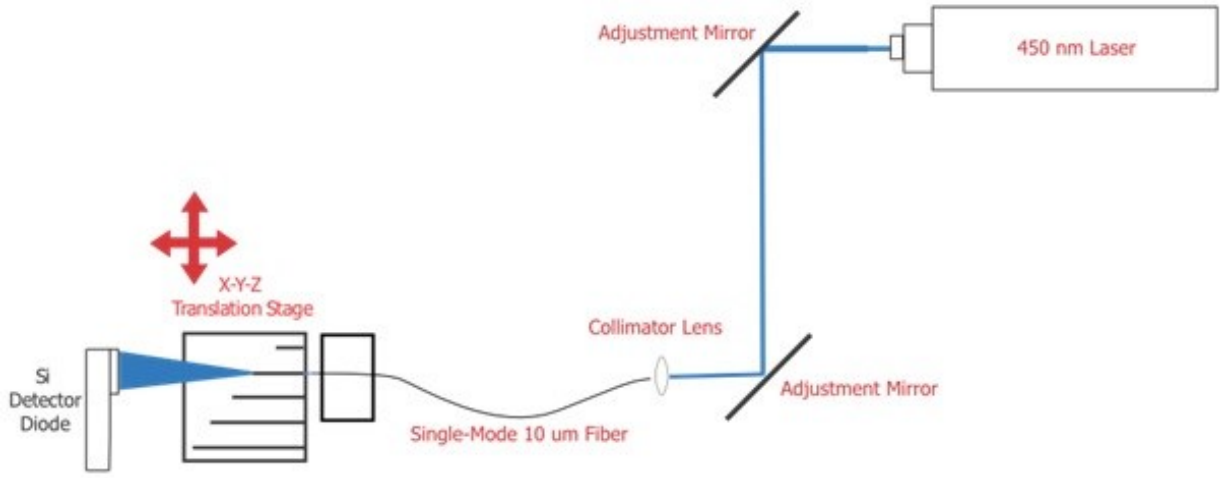

Figure 42: Setup for measuring the insertion loss of waveguide devices. The measurements were performed in Dr. Muller's laboratory in the physics department at USF.

The laser beam was generated via a 450 nm 113 mW free-space laser aligned with two mirrors and launched into a single-mode fiber via a collimator. After collimation, the output power of the fiber was measured to be 3.2 mW. Light emerges from the distal end of the waveguide onto a Si photodetector for waveguide output power measurement. The fiber was aligned for maximum intensity from the waveguide for each measurement.

For measuring loss per unit length the microfabricated 50 um x 20 um x 30 mm structures were cut into various precision lengths ranging from 1 mm to 15 mm using a diamond blade dicing saw. The waveguides were then mounted onto the stage one at a time with double sided adhesive tape. Before each measurement the power output from the optical fiber was measured to ensure proper loss calculation. The results of the test show a loss of -1.04 dB/mm for uncladded waveguides and -3.3 dB/mm and -3.9 dB/mm for those cladded in SiO2 and SiO_2/*a*-SiC respectively. The coupling loss is found from the y intercept and is estimated at ≈-1 dB for uncladded (air cladded) waveguides and ≈-3.2 dB to -3.9 dB for the cladded stacks.

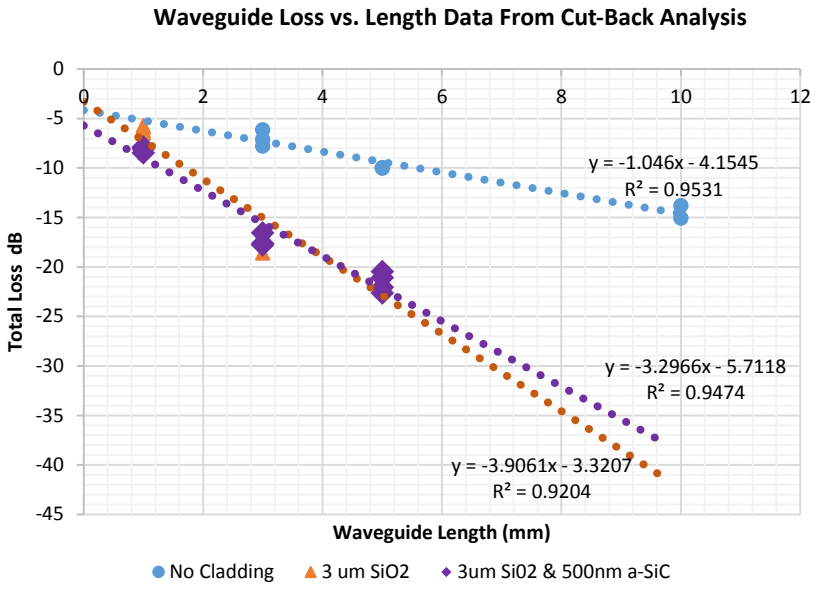

Figure 43: Optical loss (dB) per mm of waveguide structures. Optical loss was measured in dB per mm from the polymer optical waveguides fabricated on 3C-SiC substrates. Also shown are the linear fit models for each material stack type which indicate a relatively good linear-fit to the data.

The loss per unit length reported here is very similar to those SU-8 waveguides reported in the literature for a similar sized structure. For example, Maesoon *at al*. from the University of Michigan reports using 15 um square SU-8 waveguides for optogenetics with a total loss of 22.04 dB over a path length of approximately 5 mm (approximated from figure) [26]. This gives our waveguide similar results and the ability to activate ChR2 through its length.

4.6 Pulsed Optical Source Creation

In order to achieve multi-wavelength optogenetics stimulation a general light pulser setup was created. The setup needed to be cabible of generating 5 ms pulses of both 473nm and 530 nm light for ChR2 and NpHr respectively. The sources needed to be coupled to LED for flexable device development and testing.

To achieve this goal, fiber coupled LED diodes were obtained commercially through Thor Labs (MF470F1,M530F1) and were driven using 300 mA constant current power supplies and controlled using an Atmel ATMega328P microcontroller system. The diodes were fiber coupled

to 200 um core multimode optical fibers and the system was bench marked for both speed and light intensity. The software was set to generate 5 ms light pulses and the fiber output was detected using a silicon photodiode and displayed on an oscilloscope (Figure 44). The emitted optical intensity from the fibers was benchmarked using an optical power meter and silicon photodiode. The 470 nm blue channel provided 73.2 mW/mm^2 and the 530 nm channel provided 35 mW/mm^2. The system's output intensity can be adjusted in 255 discrete steps down to zero using the microcontroller software. This capability may be useful later when the system is coupled to waveguides with high inherent loss characteristics or multiple concurrent stimulation channels. Overall, it was determined that this system would provide both the temporal precision and light intensity required for optogenetic stimulation. This will provide a controller test bed when exploring other optical hardware.

Figure 44: Generated 5 ms optical pulses. Oscilloscope data showing 5 ms optical pulses detected from the 473 nm fiber output of the system. An amplified Si photodiode was used in conjunction with an oscilloscope to display the pulse timing. Each pulse displayed 73.2 mW of average power.

4.7 Optrode Design Overview

The outside device design was modeled after a 5 mm probe geometry similar to that used by NeuroNexus (probe model A1x16-5mm-100-177-A16). This outer geometry was chosen so that, in future work, the probe could be directly compared to standard Si probes for chronic implantation studies. A 60 um waveguide width was chosen to provide sufficient optical coupling to the source in coupling and activation while the 20 um height was to provide for ease of fabrication on subsequent mask alignment steps.

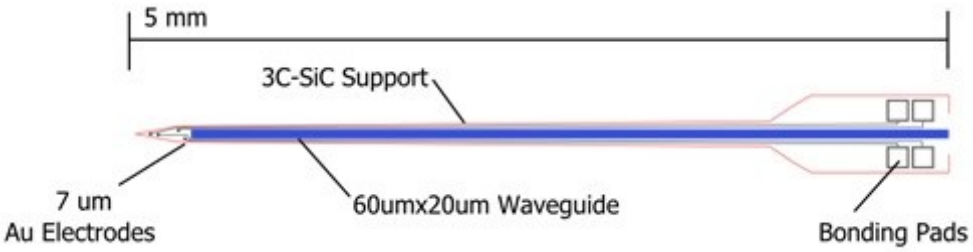

Figure 45: Overview of the adopted SiC optrode design.

The lithography mask layout was created in Autocad 2012 for later conversion to the GDSII filetype used in mask making. The mask was designed as a single 12 mm die with multiple interlocked shanks (Figure 46). This was done to allow for an outer framework the process have better adhesion to the carrier wafer used in crucial ICP etching steps and the utilization of step-and-repeat mask making to be used. Later, in packaging, the shanks will be removed by using precision vacuum tweezers. Each shank was designed to be broken at the designed snap point near its base as per the excellent suggestion of Dr. C. Frewin in our group.

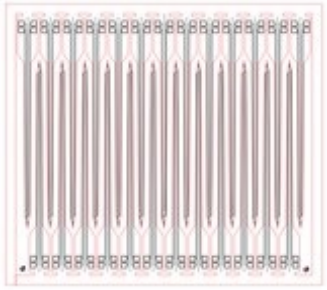

Figure 46: Mask layout of a single die of the optrode system.

4.8 Fabrication Process

The processing of the SiC-based implant device is heavily dependent on Inductively coupled plasma (ICP) etching used in multiple steps each requiring precise timing of etch parameters. Four masks are used in the total process, one for each lithographic step. The most difficult part of the process is the final release of the probes from the substrate wafer as the probe's substrate thickness is on the order of 10 um. Over etching the wafer's backside and etching through the device can happen in a misjudgment of just a few seconds just to illustrate this point.

The process is outlined in detail in Figure 47. The devices begin with an epitaxial 3C-SiC film grown by chemical vapor deposition (CVD). On top of this SiC film, 3 um of PECVD SiO_2 is deposited to act as both a lower cladding layer for the waveguide and also electrical insulation from the underlying substrate. This is followed by a metallization stack of 200 Å of Ti and 2000 Å of Au for the electrical conductors that is patterned using photoresist and etched using Au etchant. This completes the electrodes definition. Next, in another PECVD deposition, .40 nm of SiO_2 is used as an adhesion layer for a layer of amorphous SiC (*a*-SiC) which completely covers the metal contact layers. This metal layer is then patterned using photoresist-based lithography and ICP etching to reveal windows in the insulation for micro-electrodes and pads for wire bonding. ICP etching is used because, like single crystal SiC, *a*-SiC has very slow etch rates so the material is removed with high intensity RF bias (>1500W). Next, using lithography, 20 um x 60 um multimode optical waveguides are patterned using SU-8 polymer on top and adjacent to any electrodes. This completes the functional components of the device. The following steps are used to release the fabricated probes from the underlying substrate through wafer bonding and wafer thinning using ICP plasma.

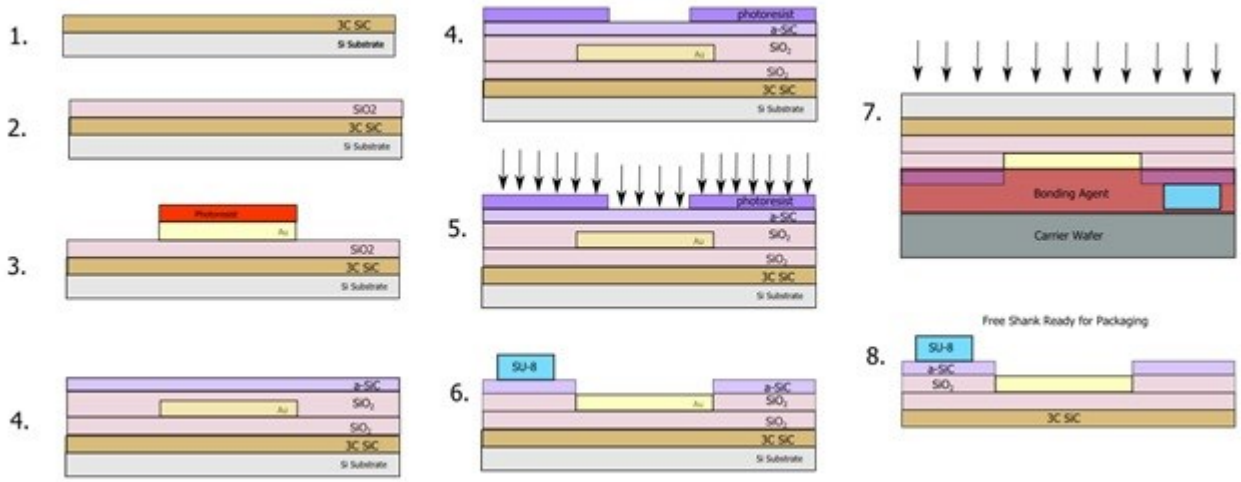

Figure 47: Process flow for creating SiC based neural probes. Process flow for creating SiC based neural probes with active electrodes and waveguide structures. Steps 1. through 8. described in detail in the text.

Devices were etched using this process and fabricated to step 7 Figure 47. The resulting device is shown in Figure 48 unreleased from the underlying Si substrate. Although nearly finished, the last release step(s) 7-8 were not achieved in the time of writing this document and are left as future work for the team.

The technical difficulty with fabricating on highly stressed 3C SiC was evident as several wafers were developed to this point and subsequently destroyed by the subsequent flip and bond process (step 7). In general, the final device film is 6 um in thickness and requires very precise etch timing to avoid etching into the device itself. In addition, any gas bubbles trapped during the flip and bond step cause allows the plasma to wrap around the device and etch the backside. Once this occurs the device is destroyed. Although precise timing was used in conjunction with a precise thickness of photoresist for the probe masking layer etching was a re-occurring problem. This is a common problem to the material and will need to be resolved before mass commercialization of such a device.

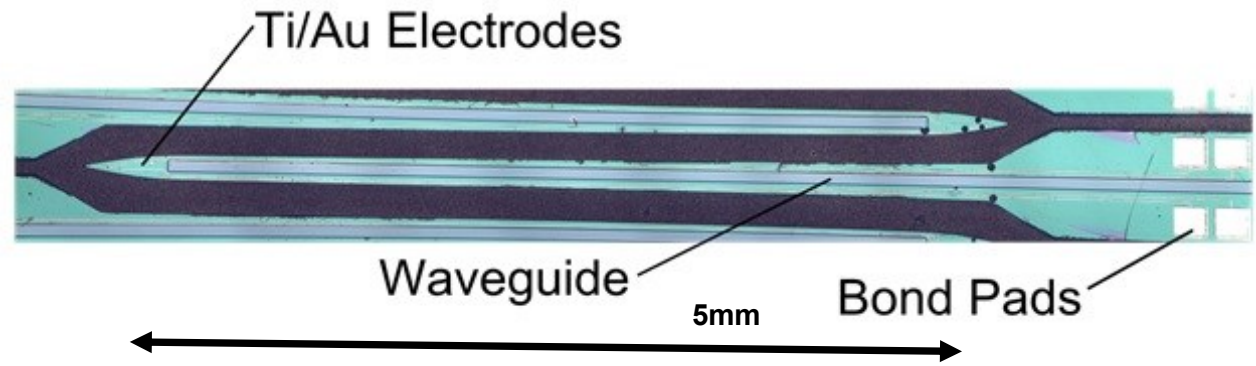

Figure 48: Optical micrograph of a SiC neural implant. SiC neural implant composed of 13 optical microscope images compiled into one photograph. Electrodes on the implant and the central SU-8 waveguide are visible in the photo. The rough blackish material is the underlying handle wafer which had yet to be removed at the time this photograph was taken.

Under high magnification the electrodes on the tip of the device are visible Figure 49. The etched electrode windows appear as white dots overtop the electrode geometry. This was a improvement over the MEA devices in chapter 3. The MEA devices exposed the underlying substrate due to the fact that the windows were larger than the electrode area. By inverting this and creating tightly controlled windows overtop of the metallization we can avoid any unnecessary contact with other less biocompatible materials.

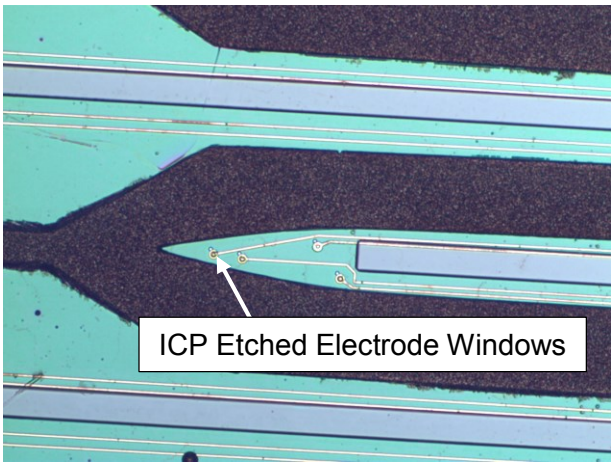

Figure 49: High magnification optical micrograph detailing device electrodes. Four electrodes are visible and the exposed electrode diameter is 10 um for each location.

4.9 Packaging

Devices that are this fragile and small require proper packaging for handling, implantation, and connection to peripheral bio potential amplifiers. Using Cadsoft Eagle 3.6 a carrier board was designed with integrated bond pads, traces, and dual-in line package (DIP) style breakout connector. The carrier was designed to be epoxy-bonded to the finished probe and then wire bonded to the integrated bond pads on the implant. The carrier board was designed with gold plated contacts to facilitate good electrical connection when using a thermosonic ball bonder.

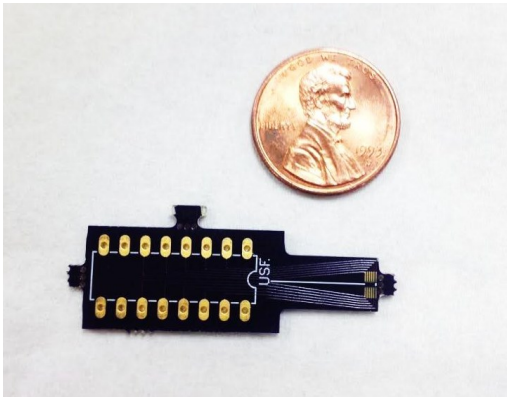

Figure 50: Carrier boards for the SiC based implants

4.10 Conclusion

In this chapter we presented the design for a SiC based optrode based on work done previously from the MEA design and fabrication discussed in chapter 3. We designed and tested SU-8 polymer waveguides for use for optogenetic stimulation that utilized a novel material stack involving SiO_2 and amorphous SiC (*a*-SiC) to improve biocompatibility of the SU-8 polymer material. A microcontroller-driven system for light pulses was built and tested to ensure temporal precision capable of ChR2 activation. In addition, a SiC based, metal (Au) electrode, optrode implant was designed and fabricated in section 4.7-4.9 using MEMS processing techniques. Work and testing on the optrode is still ongoing using improved SiC processing techniques developed based on lessons learned from this work.

CHAPTER 5: SIC PHOTOCAPACITANCE FOR BIOSENSORS

5.1 Overview of the SiC Photocapacitor Device

Photosensitive capacitors (PSCs) are one means to provide continuously variable reactive tuning in RF circuitry. In addition they enable capacitive-optical sensing applications to be realized. Unlike varactors, PSCs often do not require a DC bias voltage to operate. This is a major system advantage when interfacing directly to RF elements or implementing passively monitored optical systems. Instead of using conductive wires or traces as control elements, optical fibers or free-space lasers can be used for affecting the desired capacitance change. In the case of a tunable antenna, this results in little to no perturbation in the surrounding EM field. Also, by using durable, high-κ, high-temperature, very high breakdown voltage, V_{bd}, semiconductors such as 4H-SiC, we can greatly expand present day RF circuit capabilities into high power designs. Possible applications of the PSC effect include reactive tuning of antennas, phase delay devices, radiation detection, and chemical/biological florescence sensing.

We present experimental findings regarding the photocapacitance effect of Schottky barriers fabricated on bulk 8° off-axis high purity semi-insulating (HPSI) 4H-SiC. We have fabricated several 1cm x 1cm square photocapacitor devices from bulk material using metal-evaporated Ti/Au contacts using a simple planar parallel-gap geometry. IV curves were taken of the devices using an HP-4145B semiconductor parameter analyzer to verify Schottky behavior as a function of DC bias. The devices were then studied for series capacitance (Cs) and series resistance (Rs) characteristics using an HP-4284A LCR meter operating at up to 1 MHz and under illumination of below-bandgap 470 nm and 590 nm high intensity LED light sources (Thor Labs models M470 and M590).

The resulting data demonstrated an increase in Cs and a drop in Rs with increasing optical intensity incident on the device. This is very reminiscent of the same effect seen in HPSI Gallium Arsenide (GaAs) [66][67]. Series capacitance and resistance data points were taken in a range of light intensities from the dark condition to the peak power for each LED in 255 discrete steps. The diodes were positioned 3 cm above the sample for equivalent and uniformly distributed optical spot sizes. Shifts in both Cs and Rs were repeatable with either wavelength with the largest capacitance changes seen at low frequency (33 kHz). At this frequency while using 470 nm light, Cs increased from its nominal value of 186.7 pF to 575.6 pF while Rs dropped from 150.0 kΩ to 22.4 kΩ. This demonstrates the existence of the photocapacitance effect in HPSI 4H-SiC and thus warrants further investigation. The underlying phenomenon of the effect is suspected to be the light's interaction with the dominant deep level traps through the Shockley–Read–Hall (SRH) recombination mechanism.

5.2 G-G Model

In this experiment, we explore the use of HPSI 4H-SIC as a photosensitive capacitor exploiting its efficient SRH recombination center for high-sensitivity to below-band tuning using illumination at 473 nm. The experiment is based on the work of a similar photocapacitance effect measured in SI GaAs [66]. The effect will follow a modified model to that proposed by Goswami and Goswami (G-G)[68] and then modified by Sakr and Boulais to accommodate Shottky contacts (Figure 51).

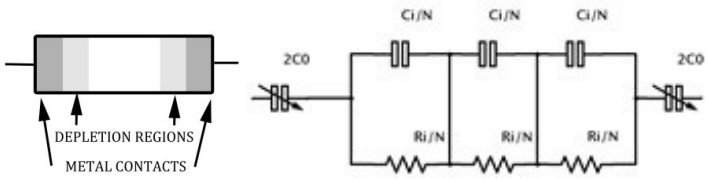

Figure 51: Photocapacitor model based on the G-G model [68]. Left device sketch showing the depletion regions in the semiconductor and right the equivalent circuit schematic. The RC lumped circuit elements in the center of the model are for variations of the material due to absorption as the light passes through the bulk. The capacitors on either side represent the junctions of the device.

The given model has two depletion junction capacitances due to each of the metal Schottky contacts in series with several internal RC lumped circuit elements approximating the varying light Φ(hv) intensity as light penetrates through the thickness of the semiconductor. Qualitatively, the system capacitance follows Eq.4.0 where R is the resistance of the device, ω is the frequency in radians, and C_∞ is the structures capacitance at high frequency. [68]

$$C = C_\infty + \frac{1}{\omega^2 R^2 C_\infty} \tag{5.0}$$

Therefore, by the G-G model the capacitance of the structure increases with light intensity due to the reduction in R and can be described as a byproduct of the photoconductivity caused by the optical generation of charge carriers in the semiconductor bulk.

The total capacitance of the device will heavily depend on the polarizability of the dielectric. Sources of polarizability within the crystal depend on ionic α_i , electronic α_e, dipolar α_e, space-charge α_{int} and a term for the addition of charge carriers during illumination α_{ph}, Using this idea we now adapt Sakr's proof of polarization dependent capacitance for our device. In a dark condition the polarization is given as:

$$\alpha_d = \alpha_{dip} + \alpha_e + \alpha_i + \alpha_{int} \tag{5.1}$$

During illumination the α_{ph} term is added to accommodate the added charge carriers as follows:

$$\alpha_T = \alpha_{dip} + \alpha_e + \alpha_i + \alpha_{int} + \alpha_{ph} \tag{5.2}$$

The Clausius–Mosotti relation gives the relationship between the carrier concentration, polarizabilty of the molecules, and the relative dielectric constant:

$$\frac{\varepsilon_d - 1}{\varepsilon_d + 2} = \frac{N_d \alpha_d}{3\varepsilon_0} \tag{5.3}$$

where ε_d (the relative permittivity) can be written as:

$$\varepsilon_d = \frac{3\varepsilon_0 + 2N_d\alpha_d}{3\varepsilon_0 - 2N_d\alpha_d} \tag{5.4}$$

Under photon flux Φ(hv) the permittivity becomes

$$\varepsilon_{ph} = \frac{3\varepsilon_0 + 2N\alpha_T}{3\varepsilon_0 - 2N\alpha_T} \tag{5.5}$$

where $N\alpha_T$ is:

$$N\alpha_T = N_d\alpha_d[1 + \log(1 + kL)] \tag{5.6}$$

where *k* is a photocapacitance factor and *L* is the light intensity. The relationship between dielectric constant change and capacitance is

$$\frac{C_{ph}}{C_d} = \left(\frac{\varepsilon_{ph}}{\varepsilon_d}\right)^n \tag{5.7}$$

where "n" is a term related to dielectric morphology, C_{ph} is the illuminated capacitance and C_d is the dark capacitance. Combining the previous information, the ratio of capacitance under illumination to the dielectric (i.e., dark state) capacitance becomes:

$$\frac{C_{ph}}{C_d} = \left(\left(\frac{3\epsilon_0 + 2N_d\alpha_d[1+\log(1+kL)]}{3\varepsilon_0 + 2N_d\alpha_d}\right)^n\right) \tag{5.8}$$

Essentially, this model states that the change in capacitance that the device exhibits will be linearly related to the light intensity for low values of intensity. The model isn't to be taken as a direct numerical simulation, but more as a guideline showing the relationship, as it depends on constants that are best experimentally determined. According to Sakr, with increasing intensity the influx of minority charge carriers produced will taper off and the capacitance will follow an asymptotic relationship leveling off at a specific value. Also, the carriers will have an ultimate polarization "velocity" that will limit the frequency that the photocapacitor can operate (i.e., less capacitance "shift" at higher frequencies).

5.3 Theory/Calculations

Semi-insulating silicon carbide has very low radiative and Auger recombination coefficients and is therefore dominated by SRH (Shockley Read Hall) recombination and surface effects within the material [69][70]. Deep level transient spectroscopy (DLTS) spectra of HPSI 4H-

SiC samples reveal two fundamental deep level electron traps with DLTS designations Z_1/Z_2 (Ec-0.65 eV) and EH_6/EH_7 (Ec-1.65eV) [71], [72] (Figure 52).

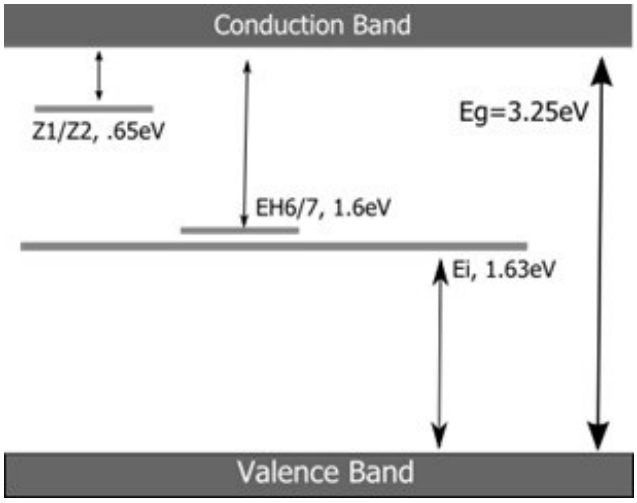

Figure 52. Summary of major recombination centers within 4H-SiC. [71,72]

The Z_1/Z_2 center is still of unknown origin but is known to be an efficient recombination center and is often cited as the dominant defect level limiting the carrier lifetime in this material [71]. Work in electron paramagnetic resonance (EPR)/DLTS has suggested that the double defect arises from a silicon antisite - silicon vacancy complex [73]. As such, the Z_1/Z_2 trap center is a combination defect and has equal cross sections for electrons and holes ($10^{-14}cm^2$) making it an efficient recombination center [73].

In addition to the centers listed Figure 52, 4H-SiC often has several other shallow-level defect centers from both Al, B (p-type dopants) and N (n-type) impurities. These shallow traps decrease the carrier lifetime for SRH recombination but are not a major factor in the bulk material's resistivity due to equal concentrations near 10^{15} cm^{-3}. It is also worth noting that these shallow traps can be greatly reduced by high-temperature annealing thereby making SRH recombination more effective [69]. In our experiment, we focused on using low intensity below-bandgap illumination to exploit the SRH recombination effect within the material's recombination centers thereby demonstrating a novel, optically tunable, SiC photocapacitive device. Such a device has

wide ranging uses suitable for applications such as high-power or ruggedized RF applications, rugged fluorescence sensing, or radiation detection.

The experiment reported here was based on work on a similar photocapacitance effect measured in SI GaAs based on the EL_2 defect [74],[66]. The effect is described in detail by Boulais who proposed three possible mechanisms: 1) Photon bombardment causing the semi-insulating state of the material to gradually become more conductive as the incident power density is increased, 2) an increasing depletion capacitance that increases with optical power density and, 3) the surface Fermi level is modified due to the change in surface states upon photon bombardment [66], [67]. In general, these effects should not be exclusive to SI GaAs so that HPSI 4H-SiC should behave in a similar way based on the same mechanisms, albeit at different optical wavelengths to the change in semiconductor bandgap energy. Due to a larger bandgap in 4H-SiC it may be possible to achieve a greater tuning range over GaAs thus further motivating our experiments.

In GaAs the EL_2 defect is located near midgap so that, upon illumination, transition of electrons to both bands occurs upon direct light illumination [74]. If the Z_1/Z_2 defect is indeed the main defect driving the capacitance change in 4H-SiC then it is likely that much of the trap kinetics happen between the trap and the conduction band due to its position in the band gap (E_c -0.6 eV). It is assumed that the deep-level trap's optical cross section will rise abruptly for any energy equal to that of the trap's depth and then decrease again for energies greater than the depth. The Z_1/Z_2 depth corresponds to a long wavelength of 2066 nm and 4H-SiC has a total bandgap of 3.25 eV [75]. Therefore, to stay within the SRH tunable spectrum, the wavelength chosen for tuning needs to be larger than this to avoid direct recombination. Readily available LED light sources at 473 nm and 590 nm were used to show SRH based capacitance tuning. It is known that the wavelength of these sources chosen is not ideal but with further experimentation we will be able to better hone in on the best wavelength(s) for our tuning experiments.

5.4 Device Fabrication Details

The experiment presented was designed to validate the existence of the photocapacitance effect in 4H-SiC and show its possible use in a device role. The test was done at low light intensity <50 mW/cm^2 and signal frequencies ≤ 1 MHz. Low light intensities were a requirement to differentiate any heating effects from those related to the photoionization of deep-level traps. A simple planar capacitor geometry was chosen to expedite fabrication. The planar photocapacitor devices were made from commercially obtained off-axis HPSI 4H-SiC substrates grown 8° of the basal (001 plane). Resistivity of the 4H-SiC substrate is given from the manufacturer as ρ ≥ 1E5 Ω-cm and a thickness of 400 μm (Fig.2). The devices were fabricated with a 1cm^2 footprint with a central 1 mm gap. This device topology allowed for standard CMOS lithography and metal etching to create the Schottky contacts.

To fabricate the device the following steps were taken: The samples were cleaned using a standard RCA cleaning process to remove organic and metal contamination from the surface. Next, metal was deposited on the topside of the substrate using electron beam deposition. The resulting metallization stack consisted of a 230 Å thick Ti adhesion layer followed by a 2600 Å Au topside contact. Then, the metallization layers were patterned using standard UV photolithography with AZ4620 photoresist. Finally, the metal contacts were etched using a combination of HF and TFA Au etchant to form the capacitor gap shown in Figure 53.

A custom acetate mask was used for the lithography. The mask was used to expose the photoresist during a 13 second exposure in the mask aligner. Once the pattern was developed a chemical wet-etch was performed using MicroChem Gold etchant to remove the unwanted gold followed by a final 2 minute rinse in 50:1 HF to remove the remaining Ti under layer. The resulting contacts consisted of a 230 Å thick titanium adhesion layer followed by a 2600 Å gold contact (see Figure 53).

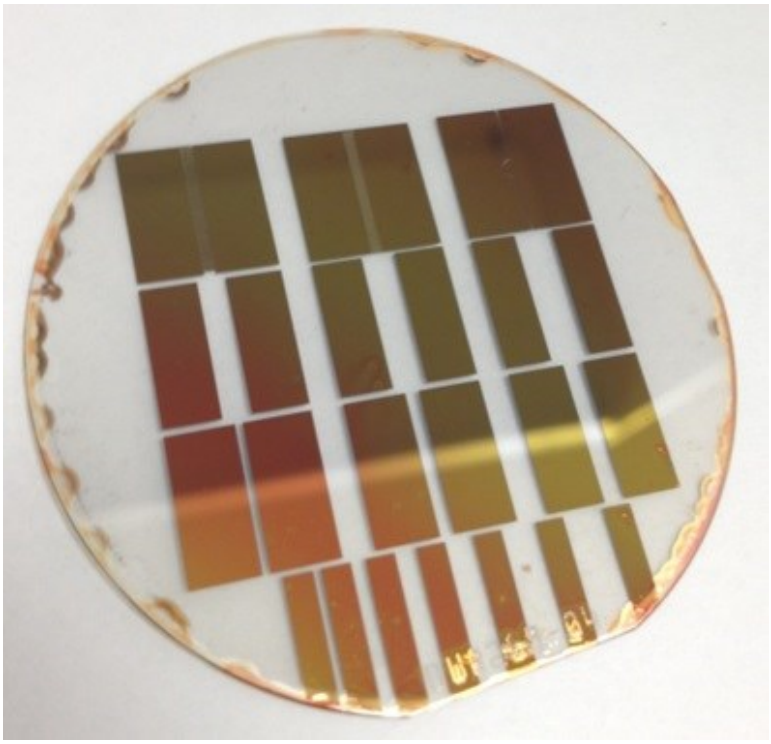

Figure 53: Photo of processed PSC devices. Processed 2” wafer after lithography and etching and before dicing. Substrate is 600 um HPSI 4H-SiC (0001).

5.5 Device Characterization

The LED sources for the experiment were excited using constant-current mode pulse-width modulation (PWM) at 214 Hz which corresponds to a total mark space time of 4.7 mS (Figure 54). The LED light source’s pulse width was set by a digital 8-bit word in the current source’s microcontroller software. Each discrete step (0-255) corresponds to an increase of 18 uS in width and increases with time until the pulse fills the entire period at 100% duty cycle (digital value 255).

This allows for discretely variable average optical power to be delivered to the sample. The LED sources were affixed over the sample at a distance of 3 cm so that the spot size completely covered the device’s central gap.

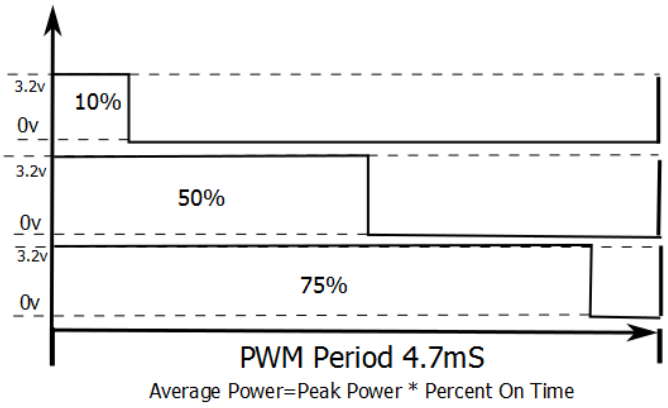

Figure 54: PWM timing diagram. Diagram demonstrates how variable pulse width affects average power.

The corresponding electrical measurements were taken using an HP-4284A LCR meter configured in two-terminal mode with the HP and HC terminals tied to one pad of the device and the LP and LC terminals tied to the adjacent pad (). Effort was taken to reduce the cable length in an attempt to minimize stray capacitance.

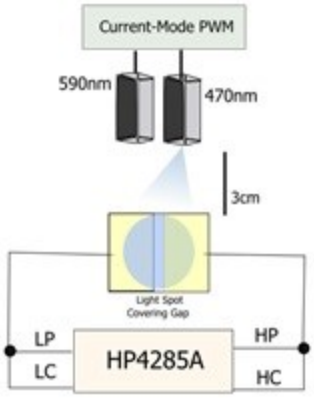

Figure 55: Experimental setup showing the HP-4285A LCR meter. LEDs, and photocapacitor in the configuration used for the experiment.

5.5.1 Schottky Contact Verification

The contacts for the devices were not annealed in order to realize Schottky contacts. To confirm Schottky behavior IV curves were taken using a HP-4145B semiconductor parameter

analyzer thus providing a greater level of confidence in the data and providing a sound starting point for developing a model of the photocapacitive effect.

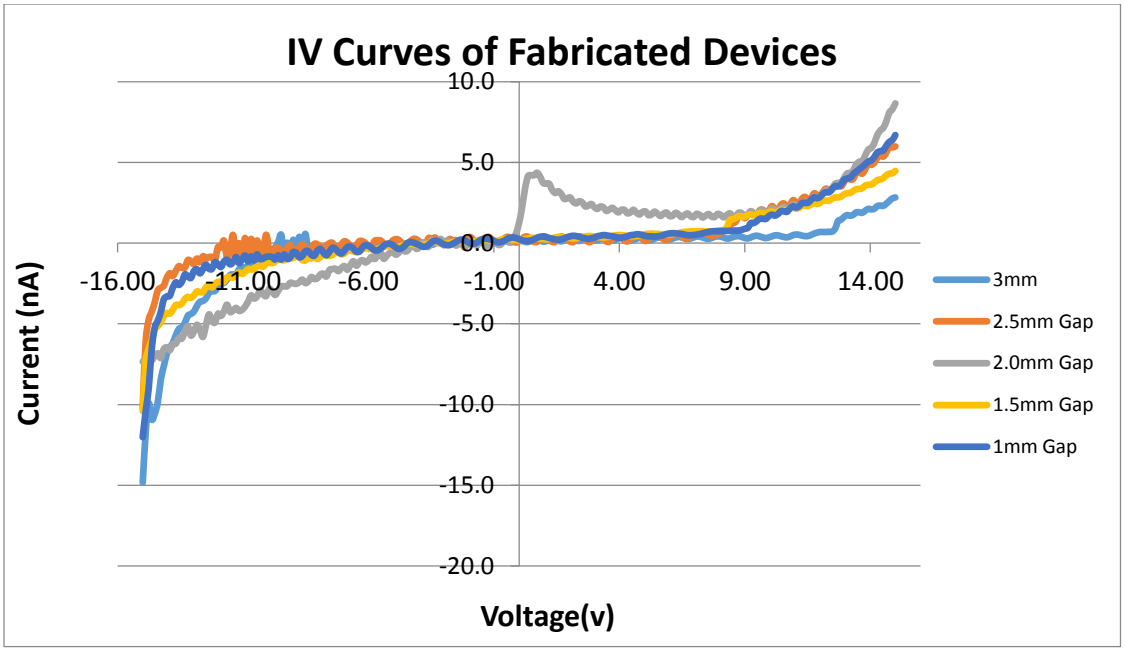

Figure 56: IV curves of 5 fabricated photocapacitor devices. Curves demonstrate Schottky-like response. Various gap geometries from the wafer were used in the test all-resulting in similar Schottky behavior as expected for SiC. The anomaly (negative resistance) on the 2 mm Gap series may be accounted for from surface charging during the test.

5.5.2 Below Bandgap Investigation

The first measurement was a comparison of 470 nm and 590 nm light taken on the same device without DC bias at 1 MHz with a 100 mV signal level. The peak power of the two LEDs differ so average power was used for the comparison. The 470 nm source is 10.1 mW and the 590 nm source has a peak power of 3.2 mW as given by the data sheet and verified using a handheld optical power meter. The C_s and R_s data was plotted against the average power of the LED sources obtained by varying the LEDs pulse width from 18 uS to 4.7 ms and the average power calculated as follows:

$$P_{avg} = \frac{current\ pulse\ width}{total\ mark\ space\ time} \times Peak\ Power \tag{5.9}$$

Also, to aid in the interpretation of the data, trend lines were added to infer how the device may respond at higher power levels of 590 nm illumination to make up for the difference in peak

power of the 590 nm LED. The inflection anomaly visible in the figure at low power levels for Rs is due to measuring the real part of the series impedance Rs. This could be resolved through determining the complex impedance.

An identical anomaly to that shown in Figure 60 was seen in parallel work done using GaAs for a similar photocapacitor device [66]. Curve fitting for the 590 nm data was done with an exponential model for Rs (eq 1.1) and a second order approximation for Cs (eq 1.2). These models led to the lowest possible R^2 squared value.

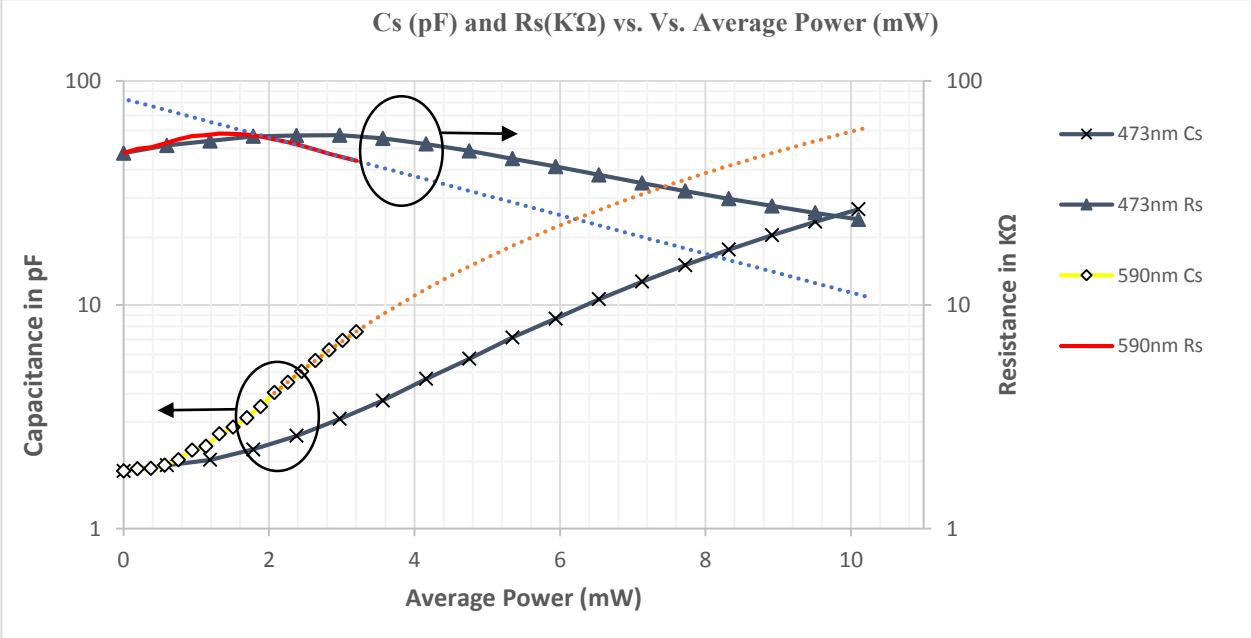

Figure 57: Measured values of Cs and Rs vs. average power for each diode. Average power calculated using eq. 1.0. Curve trend lines for CS are for a second order polynomial and Rs as an exponential with respective R^2 values. This may provide some insight into further modeling parameters.

$$C_s = 0.5611x^2 + 0.2002x + 1.2139, R^2 = 0.9995 \quad (5.10)$$

$$R_s = 83.21e^{-0.199x}, R^2 = 0.9989 \quad (5.11)$$

The photocapacitor device was then tested at three discrete signal frequencies using only 470 nm illumination to determine the frequency dependence of the effect and its corresponding sensitivity. It was evident from the data that the lower frequencies (66 kHz and 33 kHz) provided a much greater shift in capacitance. However, it is not clear if this shift scales linearly with

frequency. It is also important to note that this capacitance shift occurred at extremely low optical power levels (~mW) and, therefore, more power may be required to achieve a resonable ΔC shift at high frequencies.

At a frequency of 33 kHz the photocapacitor device demonstrated a sensitivity of 40.7 pF per mW/cm^2 of excitation power density of 10.1 mW at 470 nm illumination. For a frequency of 1 MHz this sensitivity dropped to 8.27 pF per mW/cm^2.

Other work on photocapacitance in semi-insulating semiconductors has led to proposed 1-D models by several authors [66], [68], [76]. These assume a solid piece of material with electrodes on either side of the crystal and no external fringing fields. It is theorized that the effect will nearly always follow closely to a model proposed by Goswami and Goswami (G-G) that uses series combinations of parallel R and C elements [68]. The same model was later modified by Sakr [76] and Boulais [66] to accommodate Schottky contacts and variable capacitances within the bulk material. Although these models work for general approximations it may be possible that, due to inter-trap dynamics, and the real problem existing in a 3D geometry, an exact solution may be difficult to develop.

More generally, it has been proposed by Boulais *et al.* that, in the case of SI GaAs, the photocapacitance effect is caused by an increase in electrons and holes in the material brought about by photodoping. It was shown that in GaAs the net trap ionization decreases with increasing light intensity [66]. This, in-turn, affects the electric field within the substrate and gives rise to a decrease in depletion width. GaAs has an EL_2 state near the Fermi level that is believed to be the prime center responsible for the effect. HPSI 4H-SiC has similar deep level traps, mainly the $EH_6/_7$ near midgap and the $Z_{1/2}$ slightly above midgap Figure 52, causing a similar photocapacitance phenomenon.

A general understanding of the response comes from the changing depletion capacitance. Qualitatively, the system capacitance follows Eq. 1.3 from [68] where R is the resistance of the

device, ω is the frequency in radians per second, and C_∞ is the structure's capacitance at high frequency.

$$C = C_\infty + \frac{1}{\omega^2 R^2 C_\infty} \tag{5.12}$$

Therefore, by the G-G model, the capacitance of the structure increases with light intensity due to the reduction in R and can be described as a byproduct of the photoconductivity caused by the optical generation of charge carriers in the semiconductor bulk.

5.5.3 HFSS Antenna Simulation

To demonstrate the utility of the fabricated PSC device we performed a RF simulation on a reactively tunable Frequency Selectable Surface FSS using Ansoft HFSS v.14™. In order to best illustrate the powerful effect that a PSC has on a resonant RF structure we decided to perform these simulations on an antenna structure. The antenna unit-cell choice for the simulation was a slot based resonator with a shunt capacitor. Through modifying the structure's resonance with the shunt capacitor we predicted a measureable degree of tuneability to the system.

The antenna's geometry was selected due to its simulation simplicity (less computing time) and the fact that the design lends itself well to high power microwave (HPM) applications (Figure 58). Due to the slot geometry, large broad conductors form the bulk of the structure. This dissipates heat more efficiently than small traces. The FSS simulation here reflects a signal near the X-Band region of the RF spectrum (8-12 Ghz). For the purpose of simulation the entire surface is sitting in free space on top of a 100 um thick SiO_2 substrate with a relative permittivity ε_r of 4. In addition, the metal regions were modeled as perfect electrical conductors (PEC).

Many antenna applications such as FSSs or metamaterials can be simulated as a single resonator structure replicated periodically in a two (or three) dimensional plane (box). We exploit this to perform a simulation on our infinitely-large FSS situated on the *x-y* plane. In the simulation each cell contains a tunable PSC that is a mirror image of all the others. In this was we achieve tuneability of the whole array as we sweep through capacitance values.

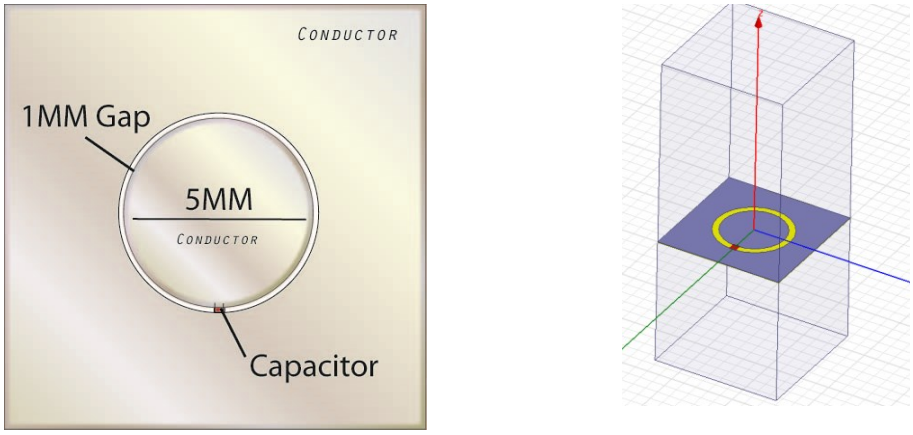

Figure 58: Single tunable cell for X-band simulation. Left dimensions of a single cell of the antenna, Right the cell construction within the HFSS software.

This type of numerical simulation requires two major components 1) periodic boundary conditions for each unit cell and 2) Simulated ports for launching and absorbing uniform plane waves. If the simulated array is sufficiently large it can be modeled using wrap around (periodic) boundary conditions as we have done herein. These boundary conditions come in pairs with one "slaved" to the other for simulating a field phase offset. In our simulation, this is done by forcing a master/slave relationship variable in HFSS (Figure 59).

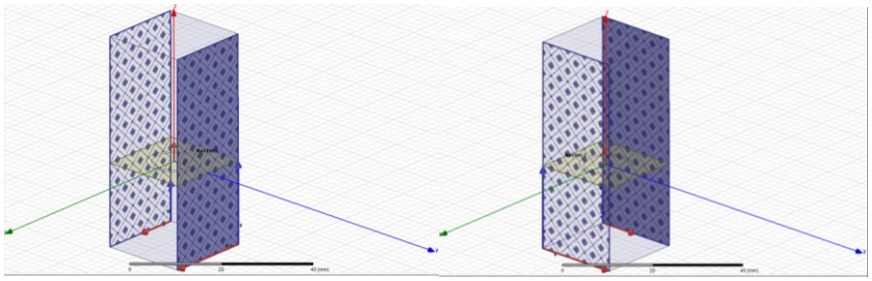

Figure 59: Assigning master and slave periodic boundary conditions. The condition allows for an infinite array of resonators to be simulated. Simulation grid as setup in HFSS.

The phase variable of the boundary conditions provides an angle for the incoming plane wave so that the array can be studied at various angles of illumination. In our preliminary

simulation we only provided for a perpendicular plane wave (Θ = 0° , φ = 0°) but in future studies this variable can be utilized to demonstrate metamaterial effects of the tunable FSSs (such as negative index of refraction).

Working in conjunction with the boundary conditions periodic waveguide ports (i.e., Floquet ports) are used to launch the EM plane wave into the unit cell. Only the lowest Floquet modes (m=n=0) were considered for the simulation. The simulation was run and results were tabulated for each mode-dependent *S* parameter in a matrix.

The simulation resulted in a small degree of predicted frequency tuning of the structure based on the TM mode of the antenna (Figure 61 and Figure 62) The TE mode simulation showed no variation in tuning. This result is to be expected, as only one polarization will result in ***E*** field coupling across the capacitor with the present antenna geometry.

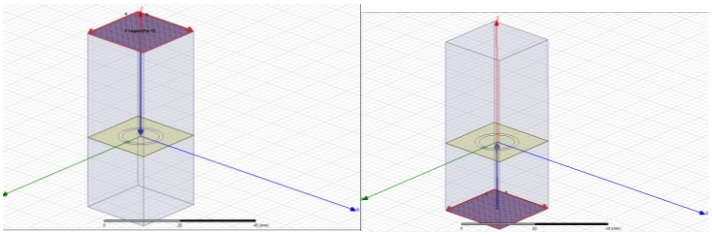

Figure 60: Boundary conditions and ports of the resonator simulation. Floquet ports assigned to the model launch plane waves that propagate perpendicular to the FSS.

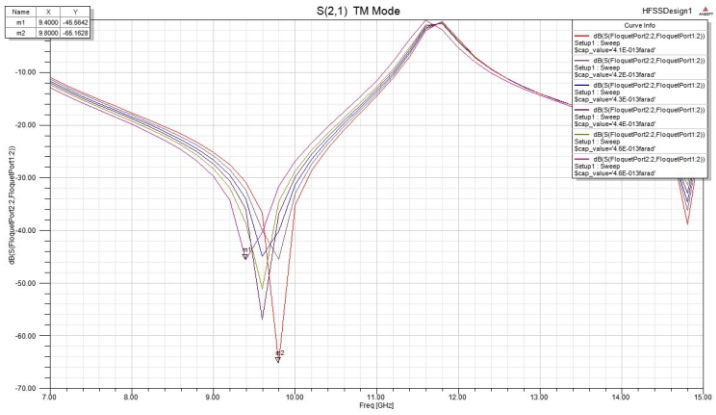

Figure 61: Simulated transmission of the tunable FSS structure. Figure showing ≈300 Mhz of tuneability with a capacitance shift of 50 fF. Each 10 fF of change is plotted as a separate trace above from 410 fF to 460 fF.

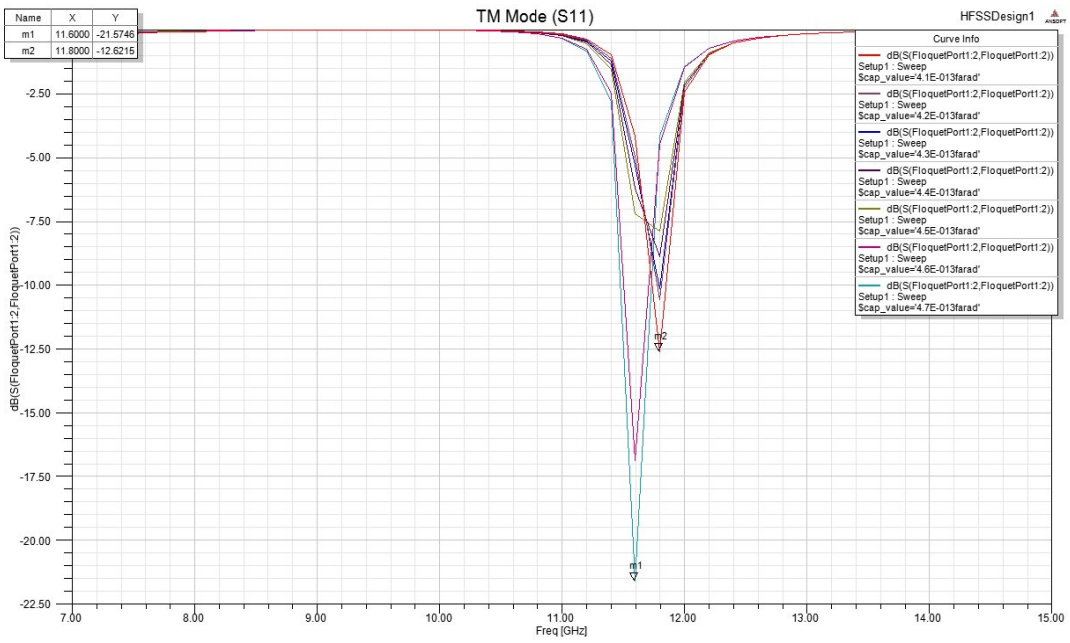

Figure 62: Reflection (S11) of the tunable FSS structure. Also shows 300 Mhz of tuneability with a capacitance shift of 50 fF Each 10 fF change is plotted as a separate trace from 410 fF to 460 fF.

5.5.4 Tuneability of Low Frequency Resonators

In order to explore the optical tuning properties in the RF resonance structure using the 4H-SiC photocapacitance effect two small single-turn magnetic loop (SSTML) antennas were constructed with a resonant frequency of 25 MHz and 150 Mhz, respectively (Figure 63). The SSTMLs are parallel resonant LC tank circuits with the inductance coming from the loop itself. A voltage maximum exists near the top of the loop and a current maximum near the bottom as shown in Figure 63. A discrete capacitor near the top of the loop acts to phase-shift the antenna across its possible resonance frequency. The main loop will inherently have a naturally low radiation resistance of less than 1 Ω so proper matching is required. Near the bottom of the main loop a smaller loop is used to inductively couple the antenna to a 50 Ω transmission line. In this way, the lower loop acts as a loosely coupled ($k \leq 0.5$) air transformer for impedance matching purposes.

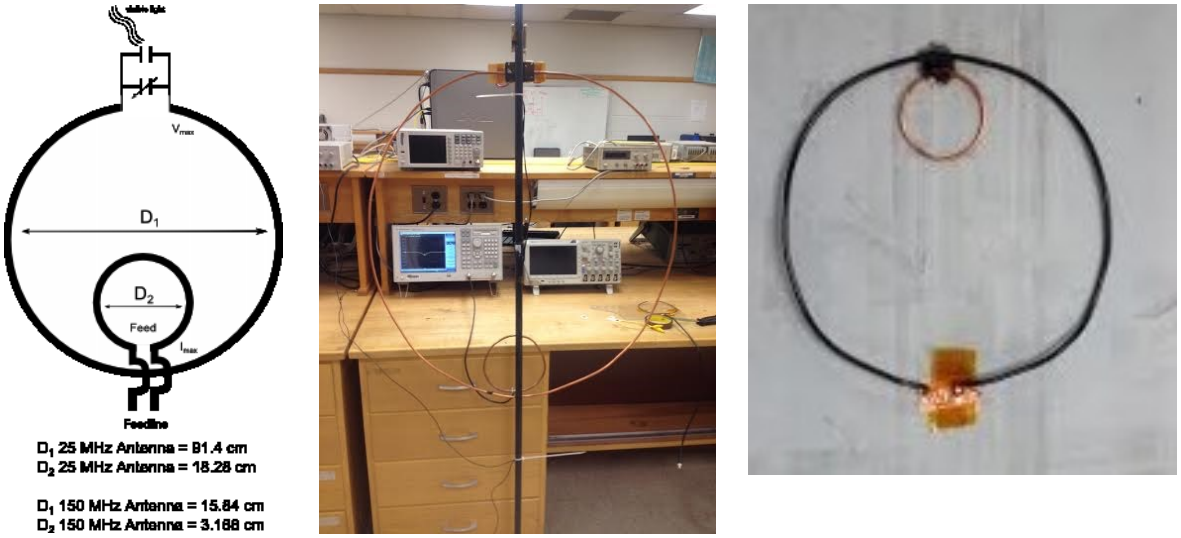

(a) (b) (c)

Figure 63: Antennas used for the optical tuning experiment. (a) Antenna diagram including dimensions (b) photograph of constructed 25 Mhz loop showing the VNA used to measure the RF performance of the antenna and (c) a photograph of the constructed 150 MHz Loop.

For the 25 MHz SSTML the main outer loop was constructed from quarter-inch copper tubing while the inner loop was made from #12 copper wire. At 25 MHz, a full wavelength would result in an 11.99 meter loop circumference. This large dimension of a full wavelength was impractical for testing so a quarter wavelength (2.81 m) was used as the outer circumference of the main loop. The diameter of the inner loop was determined experientially with a ratio of 1 to 5 inner to outer loop diameter which provided the best SWR ratio. The antenna was then mounted vertically on a non-conductive PVC support so that the base of the antenna was elevated 1 m above the ground. An LED was then placed 1 cm from the photocapacitor near the apex of the antenna and was powered by wires connected to a constant-current DC power supply. In addition, a 445 nm 2.6 W diode laser was used to demonstrate the tuning range. In this configuration the laser was colminated into a 5 mm diameter beam and directed onto the center of the 4H-SiC PSC from a distance of 1 m.

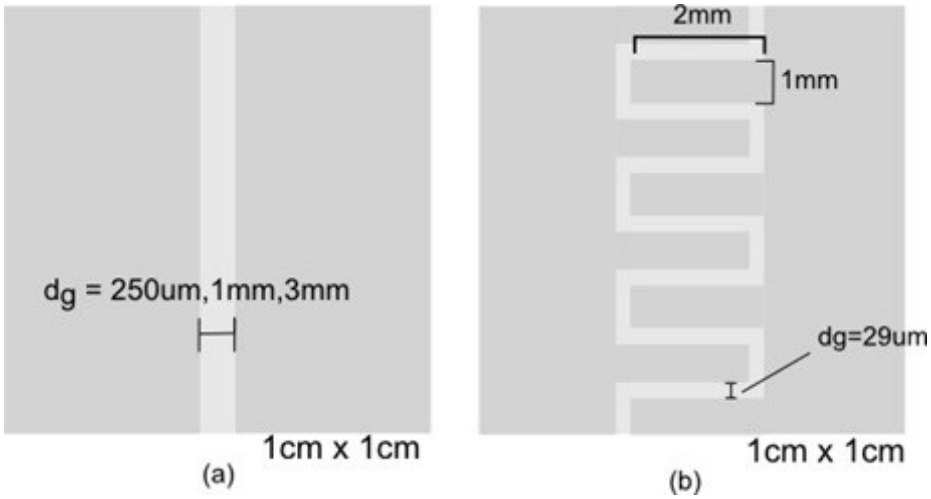

Figure 64: Diagram of PSC microfabricated gap geometries. (a) Simple planar PSC gap design with gap dimensions of 0.25, 1.0 and 3.0 mm and (b) the interdigitated PSC to increase the gap area with an conductor spacing of 29 um.

Four (4) gap geometries were used in the test. Three of the gaps were of the basic linear gap design with the fourth being a dense interdigitated gap capacitor (IDC) used to achieve a greater area (Figure 64). The devices were mounted contact side down and back-illuminated so that the light was not blocked by the PSC conductors. 4H-SiC has very low absorption at these wavelengths so the light is mostly absorbed in the bulk of the device.

5.5.5 RF Tuning Results

In the tests conducted both antennas performed well and showed a resonance shift provided enough below-bandgap illumination intensity was delivered. The 150 MHz loop showed a higher percentage resonance shift with the largest shift at 4.04 % of the resonant frequency but showed an undetectable shift with the lower intensity LEDs Figure 65. The data in Table 4 shows a light/dark comparison at the full 0.203 W intensity of the 470 nm LED and full 2.6 W intensity of the 445 nm diode laser. The laser's central wavelength slightly differs from that of the LED but this is still useful for demonstrating a wide tuning range. The dark condition was established with room light extinguished although it did not make a detectable difference in the observed data as the 4H-SiC PSC, as expected.

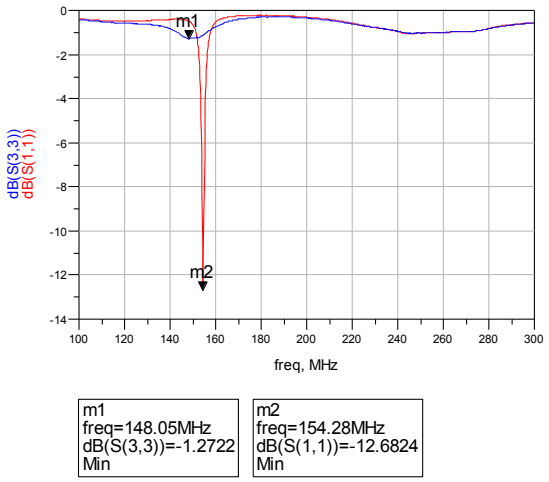

Figure 65: VNA data (S_{11}) showing the resonance point. Antenna in the dark condition (marker m2) and illuminated by a 2.6W 445 nm laser source (marker m1). The greatest shift was 6.23 MHz which was seen in the 250 um IDC gap which is a shift of 4.04% of the resonant frequency.

Comparisons were made with illuminated vs. dark conditions of the device for various gaps with the general trend moving towards the smaller gaps providing a greater resonance shift. The 25 MHz SSTML would not provide a match to the smaller-spaced 29 um IDC device. This is likely due to the low inherent initial Rs value which shorts out the loop.

All of the resonance shifts, however, have an associated loss in coupling efficiency (Figure 65). The largest frequency shift related to the greatest loss in coupling. This is likely due to the rapid drop in R_s seen in the aforementioned LCR tests shorting the loop's V_{max} point.

Table 4: Resonance shift of gap geometries. Each gap geometry and antenna combination for both 473 LED and 450 nm Laser stimulation.

25 MHz Loop	Gap Structure	Percent of Resonance Shift (%) under .2W 470 nm LED	Percent of Resonance Shift (%) 2.6 W 445nm laser
	28 um IDC	.24 %	.86 %
	250 um Gap	0.22 %	1.81 %
	1 mm Gap	0.20 %	1.24 %
	3 mm Gap	0.22 %	.08 %
150 MHz Loop			
	28 um IDC	.09 %	4.04%
	250 um Gap	.13 %	1.18 %
	1 mm Gap	.34 %	0.96 %
	3 mm Gap	.04 %	0.21 %

5.5.6 Circuit Model Development

To gain a better understanding of the SSTML resonator system a simple circuit model was constructed in the Agilent ADS (Advanced Design System) simulation platform. The model of the SSTML was a simple LCR circuit that was loosely coupled to an air-core transformer (Figure 66). The differences in sizes of the inner and outer loop were accounted for by varying the number of turns in the transformer to account for a difference in magnetic flux intersection from each loop. The lumped elements in the model combine several terms into each element. The "R" term in the model accounts for both the Radiation Resistance R_r and the loss resistance from the conductor R_l .Inductance of the loop L accounts for both the loop inductance L_l and the wire inductance L_w.

As a starting point for the simulation, loop inductance, loss resistance, and radiation resistance were calculated using approximation equations specifically for magnetic loop antennas [77].

$$R_r = (3.38E-8)(f^2 * A)^2 \tag{5.13}$$

$$R_l = (9.96E-4)(\sqrt{f})\left(\frac{S}{d}\right) \tag{5.14}$$

$$L = (1.9E-8)S(7.353 * \log\left(\frac{96*S}{\pi*d}\right) - 6.386) \tag{5.15}$$

where A is the loop's area, S is the conductor length, d is the conductor diameter and f is the central operating frequency.

The schematic shown in Figure 66 was then optimized against actual S_{11} data collected from a Vector Network Analyzer (VNA) using the ADS gradient solver algorithm. This resulted in a model with summation of the residuals sum of squares (RSS) function value of < 0.06 (Figure 67). The resulting values for the model in were R_2 = 1.45185 Ω, L_3= 2.87571 μH C_2 = 18.9061 pF, which all seem reasonable for the model chosen.

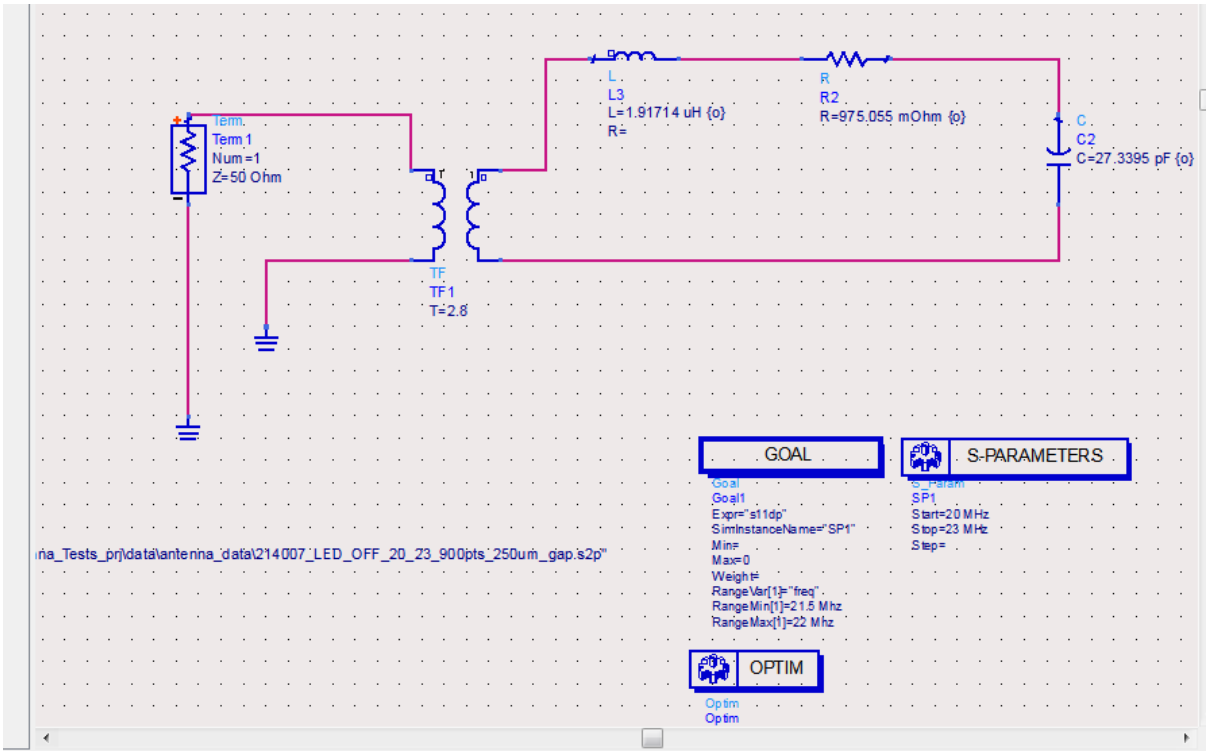

Figure 66: ADS circuit model of the SSTML resonator.

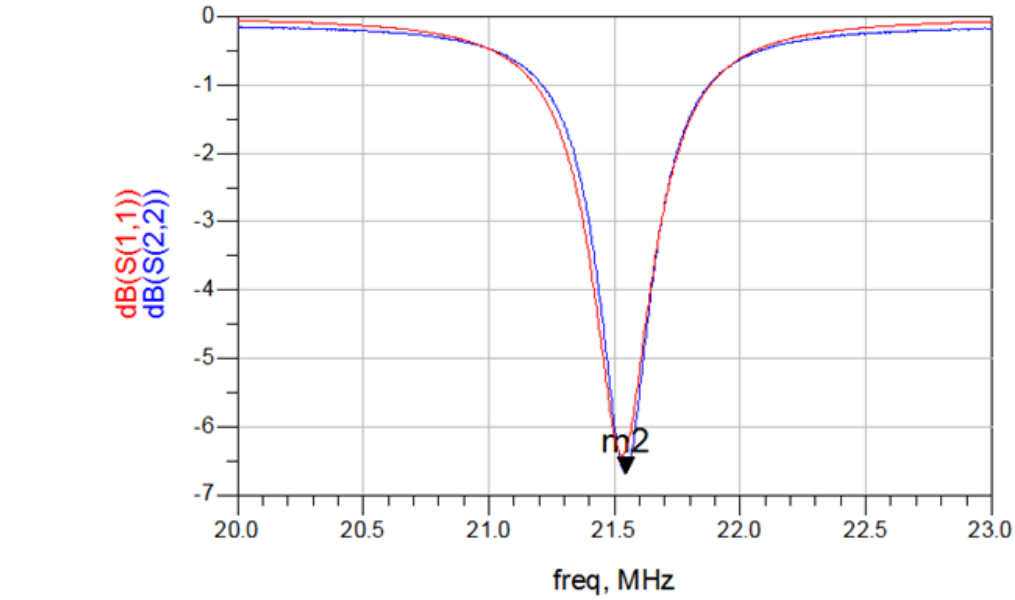

Figure 67: Measured (S11) of the fabricated SSTML. Model (S11)(in red) vs. Measured (S11) in Blue performance of the SSTML. Note the excellent fit of the model with the data. R^2 value of .98

5.5.7 Sensing with PSC Devices

Using 4H-SiC for remote sensing would allow for compact and rugged sensing structures. In the proposed design a photocapacitor and inductor are shown microfabricated directly onto the HPSI 4H-SiC wafer. This structure, used in conjunction with an inductively coupled LED at another frequency, would allow for a totally wireless passive sensing system for bio analyte characterization, UV sensing, or other florescence applications that respond to wavelengths in the sub-bandgap range of 4H-SiC (i.e., E_G < 3.2 eV)(Figure 68). Other work in the literature has established single-crystal SiC as a biocompatible and hemocompatible material [78]. Thus, 4H-SiC would be particularly well suited for use *in vivo*. Magnetic antenna structures are generally preferred as it has been shown that the magnetic field has less loss in the conductive fluid environment of the body [79].

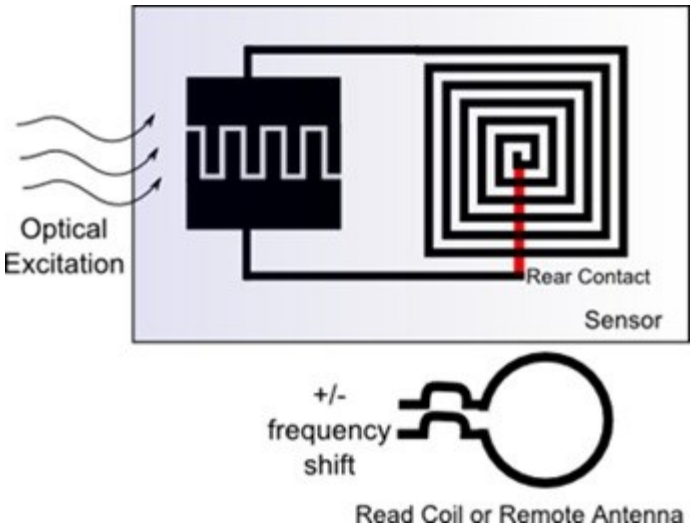

Figure 68: PSC as a possible sensing element. Possible monolithic geometry for using the SiC PSC as a sensing element. A PSC and inductor would be microfabricated directly on 4H-SiC, as shown, and tuned using a laser diode or LED thus allowing for a completely wireless sensor.

5.6 Conclusion

We have successfully demonstrated a multi-wavelength tunable photocapacitor made of HPSI 4H-SiC. We have modeled, measured, and demonstrated an effect that has yet to be reported in the literature. The fabricated devices showed changes in both series capacitance and

series resistance at 470 nm and 590 nm illumination wavelengths. For 470 nm the sensitivity of the device ranged from 40.7 pF per mW/cm^2 at 33 kHz to 8.27pF per mW/cm^2 at 1 MHz. From the data it is apparent that below-bandgap light influences the series capacitance and resistance in a predictable manor suitable for many tuning device and sensing applications. More work will need to be done to determine the frequency limits, as well as the temperature dependence of the technique. In future work the effect will be studied at higher power levels and tunable wavelengths used to optimize the effect to the trap(s) and an exact model will be pursued using Comsol™ to solve Poisson's equation in 1-D for the traps thought responsible for the measured effect reported here.

In addition, we have demonstrated ~ 6 MHz (4% of center frequency) shift in a SSTML loop antenna using optical tuning via a 4H-SiC photosensitive capacitor (PSC). These PSC devices, when optimized and combined with other monolithic circuitry, will be extremely useful for lower frequency phase shifters and passive sensing applications particularly when extremely rugged or high temperature solutions are required. Even with relatively low illumination intensity (< 1 W), RF resonance shifts were detectable from a loop antenna coupled only by mutual inductance. In every case, the observed frequency shift was marked by a significant loss in coupling efficiency that may hinder high powered RF applications but future work on improving the RF circuit should improve this situation. These initial investigations warrant more work to be done with the devices to push the boundaries of ruggedized electronics for both RF and UV sensing applications.

CHAPTER 6: CONCLUSION AND FUTURE WORK

6.1 Conclusion

There are many ways that SiC can be used as a biomaterial for both passive encapsulation and sensing applications. We have shown that the material's mechanical resilience, chemical resistance, and semiconductor properties make it suitable for the next generation of active implants and biodevices. Although SiC materials are costly and the use of the materials is process intensive, we believe the benefit they provide may far outweigh any potential cost. Currently, no other biomaterial provides suitable solutions for chronic implantation.

Processing highly stressed wafers of 3C-SiC on Si was a very challenging part of the work. If the stress in the material could be kept to near nominal levels, alignment error due to wafer bow and fractured substrates would vastly improve yield and processing speed. Efforts to nominalize the resulting stress in the CVD SiC wafers produced by our team are currently ongoing.

Despite these setbacks the original goal of this research, the demonstration of an advance SiC-based Optrode, was achieved, albeit in the absence of biological testing due to final device fabrication failure caused by the aforementioned stress issue. Nonetheless, a novel, all-biocompatible neural interface consisting of 4 electrical recording traces and an integrated optical waveguide has been simulated designed and fabricated. This device is capable of delivering both blue and yellow light, which is needed in optogenetics research, and has been characterized on the laboratory bench and shown optical performance similar to what is reported in the literature. What is novel here is the *a*-SiC coating, which has not been reported, and the integration of this waveguide on biocompatible 3C-SiC supports. With lower-stress 3C-SiC films we will be able to harvest these novel probes and use them for optogenetics experiments in the near future (see the next section, Future Work, for more details).

The amorphous SiC (*a*-SiC) process developed herein is useful for insulators and encapsulation of other active components and shows good biocompatabiliy based on ISO10993 stesting in our group . The process presented has tunable Si/C stoichiometric ratios allowing for control of optical index, inherent stress (compressive or tensile), and can be applied across a wide temperature range. Due to the temperature agility the process can be used for deposition over polymer biomaterials improving encapsulation and thereby acting as a barrier to prevent dissolution of the base material [80].

The photocapacitance work presented for HPSI 4H-SiC is the first documented case of the photocapacitance effect in 4H-SiC used in a device role. Although preliminary, the data shows promise for UV sensing and RF tuning applications. RF tuning of resonant structures was achieved with over a 4% shift in resonance indicative of an observable capacitance change. In the future this would be coupled to monolithic inductors to form wireless sensor elements.

Overall, we have established SiC as a rugged, implantable, biomaterial that can be used for a wide variety of biological applications. We have explored several uses for the material by modeling physically relevant effects and collecting relevant data. In addition, by developing new processes to deposit and fabricate wSiC biomaterials we have pushed closer towards our goal of long-term functional implants.

6.2 Future Work

The SiC based optrode device presented in Chapter 4 is the first step in integrating onboard power and electronics that will make an implantable BMI interface designed for chronic implantation. By adding single crystal SiC based electrodes in 3C-SiC and waveguides to the optrode system presented, an entirely ‘all-SiC’ metal-free implant can be realized. This would be a large step forward for the technology and would prevent many of the complications caused by long-term failure of current biomaterials. Improvements in the heteroepitaxial growth of 3C-SiC on Si by are group are the key to this dream, and recent progress indicates that very low wafer

bow is possible once the correct growth process is used. The first task to complete, based on this work, is the realization of free-standing SiC optrodes based on the work presented in Chapter 4.

The same holds true for the microelectrode array (MEA) systems presented in Chapter 3. These devices would also greatly benefit from the removal of metal in long-term cell culture. Again, in conjunction with single-crystal SiC waveguides, these devices would improve current *in vitro* testing. One important materials processing point requires further elaboration at this point to show how the 'all-SiC' device would be realized.

Using a highly conductive trace of 3C-SiC, say p^{++} doped via either ion implantation, laser-based implantation, or epi growth followed by etch-back, a pn-junction isolated electrode can be realized as shown in Figure 72.

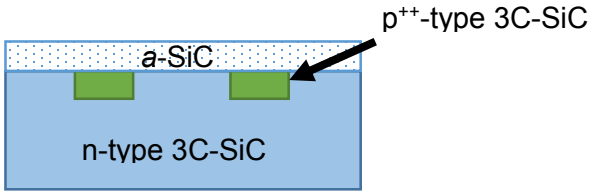

Figure 69: Cross-section schematic of pn junction isolation. Diagram depicts adjacent highly conductive traces of 3C-SiC. The process consists starts with lightly doped (either n or p type) 3C-SiC film epitaxially grown. Next, A highly doped (either p^{++} or n^{++}) film is then formed to realize the conductive trace. Due to the pn junction blocking adjacent traces would be electrically isolated to reduce cross-talk. Coating of the entire device with *a*-SiC would finish the 'all-SiC' device structure thus allowing for *in vitro* and *in vivo* use.

Working with Applicote LLC, Orlando, FL, we have been developing a direct-write laser doping process that would allow for a much more cost effective means to realize the conductive traces of Fig. 72. Figure 73 shows some examples of preliminary data from Applicote on USF provided SiC substrates. Both n+ and p+ traces have been realized to date. However process optimization is on-going and the most important characterization, the proof that a suitable pn junction can be realized, is one of the first orders of business here.

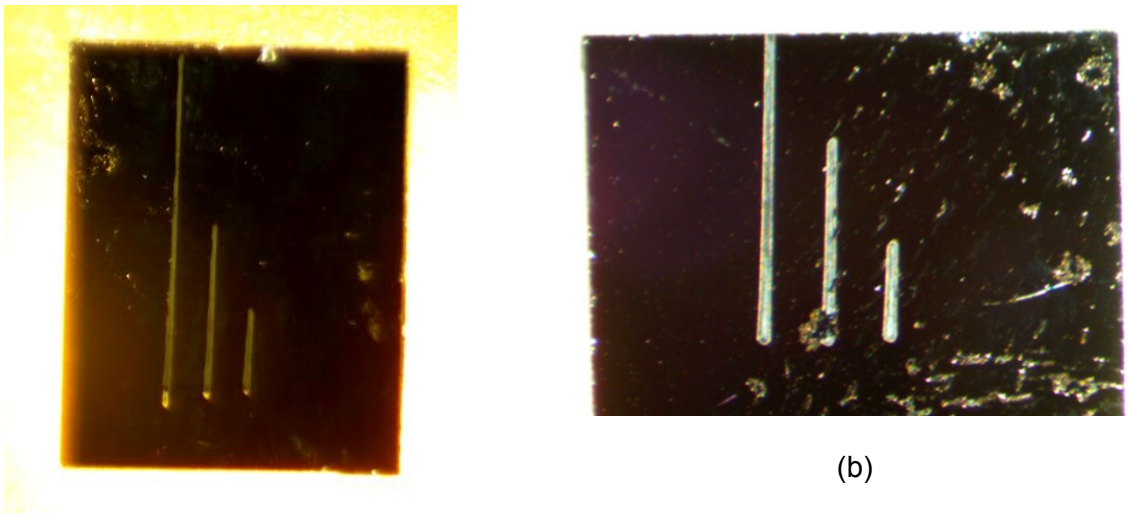

(a) (b)

Figure 70: Optical micrographs of laser doped traces in 3C-SiC. (a) n+ doped 3C-SiC on n- 3C-SiC and (b) p+ doped 3C-SiC on n- 3C-SiC. Data courtesy of Applicote LLC, Orlando, FL. This process would allow for the realization of an 'all-SiC' device that would be lower cost and fabrication time than traditional ion implantation and annealing.

The amorphous SiC (*a*-SiC) coatings developed in Chapter 2 hold promise for long-term use. The process to deposit these coatings can still be optimized through the removal of oxygen contamination and better stress measurement techniques. By improving this process it may be possible to further reduce the deposition temperature and incorporate low temperature polymer substrates such as Polyethylene.

All of the optical stimulation in the presented work was done using the single photon stimulation. By using two-photon stimulation, it has been shown that stimulation events can take place deep within the tissue without optically stimulating the tissue up until the focus point. As an example, by focusing a 946 nm light source to a point deep within the tissue a two-photon event will occur at the focus depth having the energy of two 946 nm photons or the characteristic 473 nm stimulation required for Chr2 opsins. In this way, more precision could be added to the optrode system presented in Chapter 5. Through using two-photon stimulation the stimulation point could be located some distance from the implant providing better targeting.

REFERENCES

[1] B. P. Bean, “The action potential in mammalian central neurons.,” *Nat. Rev. Neurosci.*, vol. 8, no. 6, pp. 451–65, Jun. 2007.

[2] N. Joye, A. Schmid, and Y. Leblebici, “Electrical modeling of the cell–electrode interface for recording neural activity from high-density microelectrode arrays,” *Neurocomputing*, vol. 73, no. 1–3, pp. 250–259, Dec. 2009.

[3] R. M. Rothschild, “Neuroengineering tools/applications for bidirectional interfaces, brain-computer interfaces, and neuroprosthetic implants - a review of recent progress.,” *Front. Neuroeng.*, vol. 3, p. 112, Jan. 2010.

[4] M. van Gerven, J. Farquhar, R. Schaefer, R. Vlek, J. Geuze, A. Nijholt, N. Ramsey, P. Haselager, L. Vuurpijl, S. Gielen, and P. Desain, “The brain-computer interface cycle.,” *J. Neural Eng.*, vol. 6, no. 4, p. 041001, Aug. 2009.

[5] J. M. Carmena, M. A. Lebedev, R. E. Crist, J. E. O’Doherty, D. M. Santucci, D. F. Dimitrov, P. G. Patil, C. S. Henriquez, and M. A. L. Nicolelis, “Learning to control a brain-machine interface for reaching and grasping by primates.,” *PLoS Biol.*, vol. 1, no. 2, p. E42, Nov. 2003.

[6] K. C. Cheung, “Implantable microscale neural interfaces.,” *Biomed. Microdevices*, vol. 9, no. 6, pp. 923–38, Dec. 2007.

[7] S. F. Cogan, D. J. Edell, A. A. Guzelian, Y. Ping Liu, and R. Edell, “Plasma-enhanced chemical vapor deposited silicon carbide as an implantable dielectric coating,” *J. Biomed. Mater. Res. Part A*, vol. 67A, no. 3, pp. 856–867, 2003.

[8] S. F. Cogan, “Neural stimulation and recording electrodes.,” *Annu. Rev. Biomed. Eng.*, vol. 10, pp. 275–309, Jan. 2008.

[9] K. D. Wise, J. B. Angell, and A. Starr, “An Integrated-Circuit Approach to Extracellular Microelectrodes,” *IEEE Trans. Biomed. Eng.*, vol. BME-17, no. 3, pp. 238–247, Jul. 1970.

[10] K. Wise and J. Angell, “A microprobe with integrated amplifiers for neurophysiology,” in *1971 IEEE International Solid-State Circuits Conference. Digest of Technical Papers*, 1971, vol. XIV, pp. 100–101.

[11] K. Takahashi and T. Matsuo, “Integration of multi-microelectrode and interface circuits by silicon planar and three-dimensional fabrication technology,” *Sensors and Actuators*, vol. 5, no. 1, pp. 89–99, 1984.

[12] U. of Michigan, “No Title,” 2014. .

[13] C. L. Frewin, “The neuron-silicon carbide interface: biocompatibility study and BMI device development,” University of South Florida, 2009.

[14] P. R. Albert, “Light up your life: Optogenetics for depression?,” *J. Psychiatry Neurosci.*, vol. 39, no. 1, pp. 3–5, Jan. 2014.

[15] M. M. Sidor and C. A. Mcclung, “Timing matters: Using optogenetics to chronically manipulate neural circuits and rhythms,” *Front. Behav. Neurosci.*, vol. 8, 2014.

[16] F. E. Jensen, “Epilepsy in 2013: Progress across the spectrum of epilepsy research.,” *Nat. Rev. Neurol.*, Jan. 2014.

[17] K. Deisseroth, “Optogenetics: Controlling the Brain with Light,” *Scientific American*, 2010.

[18] A. V Kravitz, B. S. Freeze, P. R. L. Parker, K. Kay, M. T. Thwin, K. Deisseroth, and A. C. Kreitzer, “Regulation of parkinsonian motor behaviours by optogenetic control of basal ganglia circuitry.,” *Nature*, vol. 466, no. 7306, pp. 622–626, 2010.

[19] M. Schermer, “Ethical issues in deep brain stimulation.,” *Front. Integr. Neurosci.*, vol. 5, p. 17, Jan. 2011.

[20] S. D. Davis, D. F. Gibbons, R. L. Martin, S. R. Levitt, J. Smith, and R. V Harrington, “Biocompatibility of ceramic implants in soft tissue.,” *J. Biomed. Mater. Res.*, vol. 6, no. 5, pp. 425–49, Sep. 1972.

[21] R. A. Normann, E. M. Maynard, P. J. Rousche, and D. J. Warren, “A neural interface for a cortical vision prosthesis,” *Vision Res.*, vol. 39, no. 15, pp. 2577–2587, 1999.

[22] M. A. Lebedev and M. A. L. Nicolelis, “Brain–machine interfaces: past, present and future,” *Trends Neurosci.*, vol. 29, no. 9, pp. 536–546, 2006.

[23] M. A. Liker, D. S. Won, V. Y. Rao, and S. E. Hua, *Deep Brain Stimulation: An Evolving Technology*, vol. 96, no. 7. IEEE-INST ELECTRICAL ELECTRONICS ENGINEERS INC, 2008, pp. 1129–1141.

[24] C. T. Nordhausen, P. J. Rousche, and R. a Normann, “Optimizing recording capabilities of the Utah Intracortical Electrode Array.,” *Brain Res.*, vol. 637, no. 1–2, pp. 27–36, Feb. 1994.

[25] W. Asaad and E. Eskandar, “The movers and shakers of deep brain stimulation.,” *Nat. Med.*, vol. 14, no. 1, pp. 17–9, Jan. 2008.

[26] M. Im, I.-J. Cho, F. Wu, K. D. Wise, and E. Yoon, “Neural probes integrated with optical mixer/splitter waveguides and multiple stimulation sites,” in *2011 IEEE 24th International Conference on Micro Electro Mechanical Systems*, 2011, pp. 1051–1054.

[27] A. Arbor, “A 16-SITE NEURAL PROBE INTEGRATED WITH A WAVEGUIDE FOR OPTICAL STIMULATION Il-Joo Cho , Hyoung Won Baac and Euisik Yoon Department of Electrical Engineering and Computer Science,” *Electr. Eng.*, pp. 995–998, 2010.

[28] A. V Kravitz and A. C. Kreitzer, “Optogenetic manipulation of neural circuitry in vivo,” *Curr. Opin. Neurobiol.*, vol. 21, no. 3, pp. 433–439, 2011.

[29] X. Han, X. Qian, J. Bernstein, H. Zhou, G. Franzesi, P. Stern, R. Bronson, A. Graybiel, R. Desimone, and E. Boyden, “Millisecond-timescale optical control of neural dynamics in the nonhuman primate brain,” *Neuron*, vol. 62, no. 2, pp. 191–198, 2009.

[30] A. N. ZORZOS, C. , A. DIETRICH, G. TALEI FRANZESI, B. CHOW, X. HAN, and E. S. B. G. FONSTAD, “Light-proof neural recording electrodes,” *Soc. Neurosci. Abstr.*, 2009.

[31] L. Sang, M. Liao, and M. Sumiya, “A comprehensive review of semiconductor ultraviolet photodetectors: from thin film to one-dimensional nanostructures.,” *Sensors (Basel).*, vol. 13, no. 8, pp. 10482–518, Jan. 2013.

[32] X. Tang, K. Wongchotigul, and M. G. Spencer, “Optical waveguide formed by cubic silicon carbide on sapphire substrates,” *Appl. Phys. Lett.*, vol. 58, no. 9, p. 917, Mar. 1991.

[33] C. A. Zorman, A. Eldridge, J. G. Du, M. Johnston, A. Dubnisheva, S. Manley, W. Fissell, A. Fleischman, and S. Roy, “Amorphous Silicon Carbide as a Non-Biofouling Structural Material for Biomedical Microdevices,” *Mater. Sci. Forum*, vol. 717–720, pp. 537–540, Jun. 2012.

[34] S. Saddow, *Silicon Carbide Biotechnology: A Biocompatible Semiconductor for Advanced Biomedical Devices and Applications (Google eBook)*. Elsevier, 2011, p. 495.

[35] S. S. Stensaas and L. J. Stensaas, “Histopathological evaluation of materials implanted in the cerebral cortex,” *Acta Neuropathol.*, vol. 41, no. 2, pp. 145–155, 1978.

[36] V. S. Polikov, P. A. Tresco, and W. M. Reichert, “Response of brain tissue to chronically implanted neural electrodes,” *J. Neurosci. Methods*, vol. 148, no. 1, pp. 1–18, 2005.

[37] C. J. Wilson, R. E. Clegg, D. I. Leavesley, and M. J. Pearcy, “Mediation of biomaterial-cell interactions by adsorbed proteins: a review.,” *Tissue Eng.*, vol. 11, no. 1–2, pp. 1–18.

[38] L. Ponsonnet, K. Reybier, N. Jaffrezic, V. Comte, C. Lagneau, M. Lissac, and C. Martelet, “Relationship between surface properties (roughness, wettability) of titanium and titanium alloys and cell behaviour,” *Mater. Sci. Eng. C*, vol. 23, no. 4, pp. 551–560, 2003.

[39] K. A. Ludwig, J. D. Uram, J. Yang, D. C. Martin, and D. R. Kipke, “Chronic neural recordings using silicon microelectrode arrays electrochemically deposited with a poly(3,4-ethylenedioxythiophene) (PEDOT) film.,” *J. Neural Eng.*, vol. 3, no. 1, pp. 59–70, Mar. 2006.

[40] and S. P. B. John M. Maloney, Sara A. Lipka, “In Vivo Biostability of CVD Silicon Oxide and Silicon Nitride Films,” *Mater. Res. Soc.*, vol. Mater. Res, no. 872, 2005.

[41] Y.-S. Chou and D. J. Green, “Silicon Carbide Platelet/Alumina Composites: II, Mechanical Properties,” *J. Am. Ceram. Soc.*, vol. 76, no. 6, pp. 1452–1458, Jun. 1993.

[42] C. I. and D. P. Poenar, *Physics and Technology of Silicon Carbide Devices*. InTech, 2012.

[43] P. Temple-Boyer, “Residual stress in low pressure chemical vapor deposition SiN[sub x] films deposited from silane and ammonia,” *J. Vac. Sci. Technol. A Vacuum, Surfaces, Film.*, vol. 16, no. 4, p. 2003, Jul. 1998.

[44] H. Zhang, H. Guo, Z. Chen, G. Zhang, and Z. Li, “Application of PECVD SiC in glass micromachining,” *J. Micromechanics Microengineering*, vol. 17, no. 4, pp. 775–780, Apr. 2007.

[45] H. Guo, Y. Wang, S. Chen, G. Zhang, H. Zhang, and Z. Li, “PECVD SiC as a Chemical Resistant Material in MEMS,” in *2006 1st IEEE International Conference on Nano/Micro Engineered and Molecular Systems*, 2006, pp. 805–808.

[46] Stephen Saddow, *Silicon Carbide Biotechnology*. Elsevier Science, 2011, p. 495.

[47] M. Reyes, Y. Shishkin, S. Harvey, and S. E. Saddow, “Development of a high-growth rate 3C-SiC on Si CVD process,” *MRS Proc.*, vol. 911, pp. 0911–B08–01, Feb. 2011.

[48] J. R. Buitenweg, W. L. C. Rutten, and E. Marani, “Geometry-based finite-element modeling of the electrical contact between a cultured neuron and a microelectrode.,” *IEEE Trans. Biomed. Eng.*, vol. 50, no. 4, pp. 501–9, Apr. 2003.

[49] K. B. Oldham, “A Gouy–Chapman–Stern model of the double layer at a (metal)/(ionic liquid) interface,” *J. Electroanal. Chem.*, vol. 613, no. 2, pp. 131–138, 2008.

[50] D. A. Sverjensky, “Interpretation and prediction of triple-layer model capacitances and the structure of the oxide-electrolyte-water interface,” *Geochim. Cosmochim. Acta*, vol. 65, no. 21, pp. 3643–3655, 2001.

[51] I. Schoen and P. Fromherz, “The mechanism of extracellular stimulation of nerve cells on an electrolyte-oxide-semiconductor capacitor.,” *Biophys. J.*, vol. 92, no. 3, pp. 1096–111, Feb. 2007.

[52] M. Grattarola and S. Martinoia, “Modeling the neuron-microtransducer junction: from extracellular to patch recording.,” *IEEE Trans. Biomed. Eng.*, vol. 40, no. 1, pp. 35–41, Jan. 1993.

[53] S. Eick, J. Wallys, B. Hofmann, A. van Ooyen, U. Schnakenberg, S. Ingebrandt, and A. Offenhäusser, “Iridium oxide microelectrode arrays for in vitro stimulation of individual rat neurons from dissociated cultures.,” *Front. Neuroeng.*, vol. 2, p. 16, Jan. 2009.

[54] M. Bariatto and A. Fontes, “IMPEDANCE CHARACTERIZATION AND MODELING OF MICROELECTRODES FOR NEURAL RECORDING,” *Natl. Inst. Astrophys. Opt. Electron.*, pp. 108–113.

[55] *The biomedical engineering handbook. 2*. Springer, 2000, p. 1408.

[56] C. Coletti, M. J. Jaroszeski, A. Pallaoro, A. M. Hoff, S. Iannotta, and S. E. Saddow, “Biocompatibility and wettability of crystalline SiC and Si surfaces.,” *Conf. Proc. Int. Conf. IEEE Eng. Med. Biol. Soc.*, vol. 2007, no. Di, pp. 5850–5853, 2007.

[57] S. A. P. WAI-FUNG CHEONG, “A Review of the Optical Properties of Biological Tissues,” *IEEE J. Quantum Electron.*, vol. 26, no. 12, 1990.

[58] A. M. Aravanis, L.-P. Wang, F. Zhang, L. a Meltzer, M. Z. Mogri, M. B. Schneider, and K. Deisseroth, “An optical neural interface: in vivo control of rodent motor cortex with integrated fiberoptic and optogenetic technology.,” *J. Neural Eng.*, vol. 4, no. 3, pp. S143–56, Sep. 2007.

[59] S. Guo, H. Zhou, J. Zhang, K. Xu, and X. Zheng, “A multi-electrode array coupled with fiberoptic for deep-brain optical neuromodulation and electrical recording.,” *Conf. Proc. IEEE Eng. Med. Biol. Soc.*, vol. 2013, pp. 2752–5, Jan. 2013.

[60] A. N. Yaroslavsky, P. C. Schulze, I. V Yaroslavsky, R. Schober, F. Ulrich, and H. J. Schwarzmaier, “Optical properties of selected native and coagulated human brain tissues in vitro in the visible and near infrared spectral range.,” *Phys. Med. Biol.*, vol. 47, no. 12, pp. 2059–2073, 2002.

[61] O. Yizhar, L. E. Fenno, T. J. Davidson, M. Mogri, and K. Deisseroth, “Optogenetics in neural systems.,” *Neuron*, vol. 71, no. 1, pp. 9–34, 2011.

[62] M. Inc, “No Title.” pp. 3–4, 2012.

[63] G. Ghosh, “Dispersion-equation coefficients for the refractive index and birefringence of calcite and quartz crystals,” *Opt. Commun.*, vol. 163, no. 1, pp. 95–102, 1999.

[64] A. A. Volinsky, G. Kravchenko, P. Waters, J. D. Reddy, C. Locke, C. Frewin, and S. E. Saddow, “Residual Stress in CVD-grown 3C-SiC Films on Si Substrates,” *MRS Proc.*, vol. 1069, pp. 1069–D03–05, Feb. 2011.

[65] K. V Nemani, K. L. Moodie, J. B. Brennick, A. Su, and B. Gimi, “In vitro and in vivo evaluation of SU-8 biocompatibility.,” *Mater. Sci. Eng. C. Mater. Biol. Appl.*, vol. 33, no. 7, pp. 4453–9, Oct. 2013.

[66] K. A. Boulais, F. Santiago, P. L. Wick, J. M. Mejeur, A. Rayms-Keller, M. S. Lowry, K. J. Long, and W. D. Sessions, “Circuit Analysis of Photosensitive Capacitance in Semi-Insulating GaAs,” *IEEE Trans. Electron Devices*, vol. 60, no. 2, pp. 793–798, Feb. 2013.

[67] K. A. Boulais, D. W. Rule, S. Simmons, F. Santiago, V. Gehman, K. Long, and A. Rayms-Keller, “Tunable split-ring resonator for metamaterials using photocapacitance of semi-insulating GaAs,” *Appl. Phys. Lett.*, vol. 93, no. 4, p. 043518, 2008.

[68] A. Goswami and A. P. Goswami, “Dielectric and optical properties of ZnS films,” *Thin Solid Films*, vol. 16, no. 2, pp. 175–185, May 1973.

[69] R. J. Kumar, J. M. Borrego, R. J. Gutmann, J. R. Jenny, D. P. Malta, H. M. Hobgood, and C. H. Carter, “Microwave photoconductivity decay characterization of high-purity 4H-SiC substrates,” *J. Appl. Phys.*, vol. 102, no. 1, p. 013704, Jul. 2007.

[70] A. Horsfall, “Review of ‘Advances in Silicon Carbide Processing and Applications’ 1st Edition by Steven E. Saddow and Anant Agarwal,” *BioMedical Engineering OnLine*, vol. 4. BioMed Central, p. 33, 2005.

[71] P. B. Klein, B. V. Shanabrook, S. W. Huh, A. Y. Polyakov, M. Skowronski, J. J. Sumakeris, and M. J. O'Loughlin, "Lifetime-limiting defects in n[sup −] 4H-SiC epilayers," *Appl. Phys. Lett.*, vol. 88, no. 5, p. 052110, Feb. 2006.

[72] N. Son, P. Carlsson, J. Ul Hassan, B. Magnusson, and E. Janzén, "Defects and carrier compensation in semi-insulating 4H-SiC substrates," *Phys. Rev. B*, vol. 75, no. 15, pp. 1–8, 2007.

[73] L. S. Løvlie, "Intrinsic bulk and interface defects in 4H silicon carbide." 29-Jan-2013.

[74] S. Dueñas, E. Castán, A. de Dios, L. Bailón, J. Barbolla, and A. Pérez, "Characterization of the EL2 center in GaAs by optical admittance spectroscopy," *J. Appl. Phys.*, vol. 67, no. 10, p. 6309, May 1990.

[75] S. Singh and J. A. Cooper, "Bipolar Integrated Circuits in 4H-SiC," *IEEE Trans. Electron Devices*, vol. 58, no. 4, pp. 1084–1090, Apr. 2011.

[76] G. B. Sakr and I. S. Yahia, "Effect of illumination and frequency on the capacitance spectroscopy and the relaxation process of p-ZnTe/n-CdMnTe/GaAs magnetic diode for photocapacitance applications," *J. Alloys Compd.*, vol. 503, no. 1, pp. 213–219, Jul. 2010.

[77] The American Radio Relay League (1988), "Small High Efficiency Loop Antennas for Transmitting," in *The ARRL Antenna Handbook. In (15th ed.).*, 1988, pp. 5–14.

[78] S. E. Saddow, C. L. Frewin, C. Coletti, N. Schettini, E. Weeber, A. Oliveros, and M. Jarosezski, "Single-Crystal Silicon Carbide: A Biocompatible and Hemocompatible Semiconductor for Advanced Biomedical Applications," *Mater. Sci. Forum*, vol. 679–680, pp. 824–830, Apr. 2011.

[79] M. Ahmadian, B. W. Flynn, A. F. Murray, and D. R. S. Cumming, "Miniature transmitter for implantable micro systems," in *Proceedings of the 25th Annual International Conference of the IEEE Engineering in Medicine and Biology Society (IEEE Cat. No.03CH37439)*, 2003, vol. 4, pp. 3028–3031.

[80] S. F. Cogan, D. J. Edell, A. A. Guzelian, Y. Ping Liu, and R. Edell, “Plasma-enhanced chemical vapor deposited silicon carbide as an implantable dielectric coating.,” *J. Biomed. Mater. Res. A*, vol. 67, no. 3, pp. 856–67, Dec. 2003.

[81] M. Levinshtein, S. Rumyantsev, and M. Shur, *Properties of advanced semiconductor materials : GaN, AlN, InN, BN, SiC, SiGe*. Wiley, 2001.

[82] M. B. J. Wijesundara and R. Azevedo, *Silicon Carbide Microsystems for Harsh Environments*, vol. 22. New York, NY: Springer New York, 2011.

[83] L. S. Lovlie and B. G. Svensson, “Enhanced annealing of implantation-induced defects in 4H-SiC by thermal oxidation,” *Appl. Phys. Lett.*, vol. 98, no. 5, p. 052108, Feb. 2011.

[84] M. Kato, S. Tanaka, M. Ichimura, E. Arai, S. Nakamura, T. Kimoto, and R. Pässler, “Optical cross sections of deep levels in 4H-SiC,” *J. Appl. Phys.*, vol. 100, no. 5, p. 053708, Sep. 2006.

[85] G. Liou, P. Lin, H. Yen, Y. Yu, and W. Chen, “Flexible Nanocrystalline-Titania / Polyimide Hybrids with High Refractive Index and Excellent Thermal Dimensional Stability,” *Polymer (Guildf).*, vol. 48, pp. 1433–1440, 2010.

[86] M. E. Levinshtein, S. L. Rumyantsev, and M. Shur, *Properties of advanced semiconductor materials : GaN, AlN, InN, BN, SiC, SiGe*. Wiley, 2001, pp. 93–148.

[87] W. C. Mitchel, R. Perrin, J. Goldstein, A. Saxler, M. Roth, S. R. Smith, J. S. Solomon, and A. O. Evwaraye, “Fermi level control and deep levels in semi-insulating 4H–SiC,” *J. Appl. Phys.*, vol. 86, no. 9, p. 5040, Nov. 1999.

[88] M. V. S. Chandrashekhar, I. Chowdhury, P. Kaminski, R. Kozlowski, P. B. Klein, and T. Sudarshan, “High Purity Semi-Insulating 4H-SiC Epitaxial Layers by Defect-Competition Epitaxy: Controlling Si Vacancies,” *Appl. Phys. Express*, vol. 5, no. 2, p. 025502, Feb. 2012.

[89] S. Kumar, “Simulation of Trapping Effects in 4H-Silicon Carbide Metal Semiconductor Field Effect Transistor (4H-SiC MESFET).” 06-Jun-2011.

APPENDICES

Appendix A 4H-SiC Simulation Parameter Table for Photocapacitance

Table A.1: 4H-SiC simulation parameter table for photocapacitance

Variable	Explanation	Reported Value	MKS units	Reference
$V_{ntherm al}$	Thermal Velocity of electrons	1.9E7 cm/s	1.9E5m/s	[81]
$V_{ptherm al}$	Thermal Velocity of Holes	1.2E7 cm/s	1.2E5m/s	[81]
σ_n	Electron Capture Cross Section of Z1/Z2 Defect	(2-4)E-15cm^2	(2-4)E-19m^2	[82][71]
σ_p	Hole Capture Cross Section of Z1/Z2 Defect	(1-2)E-14cm^2	(1-2E-18m^2	[82][71]
N_t	Intrinsic Carrier Concentration	(2-3)E15cm^{-3}	2-3E21m^{-3}	[83]
σ_p^0	Optical Ionization Cross Section (holes) *This data is still lacking in the literature	*	*	**
σ_n^0	Optical Ionization Cross Section (electrons)	1.5E-15cm^2	1.5E-19m^2	[84]
$N_{Z1/Z2\ trap}$	Z_1/Z_2 Defect Density *varies greatly with sample	1E13-1E14cm^{-3}	1E19-1E20m^{-3}	[69][85]
μ_e	Electron Mobility	≤900 $cm^2\ V^{-1}\ s^{-1}$	.09$m^2\ V^{-1}\ s^{-1}$	[81]
μ_n	Hole Mobility	≤120 $cm^2\ V^{-1}\ s^{-1}$	.012$m^2\ V^{-1}\ s^{-1}$	[86]
E_{gap}	Bandgap 4H SiC	3.25eV		[75]
E_{Fermi}	Fermi Level in HPSI 4H	1.6 below E_c *Due to defect pinning		[87]
$E_{Z1/Z2}$	Location of the Z1/Z2 Defect	Ec-.65eV		[4][5]
N_{Bs}	Shallow Boron Concentration	=3.6E+14cm^{-3} *varies	3.6E20m^{-3}	[88]
N_{Ns}	Shallow Nitrogen Concentration	=1.8E+15cm^{-3} *varies	1.8E21m^{-3}	[88]
$g_{0(Z1/Z2)}$	Degeneracy Factor of the Z1/Z2 Trap Center *Data is lacking in the literature			
$e_{nthermal\ @293K}$	Thermionic emission rate of electrons in the Z1/Z2 defect	.2516 $cm^{-3}\ s^{-1}$	2.516E5 $m^{-3}\ s^{-1}$	[89]
$e_{pthermal\ @293K}$	Thermionic emission rate of holes in the Z1/Z2 defect	.08 $cm^{-3}\ s^{-1}$	8E4 $m^{-3}s^{-1}$	[89]

Appendix B Parameters Used for Electrode Simulation Data

Table B.1: Parameters used for electrode simulation data

Parameters Used for Simulation Data		
Parameter	Value	Description
ε_{lHP}	6	Permittivity of Inner Layer [2]
ε_{d}	50	Permittivity of Diffuse Layer [2]
ε_{OHP}	32	Permittivity of Outer Layer [2]
d_{lhp}	0.3nm	Inner Plane Distance [2]
d_{ohp}	.7nm	Outer Plane Distance [2]
z	4	Number of Valance Electrons [2]
n^{0}	154mM	Bulk Concentration of Ions in Solution [2]
n	0.9	Factor for surface irregularities. [2]

Appendix C Permission for Reproduction of Materials

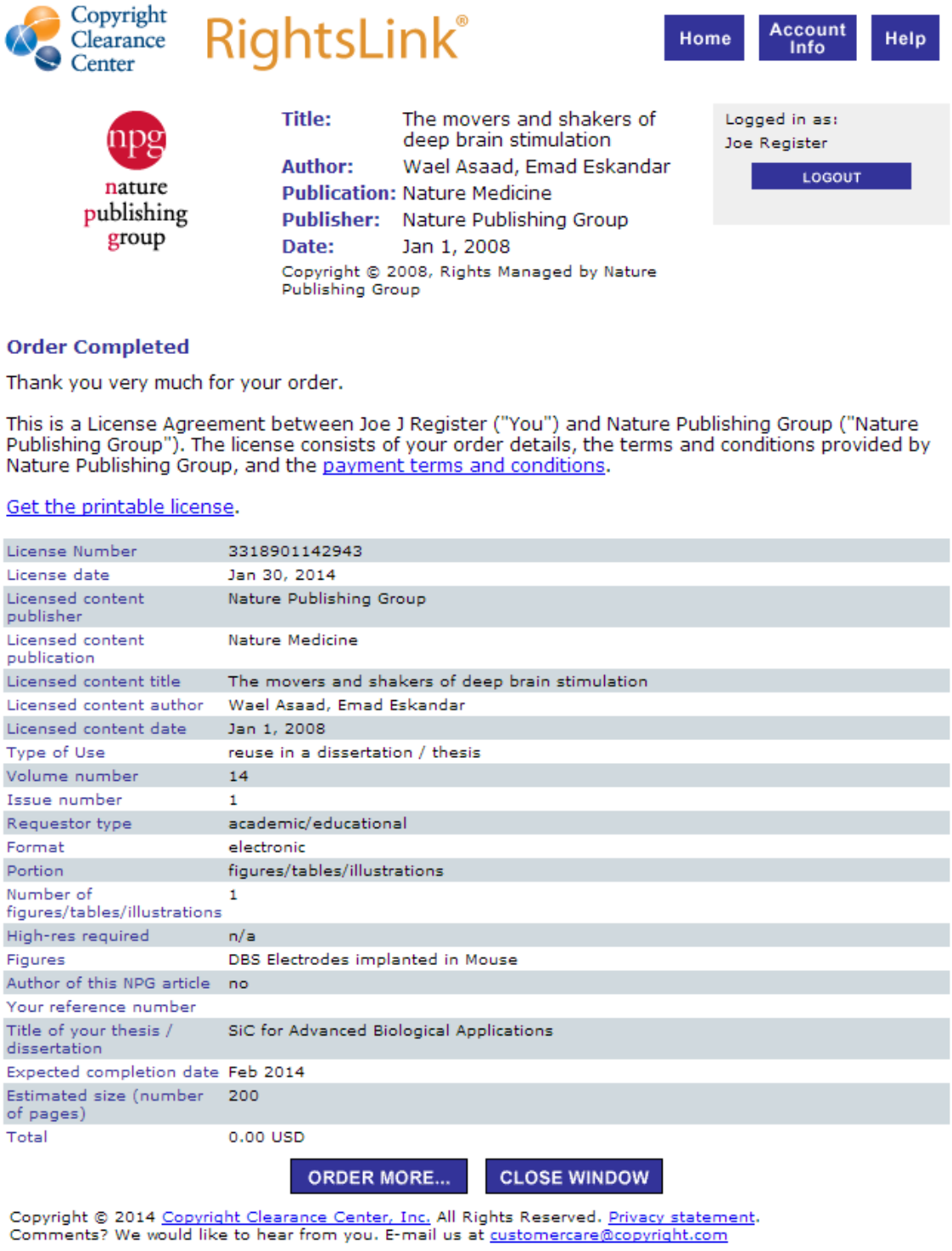

Copyright Clearance Center RightsLink®

Home | Account Info | Help

nature publishing group

Title: The movers and shakers of deep brain stimulation
Author: Wael Asaad, Emad Eskandar
Publication: Nature Medicine
Publisher: Nature Publishing Group
Date: Jan 1, 2008
Copyright © 2008, Rights Managed by Nature Publishing Group

Logged in as:
Joe Register
LOGOUT

Order Completed

Thank you very much for your order.

This is a License Agreement between Joe J Register ("You") and Nature Publishing Group ("Nature Publishing Group"). The license consists of your order details, the terms and conditions provided by Nature Publishing Group, and the payment terms and conditions.

Get the printable license.

License Number	3318901142943
License date	Jan 30, 2014
Licensed content publisher	Nature Publishing Group
Licensed content publication	Nature Medicine
Licensed content title	The movers and shakers of deep brain stimulation
Licensed content author	Wael Asaad, Emad Eskandar
Licensed content date	Jan 1, 2008
Type of Use	reuse in a dissertation / thesis
Volume number	14
Issue number	1
Requestor type	academic/educational
Format	electronic
Portion	figures/tables/illustrations
Number of figures/tables/illustrations	1
High-res required	n/a
Figures	DBS Electrodes implanted in Mouse
Author of this NPG article	no
Your reference number	
Title of your thesis / dissertation	SiC for Advanced Biological Applications
Expected completion date	Feb 2014
Estimated size (number of pages)	200
Total	0.00 USD

ORDER MORE... CLOSE WINDOW

Copyright © 2014 Copyright Clearance Center, Inc. All Rights Reserved. Privacy statement.
Comments? We would like to hear from you. E-mail us at customercare@copyright.com

Figure C.1: Reprint permission from Nature Publishing Group for Figure 5

Appendix C (Continued)

Copyright Clearance Center RightsLink®

Home | Account Info | Help

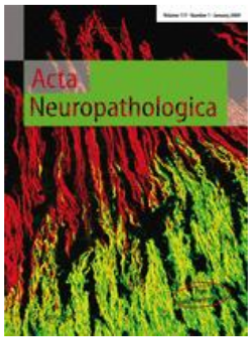

Title: Histopathological evaluation of materials implanted in the cerebral cortex
Author: Suzanne S. Stensaas
Publication: Acta Neuropathologica
Publisher: Springer
Date: Jan 1, 1978
Copyright © 1978, Springer-Verlag

Logged in as:
Joe Register
Account #:
3000745248
LOGOUT

Order Completed

Thank you very much for your order.

This is a License Agreement between Joe J Register ("You") and Springer ("Springer"). The license consists of your order details, the terms and conditions provided by Springer, and the payment terms and conditions.

Get the printable license.

License Number	3357091020906
License date	Mar 27, 2014
Licensed content publisher	Springer
Licensed content publication	Acta Neuropathologica
Licensed content title	Histopathological evaluation of materials implanted in the cerebral cortex
Licensed content author	Suzanne S. Stensaas
Licensed content date	Jan 1, 1978
Volume number	41
Issue number	2
Type of Use	Thesis/Dissertation
Portion	Figures
Author of this Springer article	No
Original figure numbers	1
Title of your thesis / dissertation	SiC for Advanced Biological Applications
Expected completion date	Mar 2014
Estimated size(pages)	150
Total	0.00 USD

CLOSE WINDOW

Figure C.2: Reprint permission from Springer Press for Figure 6